UNIVERSITY OF RIJEKA
FACULTY OF PHYSICS

Lovro Pavletić

INFLUENCE OF ATMOSPHERIC CONDITIONS ON OBSERVATIONS WITH IMAGING ATMOSPHERIC CHERENKOV TELESCOPES AND MULTI-WAVELENGTH ANALYSIS OF THE FLARING BLAZAR B2 1811+31

DOCTORAL DISSERTATION

Rijeka, 2026.

UNIVERSITY OF RIJEKA
FACULTY OF PHYSICS

Lovro Pavletić

INFLUENCE OF ATMOSPHERIC CONDITIONS ON OBSERVATIONS WITH IMAGING ATMOSPHERIC CHERENKOV TELESCOPES AND MULTI-WAVELENGTH ANALYSIS OF THE FLARING BLAZAR B2 1811+31

DOCTORAL DISSERTATION

Supervisor: prof. dr. sc. Dijana Dominis Prester

Rijeka, 2026.

SVEUČILIŠTE U RIJECI
FAKULTET ZA FIZIKU

Lovro Pavletić

UTJECAJ ATMOSFERSKIH UVJETA NA OPAŽANJA ČERENKOVLJEVIM TELESKOPIMA ZA SLIKOVNO BILJEŽENJE ATMOSFERE I ANALIZA BLJESKA BLAZARA B2 1811+31 U VIŠEVALNOM PODRUČJU

DOKTORSKI RAD

Mentor: prof. dr. sc. Dijana Dominis Prester

Rijeka, 2026.

Mentor rada: prof. dr. sc. Dijana Dominis Prester

Doktorski rad obranjen je dana ____________________ u/na __________

________________________________, pred povjerenstvom u sastavu:

1.________________________________

2.________________________________

3.________________________________

4.________________________________

5.________________________________

Ovaj je rad započet u Višnjanu, nastavljen u Vodnjanu, svoj oblik je poprimio u Mrkoplju, a završen je u Rijeci.

You pick the place and I'll choose the time
And I'll climb the hill in my own way
Just wait awhile for the right day
And as I rise above the tree line and the clouds
I look down, hear the sound of the things you said today
(Pink Floyd - Fearless, Meddle 1971)

There's no feeling more intense than starting over. If you've deleted your homework the day before it was due, as I have; or if you left your wallet at home and you have to go back after spending an hour in the commute; if you won some money at the casino and then put all your winnings on red, but it came up black; if you got your best shirt dry-cleaned before a wedding and then immediately dropped food on it; if you won an argument with a friend and then later discovered that they just returned to their original view... Starting over is harder than starting up. If you're not ready for that, like if you've already had a bad day, then what you're about to go through might be too much. Feel free to go away and come back. I'll be here.
(Getting over it with Bennet Foddy)

Acknowledgments: I would like to thank to all the people who have contributed in making of this thesis.

Influence of Atmospheric Conditions on Observations with Imaging Atmospheric Cherenkov Telescopes and Multi-Wavelength Analysis of the Flaring Blazar B2 1811+31

Abstract

Observations of Active Galactic Nuclei (AGNs) in the very-high-energy (VHE) gamma-ray domain are determined by both the intrinsic properties of their emission and the transparency of Earth's atmosphere. Since *Imaging Atmospheric Cherenkov Telescopes* (IACTs) like *Major Atmospheric Gamma Imaging Cherenkov Telescopes* (MAGIC) and *Cherenkov Telescope Array Observatory* (CTAO) rely on the detection of Cherenkov light produced in extensive air showers, changes in atmospheric transmission—due to clouds, aerosols, or artificial light pollution—can significantly affect detector sensitivity and energy reconstruction. This dissertation investigates the sensitivity of MAGIC LIDAR detectors to variations in the Night Sky Background (NSB), using data from the MAGIC Collaboration Database. The analysis focuses on the relationship between atmospheric transmission, measured by LIDAR, and its impact on observed background rates. Results highlight how artificial light pollution and cloud cover influence camera performance under different azimuthal angles and transmission levels. Additionally, using CORSIKA simulations, the study evaluates the impact of various cloud altitudes on CTAO-North sensitivity, showing that low clouds severely reduce performance, while high clouds have negligible effect. The principal component of this study presents a detailed study of the 2020 gamma-ray flare from B2 1811+31, which led to the first detection of VHE gamma rays from this source by MAGIC. Multi-wavelength data indicate a transition into a high-energy peaked blazar state, with modeling suggesting a two-zone synchrotron self-Compton scenario as the best explanation for the observed emission.

Keywords: gamma-rays: general, atmospheric effects, instrumentation: detectors, light pollution, methods: data analysis, site testing, active galactic nuclei.

Utjecaj atmosferskih uvjeta na opažanja Čerenkovljevim teleskopima za slikovno bilježenje atmosfere i analiza bljeska blazara B2 1811+31 u viševalnom području

Sažetak

Precizno opažanje aktivnih galaktičkih jezgri (AGN-ova) u vrlo visokom energetskom (VHE) gama-zračnom području ne ovisi samo o intrinzičnim emisijskim svojstvima tih izvora, već i o prozirnosti Zemljine atmosfere. Budući da teleskopi za promatranje Čerenkovljevog zračenja u atmosferi (IACT-ovi), poput MAGIC-a i CTAO-a, ovise o detekciji Čerenkovljevog svjetla koje nastaje u opsežnim zračnim pljuskovima, promjene u atmosferskoj transmisiji — uzrokovane oblacima, aerosolima ili umjetnim svjetlosnim zagađenjem — mogu značajno utjecati na osjetljivost detektora i rekonstrukciju energije. Ovaj doktorski rad istražuje osjetljivost MAGIC LIDAR sustava na varijacije u pozadinskom noćnom svjetlu (NSB), koristeći baze podataka kolaboracije MAGIC. Analiza se fokusira na odnos između atmosferske transmisije, mjerenje LIDAR-om, i njen utjecaj na opažene stope pozadinskog zračenja. Rezultati naglašavaju kako umjetno svjetlosno zagađenje i pokrivenost oblacima utječu na performanse kamera pri različitim azimutima i razinama transmisije. Dodatno, koristeći simulacije CORSIKA kodom, studija procjenjuje utjecaj oblaka različitih visina na osjetljivost CTAO-North-a, pokazujući da niski oblaci znatno smanjuju performanse, dok visoki oblaci imaju zanemariv utjecaj. Središnji dio ovog rada predstavlja detaljno proučavanje stanja pojačane aktivnosti iz 2020. godine s izvora B2 1811+31 koje je dovelo do prvog otkrića gama-zračenja vrlo visokih energija iz ovog izvora teleskopima MAGIC. Opažanja u viševalnom području ukazuju na prijelaz blazara u fazu pojačane visokoenergetske emisije, dok modeliranje pokazuje da dvozonski model sinkrotronskog vlastitog Comptona (SSC) najbolje opisuje promatranu emisiju.

Ključne riječi: gama-zrake: općenito, atmosferski učinci, instrumentacija: detektori, svjetlosno onečišćenje, metode: analiza podataka, ispitivanje lokacije, aktivne galaktičke jezgre.

Contents

Introduction

Gamma-ray astronomy explores the most energetic astrophysical phenomena in the universe, including pulsars and quasars powered by accreting black holes. Gamma rays observed in astrophysics are primarily produced by high-energy processes such as the decay of neutral pions created in cosmic-ray interactions, inverse Compton scattering of relativistic electrons on low-energy photons, synchrotron radiation in strong magnetic fields, and nuclear transitions in radioactive isotopes. Gamma-rays are photons with energies ranging from approximately 100 keV to several tens of TeV. High-energy (HE) and very-high-energy (VHE) gamma rays are commonly distinguished using an energy threshold of 100 GeV. This classification is also relevant with respect to the detection techniques employed.

To observe HE gamma rays, instruments are placed on satellites, as Earth's atmosphere absorbs the radiation. The first measurements were made by the *Orbiting Solar Observatory 3* (OSO-3) spacecraft in 1968 [1], and in 1972, the *Small Astronomy Satellite 2* (SAS-2) detected gamma radiation from two pulsars and the first quasar ever discovered [2]. An accidental discovery of strong cosmic radiation in the X-ray and gamma-ray regions, made during espionage efforts to detect nuclear activity on Earth, radically changed our understanding of the universe. Bursts of mysterious cosmic gamma radiation were detected in the late 1960s by the VELA satellite system, which had been launched by the U.S. Department of Defense to search for potential Soviet nuclear detonations, especially from the far side of the Moon [3]. The Soviets never conducted such tests, but instead, a new astronomical phenomenon was uncovered - actual bursts of radiation from distant regions of space.

Major Atmospheric Gamma Imaging Cherenkov Telescopes (MAGIC), later renamed to MAGIC *Florian Goebel Telescopes* is a collaboration that employs two telescopes located on the Canary Islands to detect VHE gamma radiation through imaging Cherenkov detection. MAGIC was established in 2004, with the first telescope installed in 2006. Its most significant achievements include the detection of gamma rays from astrophysical systems associated with supermassive black holes, as well as from pulsars and gamma-ray bursts (GRBs). [4].

The first GRB detected by the MAGIC telescopes, GRB 190114C, was a landmark observation, providing the highest-energy photons detected from a gamma-ray burst at the time. Detected on January 14th, 2019, the photons observed by MAGIC must originate from a previously unseen process in the afterglows of GRBs, distinct from the known mechanism responsible for their emission at lower energies [5].

MAGIC has also enabled the observation of astrophysical phenomena that were previously undetectable, greatly advancing our understanding of high-energy processes in space.

Cherenkov Telescope Array Observatory (CTAO), the world's largest system for detecting high-energy gamma radiation, is currently in its development phase, where the system is actively being tested and assembled. CTAO is an international project involving a network of telescopes positioned in both the Northern (La Palma, Spain) and Southern Hemispheres (Paranal, Chile). CTAO will cover a broad energy range from 20 GeV to 300 TeV by combining three types of telescopes (Large-Sized Telescope, Medium-Sized Telescope and Small-Sized Telescope), providing a sensitivity of $\approx 0.1\%$ of the Crab Nebula flux in 50 hours of observation [6, 7, 8].

In addition to MAGIC and CTAO, there are several other important collaborations and telescopes contributing to gamma astronomy. *The Fermi Gamma-ray Space Telescope* (FGST), previously known as *Gamma-ray Large Area Space Telescope* (GLAST), operates in orbit and investigates HE gamma radiation across a wide energy range [9]. The *High Energy Stereoscopic System* (H.E.S.S.), located in Namibia, uses Cherenkov detection to observe VHE gamma rays [10]. *Very Energetic Radiation Imaging Telescope Array System*

(VERITAS) in the United States and *Astrorivelatore Gamma a Immagini LEggero* (AGILE), which operated in Earth's orbit from 2007 to 2024, further enhanced global efforts in studying gamma radiation [11].

Imaging Atmospheric Cherenkov Telescopes (IACTs) rely fundamentally on the Earth's atmosphere as part of their detection mechanism, since Cherenkov light produced by extensive air showers must travel through atmospheric layers to reach the telescopes. Variability in atmospheric transmission—caused by the presence of aerosols, clouds, and other meteorological phenomena—directly affects the intensity and shape of the detected Cherenkov light signals. Such changes can alter the reconstructed energy and arrival direction of incoming gamma rays, and may introduce systematic errors in the interpretation of astrophysical sources, particularly at low energies. Therefore, detailed, real-time atmospheric monitoring and characterization have become indispensable for modern gamma-ray astronomy, especially for observatories like MAGIC and CTAO. Instruments like optical LIDARs and robotic photometric telescopes (such as FRAM) are used to derive atmospheric transmission profiles and aerosol optical depth (AOD), enabling both correction of observational data and the optimization of observing schedules. These systems ensure that valuable observing time is not lost due to unfavorable atmospheric conditions and that scientific results remain robust and reliable across a wide range of energies and source types [12].

Ground-based VHE gamma-ray observatories require clear nights with high atmospheric transparency. Therefore, such observatories are typically located in remote areas with dry air, minimal artificial light, and stable weather conditions, free from clouds and precipitation year-round. Although clouds can limit atmospheric transparency, experience with MAGIC telescopes shows that observations can still be conducted effectively under certain cloudy conditions. The study, analysis, and detailed monitoring of atmospheric conditions on both short-term and long-term scales above the Roque de los Muchachos Observatory on La Palma, where the MAGIC telescopes are located, form a significant part of this doctoral thesis. Atmospheric monitoring was conducted using the MAGIC micro-joule LIDAR system, which will be described in Chapter 4.

The second part of this doctoral thesis is dedicated to the analysis and evaluation of data, with a comprehensive study on the impact of reduced atmospheric transmission on the performance of CTAO-North and its subarrays. This investigation employs atmospheric modeling and Monte Carlo (MC) simulations to simulate air showers and telescope responses, as detailed in Chapter 5.

After *Fermi*-LAT detected a high state in the E $>$ 100 MeV range on October 1, 2020 (MJD 59123), a multi-wavelength (MWL) campaign on B2 1811+31 was launched. During this high state, MAGIC telescopes observed the first VHE γ-ray emission from the source. *The Neil Gehrels Swift Observatory*, along with other optical and radio telescopes, joined the follow-up, enabling a comprehensive study of the source across the electromagnetic spectrum.

The research conducted as the third part of this doctoral thesis underscores the critical importance of multiwavelength observations, as understanding active galactic nuclei requires more than just VHE observations from MAGIC. A detailed spectral energy distribution (SED) across the full electromagnetic spectrum is essential to fully characterize the complex phenomena occurring in these distant and energetically violent objects in the universe. Results discussed in Chapter 6 represent the principal contribution of this doctoral research to astrophysical studies.

Chapter 1

Active Galactic Nuclei

Active galactic nuclei (AGN) exhibit intense energetic emission from their central regions, which shows no clear correlation with the morphology of the host galaxy and cannot be explained by standard galactic emission mechanisms [13].

In the most widely accepted scenario, AGN emission arises from the presence of a supermassive black hole (SMBH) located at the galaxy's center. The SMBH converts gravitational energy into electromagnetic radiation, powered by the infall of nearby material such as gas, dust, and stars. The angular momentum of this material leads to the formation of an accretion disk, whose viscosity gradually removes angular momentum until the material is ultimately accreted by the black hole [14].

The observed luminosity variability in extremely compact AGN regions indicates the presence of highly energetic processes that are far more efficient than nuclear fusion, making AGNs the most powerful stable sources in the Universe. Their emission spans the entire electromagnetic spectrum, typically peaking in the ultraviolet (UV) range. Although the nuclear emission itself is not spatially resolved, radio interferometry can achieve angular resolutions of the order of milliarcseconds and, in the case of very-long-baseline interferometry such as the Event Horizon Telescope, down to tens of microarcseconds, revealing collimated outflows of material moving at relativistic velocities—known as jets [14].

The AGN spectra in the rest-frame optical range result from the superposition of multiple components: the active nucleus, stars, gas, and dust. Consequently, these spectra often include emission originating from the surrounding stellar population. The total AGN spectrum can be decomposed into several distinct, and often temporally variable, components:

- Emission from the accretion disk.
- Emission from relativistic jets.
- A system of relatively narrow emission lines originating in the narrow-line region (NLR). These lines are broader than those observed in normal galaxies, reflecting the kinematics of the emitting gas. Many of them are so-called forbidden lines (e.g., [N II], [O III], [O II]), arising from metastable excited states. Such transitions can occur only in regions of very low atomic density, as collisions at typical terrestrial densities would efficiently suppress them.
- A set of broad permitted lines (arising from the broad-line region, BLR), including the H-Balmer series as well as He I and He II transitions.
- Spectral lines characteristic of star formation processes. Since AGN activity and star formation commonly coexist within galaxies, disentangling their respective contributions remains a significant observational challenge.

1.1 Classification of AGNs

The main characteristics of different AGN types are summarized below, beginning with AGNs exhibiting low radio emission and proceeding to those with strong radio-loud activity.

Seyfert galaxies

- **Seyfert 1:** These galaxies are identified observationally by spectra that exhibit both narrow and broad emission lines, indicating the presence of narrow- and broad-line regions (NLRs and BLRs). Their observed continuum spectra show few absorption features and are dominated by emission from the central engine. In addition, they display strong X-ray emission and variability on timescales ranging from hours to days.

- **Seyfert 2:** These galaxies show weak or absent broad emission lines, with spectra dominated by narrow lines, a fainter continuum, and a significant contribution from stellar light. Their X-ray emission is weaker than in Seyfert 1 galaxies, as spectral analyses reveal that part of the emission is absorbed along the line of sight.

LINERs

Low-Ionization Nuclear Emission-Line Regions (LINERs) display strong low-ionization lines, such as [O I], [O II], and [N II], associated with gas that is excited or collisionally ionized. LINERs appear to be related to both AGN activity and star formation processes. Nearly all spiral galaxies exhibit nuclear LINER-type spectra, which are also observed in some H II regions [15].

Quasars

Quasar spectra exhibit a power-law continuum and broad emission lines similar to those of Seyfert 1 galaxies, characterized by weak narrow components and strong lines from highly ionized species. Compared to normal galaxies, quasars emit strongly in the infrared and across other wavelengths. Approximately 10% of quasars are radio-loud, showing intense radio emission—particularly from jets, which are sometimes visible even in the optical range. Due to their extreme intrinsic luminosity, quasars are observable at very high redshifts.

Radio Galaxies

The radio emission of these galaxies originates primarily from the nucleus, the lobes, and extended jets emanating from the central region. In some cases, two jets are observed, while in others, only one is visible. Fanaroff–Riley (FR) galaxies are classified according to the morphology of their radio emission, as introduced by British astronomers B. L.

Fanaroff and J. M. Riley in 1974 [16].

- **FR I:** The radio brightness decreases with distance from the galaxy center, typically showing two curved jets.
- **FR II:** The radio emission peaks at the ends of the lobes. These galaxies usually display a single straight jet, although a second, weaker jet may sometimes be detected.

Blazars

Blazars are the most violently variable type of AGN, characterized by two powerful plasma jets in which matter flows at relativistic velocities. Their defining feature is that one of these jets is oriented close to our line of sight, leading to strong relativistic beaming that amplifies the observed emission and shortens the variability timescales.

The blazar emission spans the electromagnetic spectrum from radio to γ-ray frequencies and shows variability across all wavelengths. The observed radio, near-infrared, and optical emission can be polarized, with both the degree and angle of polarization varying over time [17, 18]. The low-frequency emission originates from synchrotron radiation, while the high-energy component is most likely produced through inverse Compton scattering (see Section 1.6).

Blazars comprise two main subclasses [19]:

- **BL Lac Objects (BL Lacs):** Originally defined as sources with very weak or absent emission lines, making redshift determination difficult or impossible for many of them.
- **Flat Spectrum Radio Quasars (FSRQs):** Similar to BL Lac objects but exhibiting stronger emission lines, allowing their redshifts to be measured even at greater distances.

Both BL Lacs and FSRQs display extreme variability across multiple frequency bands, with large flux variations over short timescales. In some cases, intraday variability or microvariability—brightness changes on timescales of tens of minutes to a few hours—has been observed, a phenomenon not typically seen in quasars.

Based on their optical emission-line properties, active galactic nuclei are classified as broad-line AGNs (Type 1), which exhibit at least one broad emission line (FWHM $>$ $2000\ \mathrm{km\,s^{-1}}$), or as narrow-line AGNs (Type 2), characterized solely by narrow emission lines [20].

1.2 A Unified Model of AGN

The study of AGNs remains one of the most intriguing areas in astrophysics, as it provides insight into the fundamental processes of supermassive black hole growth and galactic evolution.

It seems like observational differences appear only due to the different orientations of galaxies as viewed along the line of sight for the observer from Earth, and different rates of accretion and masses of the central black holes. The existence of radio lobes that are present around AGNs is something in addition to, and consistent with, the basic model.

These lobes can significantly influence the surrounding intergalactic medium and further shape the evolution of AGNs. The general agreement on some of the specific details of the unified model of AGNs is not yet achieved, but the conceptual idea helps to provide a framework for organizing the systematic observations of AGNs and their interpretations.

Figure 1.1 shows $L_{H\alpha}$, the luminosity in the H_α emission line, and L_{FC}, the luminosity of the featureless continuum near 480 nm, plotted for several AGNs (excluding blazars). If the hydrogen emission lines are produced by the photoionization of hydrogen atoms by continuous radiation and subsequent recombination of the atoms, then the two luminosities should be proportional and a straight line with slope 1 should be found on the logarithmic graph. The slope of the dashed line is 1.05, confirming that $L_{H\alpha}$ is proportional to L_{FC}. This result supports a common physical connection between the continuum source and the emission-line regions in Seyfert 1 and 2 galaxies, broad and narrow-line radio galaxies, and radio-loud and radio-quiet quasars [21].

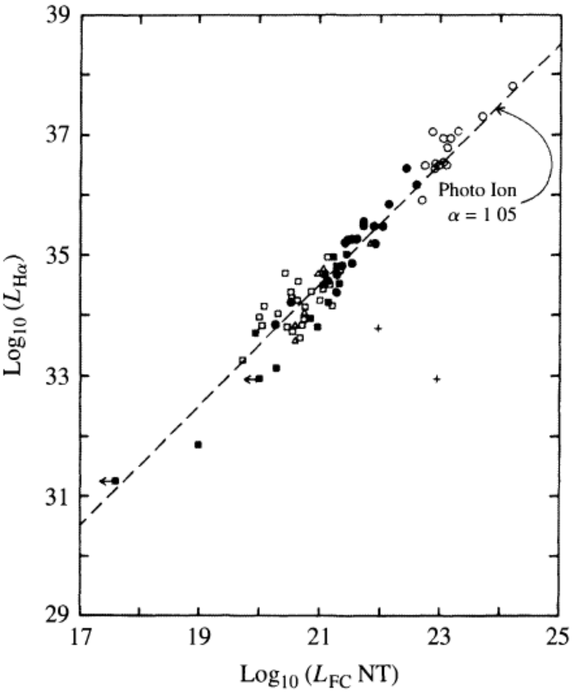

Figure 1.1: The luminosity in the H_α emission line versus the luminosity of the featureless continuum at a wavelength near 480 nm. Quasars are represented by open circles, Seyfert 1 galaxies by filled circles, Seyfert 2 galaxies by open squares, NLRGs by triangles, and more Seyfert 2 and NLRGs by filled squares. The "NT" stands for "non-thermal". Figure taken from [21].

Another piece of evidence for a unified model comes from an observation reported by Robert Antonucci and Joseph Miller in 1985 [22]. When they observed NGC 1068 (a Seyfert 2) in polarized light, they found a Seyfert 1 spectrum with a broad emission lines. This and similar cases discovered since then imply that within these Seyfert 2 galaxies there are Seyfert 1 nuclei that are hidden from from the direct view of Earth by some optically thick material [14]. The diminished Seyfert 1 spectrum (normally overwhelmed by the direct Seyfert 2 spectrum) comes from light that reaches us indirectly by reflection from the interstellar medium outside the nucleus. This reflection would also contribute to the observed linear polarization, when the electric field vector is perpendicular to the radio axis (the direction defined by the relativistic plasma jets emitted from the central region of the AGN, typically observed in radio wavelengths). The orientation of the AGN relative to the line of sight from Earth (example in Figure 1.2) will be an important factor in the unified model to be described [14].

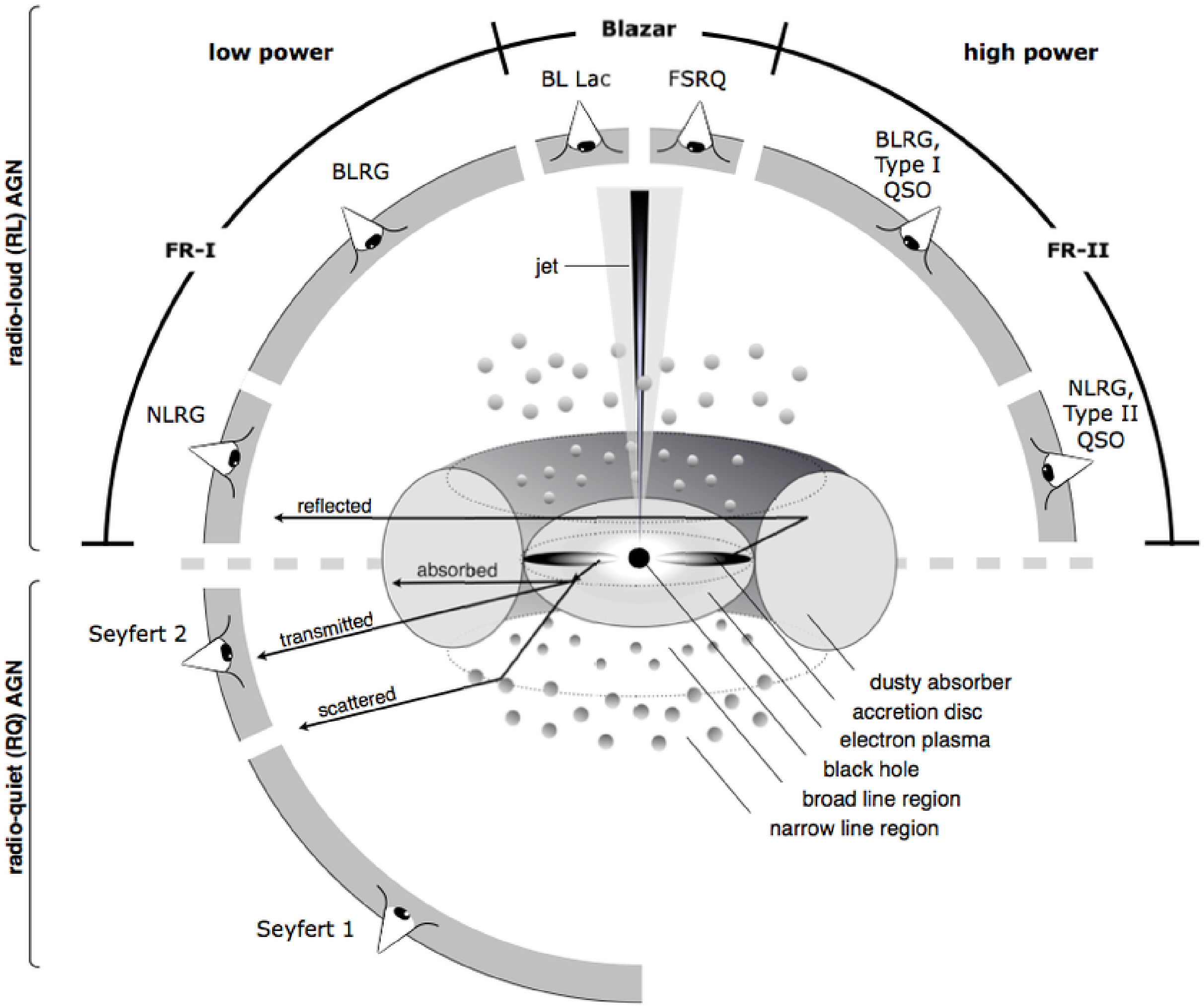

Figure 1.2: Conceptual illustration of the unified model of AGN. The observed AGN type depends primarily on the orientation of the system relative to the observer, the presence or absence of relativistic jets, and the intrinsic power of the central engine. Taken from [23].

1.3 Multi-wavelength Emission of AGN

AGNs are inherently multi-wavelength emitters, radiating throughout the entire electromagnetic spectrum from radio waves to γ-rays. Each portion of the spectrum probes a different physical component or process within the AGN, offering a complementary view of its structure and dynamics:

- **Radio**: Emission is typically non-thermal and originates from synchrotron processes in large-scale jets and radio lobes. High-resolution radio interferometry can reveal jet morphology, orientation, and dynamics.

- **Infrared (IR)**: Infrared emission may originate from both thermal emission of dust in the circumnuclear torus, heated by the accretion disk, and non-thermal synchrotron radiation from the jet, particularly in blazars. IR observations probe dust geometry and help disentangle thermal and non-thermal components.

- **Optical/Ultraviolet (UV)**: Primarily emitted by the accretion disk. Broad and narrow emission lines visible in this range help classify AGNs and provide insight into the dynamics of the broad line region (BLR) and narrow line region (NLR).

- **X-rays**: Arise from the hot corona above the accretion disk and potentially from relativistic jets. X-ray variability can reveal processes occurring very close to the SMBH, such as coronal heating or disk instabilities.

- **γ-rays**: Produced by inverse Compton scattering and hadronic interactions within relativistic jets. The detection of γ-ray emission is a signature of extreme conditions and highly accelerated particles.

1.4 Multi-wavelength Observations of Blazar Emissions

Blazars are classified into two main categories based on their optical spectral characteristics: flat spectrum radio quasars (FSRQs) and BL Lacertae (BL Lac) objects. FSRQs are distinguished by their higher luminosity and the presence of broad emission lines in their optical spectra, which serve as strong indicators of a broad line region (BLR). On the other hand, BL Lacs lack or show only weak emission lines and typically exhibit lower luminosities (see section 1.1).

One of the defining features of blazars is their high variability across a broad range of timescales, from short sub-hour variations to long-term changes. The emission from blazars is predominantly non-thermal radiation, spanning the entire electromagnetic spectrum, from radio to very high energy (VHE, $E \geq 100$ GeV) gamma rays.

The broad-band spectral energy distribution (SED) of a blazar is characterized by two prominent bumps [24]. The first bump peaks in the infrared to X-ray range and is typically attributed to synchrotron radiation, which is emitted by ultrarelativistic electrons accelerated within the blazar's jet. The second bump, which peaks at energies above MeV, is most likely due to inverse Compton (IC) scattering, possibly involving synchrotron photons from the same electron population, a process known as synchrotron self-Compton (SSC) [25, 26]. Additionally, external Compton processes, where photons from outside the jet are scattered, may also contribute. A sub-dominant hadronic component is also a possibility [27] and supported by evidence for neutrino emissions from nearby active galaxies [28, 29, 30].

BL Lac objects can be further categorized into three sub-classes based on the peak frequency of their spectral energy distribution (SED): high-frequency-peaked BL Lacs (HBLs), intermediate-frequency-peaked BL Lacs (IBLs), and low-frequency-peaked BL Lacs (LBLs) [31]:

- **LBLs**: $\nu_{\mathrm{peak}}^{\mathrm{syn}} < 10^{14}$ Hz,
- **IBLs**: 10^{14} Hz $\leq \nu_{\mathrm{peak}}^{\mathrm{syn}} < 10^{15}$ Hz,
- **HBLs**: $\nu_{\mathrm{peak}}^{\mathrm{syn}} \geq 10^{15}$ Hz.

Most of the blazars detected in the VHE gamma-ray range are HBLs, with a few IBLs and LBLs also being detected, typically during flare events [32]. The absence of low-energy-peaked sources in the VHE range can be attributed to the IC bump of these sources being located at lower energies, resulting in a reduced flux at TeV energies. This makes IBLs and LBLs ideal targets for low-energy gamma-ray telescopes such as the *Fermi Large Area Telescope* (LAT).

An empirical sequence connecting the bolometric luminosity of blazars with their classification has been established, with LBLs exhibiting higher luminosities compared to HBLs [33].

To gain a comprehensive understanding of the emission mechanisms in blazars, it is essential to have complete energy coverage of their emissions. This requires multi-wavelength (MWL) observations ranging from radio to VHE gamma rays. Additionally, due to the highly variable nature of their spectra, these observations should ideally be conducted (quasi-)simultaneously to capture a snapshot of the blazar's emission state. However, for weaker blazars, obtaining full energy coverage during low emission states can be challenging.

1.5 AGN Activity States: Quiescent, High, and Flaring

The terms *quiescent*, *high*, and *flaring state* refer to distinct phases of AGN variability, commonly identified through changes in flux amplitude and spectral shape in various energy bands (e.g., radio, optical, X-ray, and gamma-ray). While no universal threshold exists, a flaring state typically involves rapid and significant flux increases, particularly in high-energy bands, whereas the quiescent state denotes a baseline level of emission with minimal variability.

- **Quiescent state**: This refers to the AGN's baseline or lowest observed flux level. During this state, emission is relatively stable over time, and no significant spectral hardening or multi-band correlation is present. In radio-quiet AGNs, this may correspond to a disk-dominated spectrum, while in blazars, it represents the low-activity phase of the jet.
- **High state**: An intermediate level of activity, typically defined by a sustained increase in flux compared to the quiescent baseline. This state may or may not include strong variability and often corresponds to moderate changes in spectral indices or multi-wavelength correlations (e.g., optical/X-ray).
- **Flaring state**: A rapid and pronounced increase in flux, often accompanied by strong spectral changes. Flares are typically short-lived (hours to days) and most readily identified in the X-ray and γ-ray bands, particularly in blazars. Flaring episodes may involve enhanced particle acceleration in jets, magnetic reconnection, or instabilities in the inner accretion disk.

The determination of AGN activity state in this work is primarily based on the observed variability in γ-ray fluxes from MAGIC observations, complemented by publicly available data in X-ray, UV, optical, and radio bands from external monitoring programs. Time-resolved light curves and spectral energy distributions (SEDs) are used to categorize specific epochs into quiescent, high, or flaring states, typically characterized by flux changes of at least one order of magnitude and correlated spectral variations.

The distinction between states is crucial for interpreting the physical processes governing AGN emission. For example, during flaring states, gamma-ray emission is often dominated by inverse Compton scattering, either via synchrotron self-Compton (SSC) or external Compton (EC) mechanisms. In quiescent states, the emission is typically weaker, but still primarily arises from the same high-energy processes, including steady jet emission through inverse Compton or photo-hadronic interactions.

Multi-wavelength campaigns, involving simultaneous observations across radio, optical, X-ray, and γ-ray bands, are essential for unambiguously identifying and understanding these activity states.

1.6 Synchrotron Radiation and Inverse Compton Scattering in AGN

1.6.1 Synchrotron Radiation

Synchrotron radiation is one of the fundamental emission mechanisms in high-energy astrophysics and plays a central role in our understanding of AGNs, especially in the context of relativistic jets. This process occurs when relativistic electrons spiral around magnetic field lines, emitting highly polarized and broadband radiation that can span from radio wavelengths up to X-rays, depending on the electron energy and magnetic field strength [34].

In AGNs, particularly blazars, synchrotron radiation dominates the low-energy hump of the SED, peaking anywhere from radio to optical or even X-ray bands (see Figure 1.3). The shape and variability of the synchrotron component provide direct insights into the physical conditions in the jet, including the magnetic field configuration, particle acceleration mechanisms, and jet orientation [19].

1.6.2 Inverse Compton Scattering in AGN Jets

IC scattering is another key radiative mechanism in AGN jets, particularly responsible for the high-energy (X-ray to γ-ray) emission observed in many AGN, including FSRQs and BL Lac objects. In this process, relativistic electrons transfer part of their kinetic energy to low-energy photons, upscattering them to much higher energies [35].

There are two main sources of seed photons in AGN jets: synchrotron photons produced within the jet itself (SSC), and photons from external regions such as the accretion disk, broad-line region, or dusty torus (EC). The dominance of SSC or EC mechanisms depends on the AGN subclass and the location of the emission region within the jet [36].

The IC component forms the high-energy hump in the SED of blazars and is crucial for interpreting γ-ray observations from instruments like *Fermi*-LAT and ground-based Cherenkov telescopes (e.g., MAGIC, H.E.S.S., VERITAS).

Figure 1.3 illustrates the multi-component model of high-energy emission in AGN jets. The broadband SED features a low-energy bump due to synchrotron emission from relativistic electrons spiraling in magnetic fields, and a high-energy bump primarily attributed to inverse Compton processes. In this model, both SSC and EC contributions are included, with the EC component clearly dominating the gamma-ray regime. This configuration is particularly relevant for blazar-type AGNs, where external photon fields (e.g., from the broad-line region or dusty torus) play a significant role in shaping the observed spectrum.

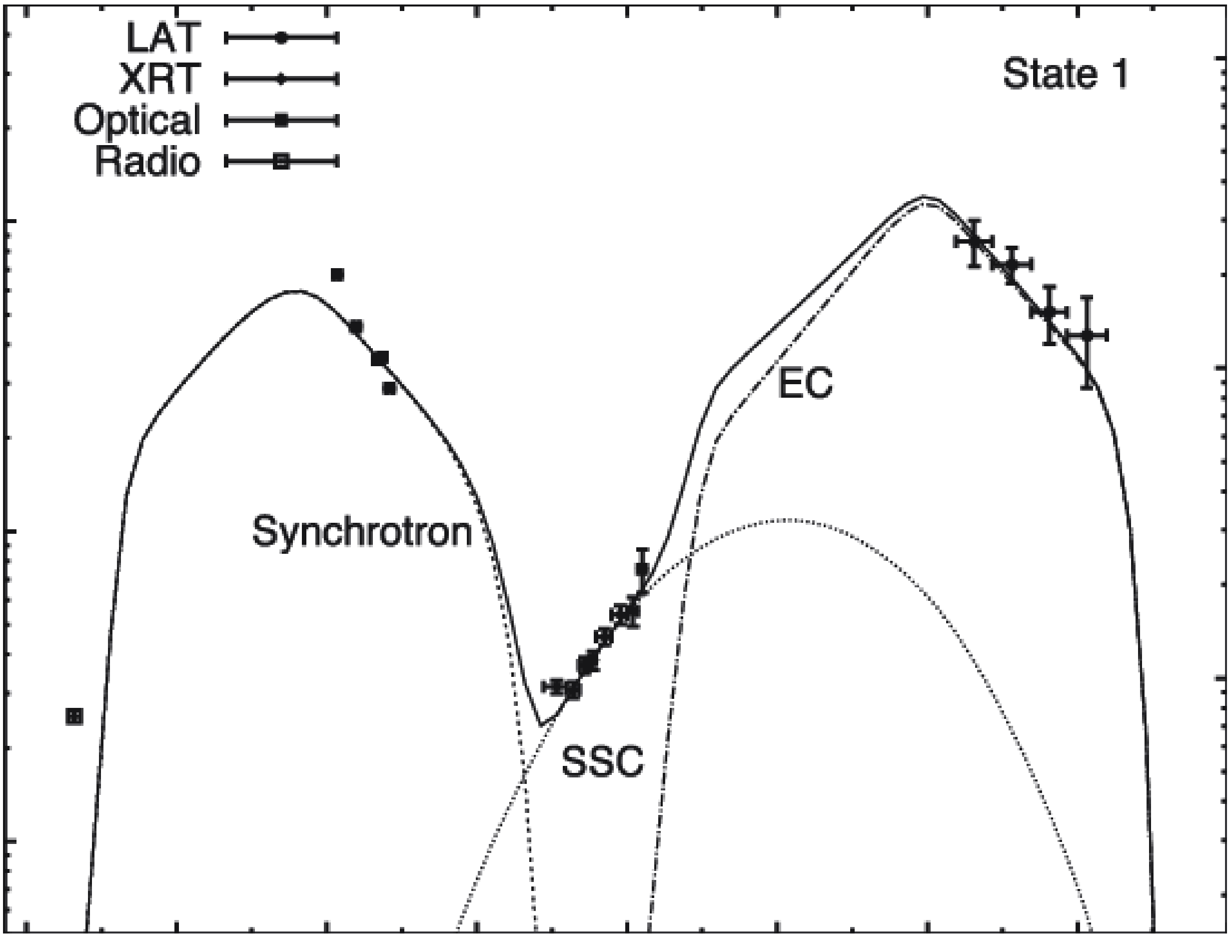

Figure 1.3: Modeled SED of an AGN jet during a flaring state, showing individual emission components: synchrotron (dashed line), Synchrotron Self-Compton — SSC (dotted line), and External Compton — EC (dash-dotted line). The solid curve represents the total model fit. The EC component clearly dominates the high-energy regime, while synchrotron and SSC contribute at lower energies. Taken from [37].

Chapter 2

Gamma-Ray Propagation and Flux Attenuation

When gamma rays, the highest-energy form of electromagnetic radiation, propagate through interstellar and intergalactic space, their intensity can be attenuated primarily through interactions with ambient radiation fields, such as the extragalactic background light (EBL) and the cosmic microwave background (CMB). These interactions are dominated by processes such as electron–positron pair production.

The degree of attenuation depends on the energy of the gamma rays and on the spectral and spatial properties of the intervening radiation fields. By analyzing attenuation signatures in gamma-ray spectra from distant astrophysical sources, such as gamma-ray bursts and active galactic nuclei, astronomers can study the properties of the intervening radiation fields, such as EBL, which in turn helps disentangle the intrinsic emission of the sources from propagation effects. A proper understanding of gamma-ray attenuation is therefore essential for interpreting observations from gamma-ray telescopes and for constructing accurate models of the high-energy universe, providing key constraints on cosmic background radiation and particle acceleration processes.

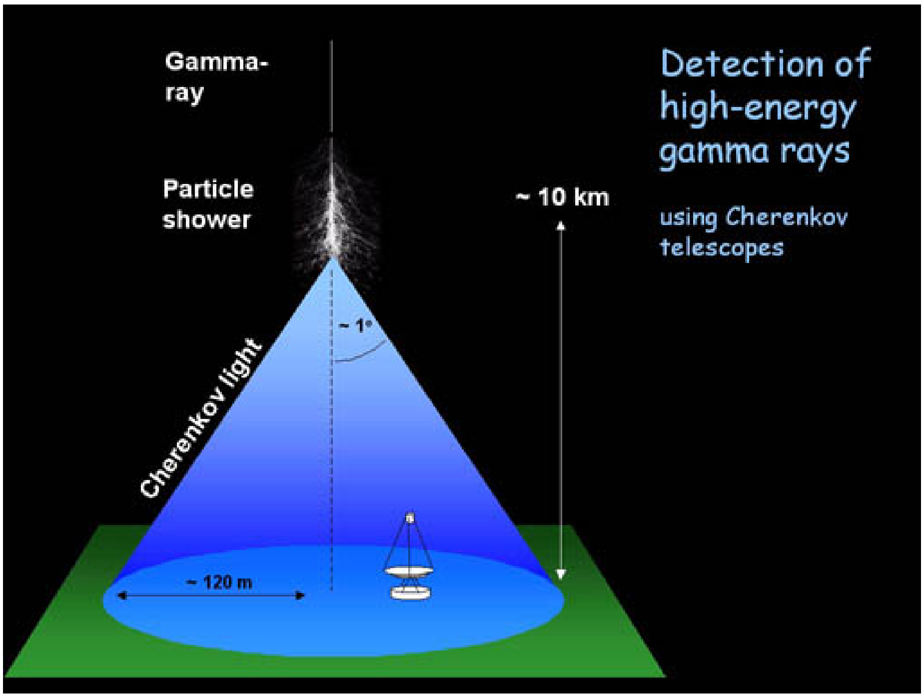

Figure 2.1: A sketch of a γ-ray induced shower and the Cherenkov light pool it creates. Image credit: H.E.S.S. - The High Energy Stereoscopic System [38].

2.1 Cherenkov Radiation

If a relativistic charged particle travels through the transparent dielectric medium with refractive index $n > 1$ at a velocity that exceeds the speed of light in that medium ($v > c_n$), then Cherenkov radiation is emitted. The light produced in the process is self-coherent and emitted at the Cherenkov angle θ_C. The relationship between the angle at which the flash will be emitted (θ_C) and the energy is given by relation:

$$\theta_C = \arccos \frac{1}{n\beta} \, . \tag{2.1}$$

In order for an electron to induce Cherenkov radiation in air that is observable at sea level, it must have incident energy $E_{\text{electron}} \geq 21\,\text{MeV}$. Refraction index n at sea level is $n \approx 1.0003$, so the radiation angle of the Cherenkov flash relative to the particle's direction of propagation will be small ($\theta_C \approx 0.1$ deg). β is the ratio of the particle's velocity to the speed of light in vacuum, i.e. $\beta = v/c$.

Each electron in the particle shower near the ground emits about 45 Cherenkov photons for every meter traveled. Particle shower of primary γ-rays of energy 1 TeV will result in about 100 Cherenkov photons per m^2 on the ground. The relative difference between the speed of the particles in the shower and the speed of light in the air is about 10^{-4}, so the Cherenkov flash of the air-shower will last only a few nanoseconds. Only a small fraction of the primary particle's energy (10^{-4}) will be converted into Cherenkov radiation. Cherenkov radiation from an electromagnetic air-shower is illustrated in Figure 2.1.

Cherenkov light is detected on the ground by instruments equipped with sensors sensitive to visible and near-UV wavelengths. However, the effective observation time is limited to approximately 1200 hours per year, primarily due to the necessity of clear, moonless nights. Additionally, factors such as moonlight, weather conditions, and light pollution degrade the quality of Cherenkov light detection and reduce observational sensitivity.

2.2 Imaging Atmospheric Cherenkov Telescopes

From the ground, γ-rays are observed using *Imaging Atmospheric Cherenkov Telescopes* (IACTs), which detect Cherenkov radiation in the atmosphere produced by extensive air showers (EAS) initiated by high-energy particles. Strictly speaking, IACTs are optical telescopes, as their cameras consist of photomultiplier tubes (PMTs).

The first IACT was the 10-meter Whipple telescope, which began operating in 1968. In 1989, it was used to detect very-high-energy (VHE) γ-radiation from the Crab Nebula [39], and in 1992 from Markarian 421, making it the first AGN detected in the VHE regime [40].

Observations using multiple telescopes were introduced by the *High Energy Gamma-Ray Astronomy* (HEGRA) collaboration, whose array operated from 1987 to 2002 [41]. Two of today's major collaborations, *High Energy Stereoscopic System* (H.E.S.S.)[1] and

---

[1] www.mpi-hd.mpg.de/hfm/HESS/HESS.shtml

Major Atmospheric Gamma Imaging Cherenkov Telescopes (MAGIC)[2], were founded from the HEGRA legacy. The MAGIC telescopes were built on the site of the former HEGRA installation at the Observatorio del Roque de los Muchachos, on the Canary Island of La Palma in Spain, while the H.E.S.S. telescopes were constructed in Namibia. Another major collaboration, the *Very Energetic Radiation Imaging Telescope Array System* (VERITAS)[3], is the successor to the Whipple collaboration.

PMTs, commonly used in IACTs, are typically sensitive to wavelengths in the range of 300–700 nm. Although the intrinsic sensitivity depends on the detector design, the effective detection window is primarily shaped by atmospheric transmission. While ozone absorption strongly suppresses ultraviolet photons below approximately 300 nm, its impact on Cherenkov light from extensive air showers is limited, since the ozone layer peaks at altitudes of about 20–30 km, whereas the shower maximum typically occurs at lower altitudes. At shorter wavelengths, Rayleigh scattering, whose cross section scales as λ^{-4}, plays a dominant role in reducing the Cherenkov photon flux reaching ground level. At longer wavelengths, the detected signal is increasingly dominated by the night-sky background above approximately 700 nm. A comparison of quantum efficiency curves for PMTs used in the MAGIC-I and MAGIC-II telescopes is shown in Figure 2.2.

It is important to note that IACTs use the Earth's atmosphere as a detection medium: although not a calorimeter in the traditional sense, it serves a similar function by enabling the development of particle showers whose Cherenkov light can be observed from the ground. In this sense, the technique of ground-based γ-ray detection is analogous to methods used in particle and nuclear physics experiments.

Currently, a new generation of Cherenkov telescopes is being developed under the *Cherenkov Telescope Array Observatory* (CTAO)[4], an international project aiming to build the most sensitive ground-based observatory for VHE γ-ray astronomy. The prototype of the Large-Sized Telescope (LST) was constructed on La Palma, near the still-operational

---

[2] www.magic.mpp.mpg.de

[3] veritas.sao.arizona.edu

[4] portal.cta-observatory.org

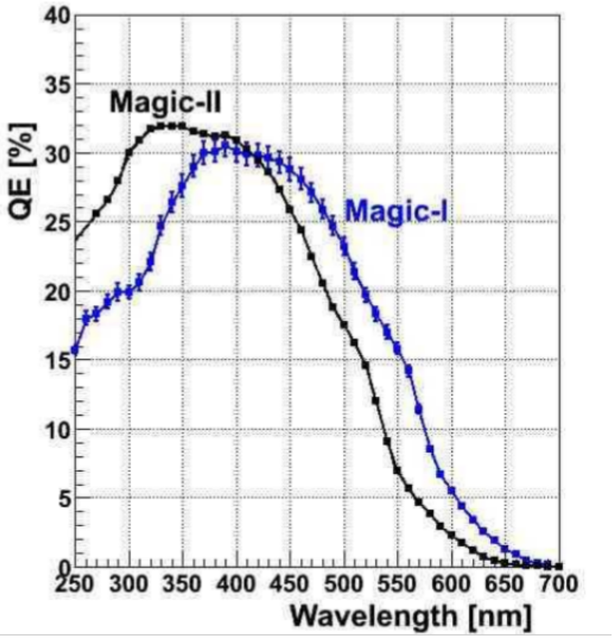

Figure 2.2: Comparison of quantum efficiency curves for MAGIC-I and MAGIC-II photomultiplier tubes [42].

MAGIC telescopes. CTAO will consist of two arrays, one in the northern and one in the southern hemisphere. To cover the full energy range from 20 GeV to 300 TeV, three types of telescopes will be used. The core energy range (150 GeV to 5 TeV) will be covered by 23 Medium-Sized Telescopes deployed across both sites. Additionally, 4 Large-Sized Telescopes will be installed in the northern array, and 37 Small-Sized Telescopes in the southern array, optimized for energies below 150 GeV and above 5 TeV, respectively [6].

In addition to IACTs, VHE γ-rays can also be detected from the ground using water Cherenkov detectors, such as the *High-Altitude Water Cherenkov Observatory* (HAWC) in Mexico and the *Large High Altitude Air Shower Observatory* (LHAASO) in China. Although primarily designed for cosmic-ray detection, the Pierre Auger Observatory in Argentina also uses water Cherenkov tanks and has contributed to high-energy photon studies.

2.3 Interaction between the Extragalactic Background Light and Very-high-energy Gamma Rays

The universe is filled with diffuse electromagnetic radiation of all wavelengths. Radiation in the infrared to ultraviolet range (0.1–1000 µm) is called Extragalactic Background Light (EBL). It is thought to originate from starlight, dust-processed starlight, and light emitted by active galactic nuclei. Very-high-energy (VHE) γ-rays interact with EBL photons, where they are converted into an electron–positron pair, and because of this, their flux on the way to Earth is attenuated [43]. The attenuation depends on the energy of the γ-ray and the redshift of the source (z). The relation between the measured and the intrinsic spectrum of the source is given by the relation:

$$\left.\frac{\mathrm{d}N(E)}{\mathrm{d}E}\right|_{obs} = \left.\frac{\mathrm{d}N(E)}{\mathrm{d}E}\right|_{int} e^{-\tau(E,\,z)}\,. \tag{2.2}$$

In this expression, $\frac{dN(E)}{dE}_{\text{obs}}$ and $\frac{dN(E)}{dE}_{\text{int}}$ represent the observed and intrinsic differential photon fluxes, respectively, as functions of energy E. The optical depth τ is given by:

$$\tau(E,\,z) = \int_0^z \mathrm{d}z'\,\frac{\mathrm{d}l(z')}{\mathrm{d}z'}\,\frac{1}{2}\int_{-1}^{+1}\mathrm{d}\mu\,(1-\mu)\int_{\epsilon_{th}}^{\infty}\mathrm{d}\epsilon'\,n_{EBL}(\epsilon',\,z')\,\sigma_{\gamma\gamma}\left(E(1+z'),\,\epsilon',\,\mu\right)\,, \tag{2.3}$$

with $\mathrm{d}l'/\mathrm{d}z' = c|\mathrm{d}t'/\mathrm{d}z'|$ which will be explained later in equation 2.8.

The first integral takes into account the distance traveled by the γ-ray, the second integrates over the scattering angle, where $\mu \equiv 1 - \cos\theta$ applies, and the third accounts for the probability of scattering. n_{EBL} is the photon density of the EBL in the given reference frame, and $\sigma_{\gamma\gamma}$ is the cross section for the formation of an electron–positron pair. The quantity ϵ_{th} represents the energy threshold of the reaction, which depends on the energy of the γ-ray and the interaction angle μ.

The condition for the photon–photon pair production process is given by [44]:

$$\sqrt{2\epsilon E(1-\cos\theta)} \geq 2m_e c^2\,, \tag{2.4}$$

where ϵ is the energy of the EBL photon, E is the energy of the γ photon emitted by an AGN at cosmological distance in the rest frame at redshift z, m_e is the electron mass, and θ is the interaction angle. The corresponding threshold energy ϵ_{th} is thus:

$$\epsilon_{th} \equiv \frac{2m_e^2\, c^4}{E(1-\cos\theta)}\,. \tag{2.5}$$

The cross section of this interaction reaches its maximum for photon energies around twice ϵ_{th}, which produces a peak at $\lambda = 1.24\,\left(\frac{E}{\mathrm{TeV}}\right)\,\mu$m [45]. Therefore, a γ-ray with energy 1 TeV interacts mainly with EBL photons of wavelength $\approx 1\,\mu\mathrm{m}$. This relation is essential for connecting the γ-ray attenuation with the EBL spectrum shown in Figure 2.3.

The number of galaxies per luminosity interval can be described by a luminosity function [46]:

$$j_{total}(\lambda,\, z) = \sum_i j_i(\lambda,\, z)\,. \tag{2.6}$$

Here, $j_{\mathrm{total}}(\lambda, z)$ is the co-moving luminosity density, representing the total energy emitted per unit time, per unit wavelength, per unit comoving volume, at wavelength λ and redshift z. The quantity $j_i(\lambda, z)$ denotes the contribution to the luminosity density from the i-th galaxy population or type.

The EBL flux seen by an observer at redshift z, due to the radiation emitted from z_{max} down to z, is obtained by integrating equation 2.6:

$$\lambda I_\lambda\,(\lambda,\, z) = \frac{c^2}{4\pi\lambda}\int_z^{z_{max}} j_{total}\;[\lambda(1+z)/(1+z'),\, z']\left|\frac{\mathrm{d}t}{\mathrm{d}z'}\right|\mathrm{d}z'\,, \tag{2.7}$$

Here, $\lambda I_\lambda(\lambda, z)$ denotes the spectral intensity of the EBL at wavelength λ and redshift z. This co-moving EBL spectrum is given in intensity units $[\mathrm{nW\,m^{-2}\,sr^{-1}}]$, while the factor $\mathrm{d}t/\mathrm{d}z'$ takes into account the assumed cosmology [47] and is given explicitly by:

$$\left|\frac{\mathrm{d}t}{\mathrm{d}z'}\right| = \frac{1}{H_0(1+z')\sqrt{\Omega_m\,(1+z')^3+\Omega_\lambda}}\,. \tag{2.8}$$

Term H_0 is Hubble's constant, whose current best local measurement is $H_0 = 73.04 \pm 1.04$ $\mathrm{km\,s^{-1}\,Mpc^{-1}}$, Ω_m is the mass density parameter which includes both baryonic and dark matter mass ($\Omega_m = 0.3$), and Ω_λ is the effective mass density of the dark energy ($\Omega_\lambda = 0.7$), taking the role described as the cosmological constant [48].
All parameters are derived from the ΛCDM[5] cosmology.

The contribution of different redshift intervals to the EBL can be directly calculated, along with the evolution of the EBL spectrum over cosmic time, by accounting for processes such as stellar emission, dust absorption and re-emission, and galaxy formation history [50]. The local EBL ($z = 0$) estimated by [50] by using equation 2.6 is shown in Figure 2.3. To accurately determine the attenuation for VHE γ-rays for the high-redshift universe and to account for the history of galaxy emission and the processes involved, it is crucial to understand the evolution of the EBL [50].

Figure 2.4 illustrates the contribution to the EBL from four representative galaxy populations, each characterized by a different SED, along with the co-moving EBL intensity as a function of redshift and predictions from several theoretical models. It should be emphasized that only about 30% of the starburst galaxy population contributes to the total galaxy population in the local universe (at $z \approx 0$), whereas at redshift $z = 2$, the co-moving bolometric EBL is dominated by starburst galaxies, contributing approximately 54% to the total EBL intensity. All these values are obtained through SED modeling and integration of the luminosity functions across redshift, based on observational data and semi-empirical galaxy evolution models.

It can also be noted that at these redshifts, the far-IR peak in the SED is higher than the near-IR peak; this is because a significant portion of the energy emitted by starburst systems is at far-IR wavelengths. The total bolometric intensity peaks at $z = 0.6 - 0.2$, as shown in Figure 2.4, where the far-IR peaks at more energetic wavelengths.

---

[5] ΛCDM (Lambda Cold Dark Matter) is a parameterization of the Big Bang cosmological model in which the universe contains three major components: first, a cosmological constant denoted by Lambda (Greek Λ) associated with dark energy; second, the postulated cold dark matter (abbreviated CDM); and third, ordinary matter [49].

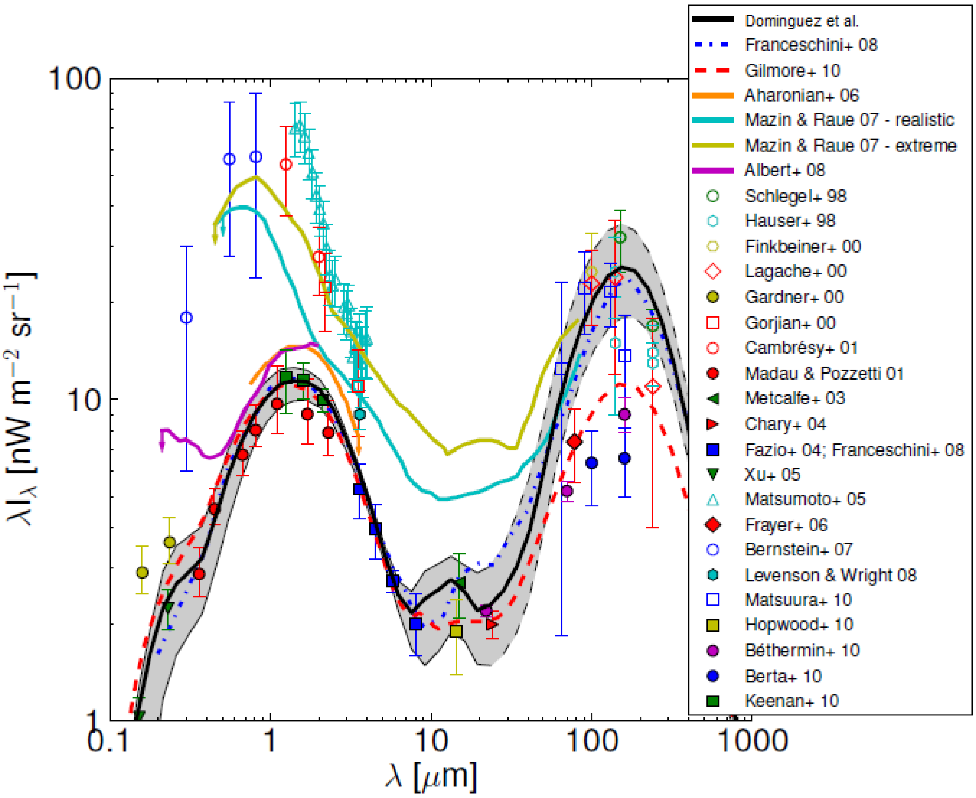

Figure 2.3: EBL models by various authors. The solid-black line is the EBL calculated by the fiducial extrapolation of the galaxy SED-type fractions for $z > 1$ made by [50]. Fits are based upon direct measurements of the whole EBL emitting range from 0.1–1000 µm performed by various authors indicated in the legend. Dashed lines are predictions from models by various authors, while the colored solid lines are upper limits from γ-ray astronomy using different blazars also mentioned in the legend. Uncertainties in the EBL estimation are shown with a shaded area. The envelope of the shaded region within the dashed line at wavelengths above 240 µm shows the region where there are no photometry measurements in available galaxy catalogues.

The aforementioned bolometric intensity I_{bol} is defined by:

$$I_{bol} = \int \nu I_\nu \, \mathrm{d} \ln \nu \,, \tag{2.9}$$

where ν is the frequency, and I_ν is the specific intensity per unit frequency. This is the

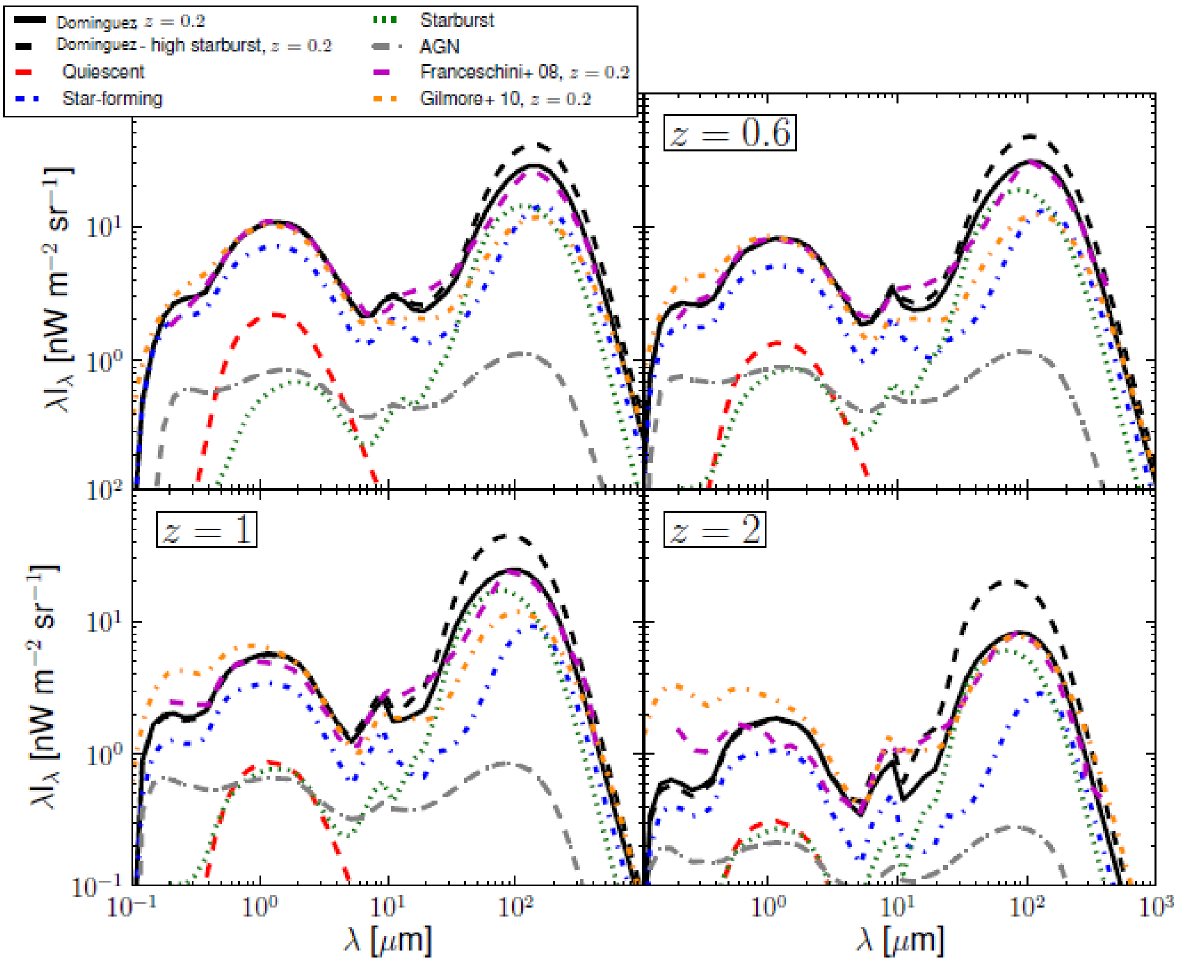

Figure 2.4: A model of Extragalactic Background Light in the co-moving frame at different redshifts, based on two assumptions for the extrapolation of the fractions for $z > 1$ [50]. The red-dashed line represents the contribution from quiescent galaxies, the blue dot-dashed line from star-forming galaxies, the green dotted line from starbursts, and the grey long-dashed line from AGN galaxies. The predictions by [51] and [52] are shown using the orange dot-dashed and magenta dashed lines, respectively.

total energy emitted per unit time and unit area by all galaxies across all wavelengths of the electromagnetic spectrum since the Big Bang.

Chapter 3

Atmospheric Properties

Dry air contains 78.08% nitrogen, 20.95% oxygen, 0.93% argon, and other gases in small quantities, including greenhouse gases such as water vapor, carbon dioxide, methane, nitrogen oxides, and ozone. Observations show that these gases are well mixed in nearly constant proportions up to altitudes of about 100 km [53]. Solid particles colloidally dispersed in the atmosphere that are its integral part are called aerosols. Aerosols are commonly classified as organic, mainly of natural origin, and inorganic, primarily of anthropogenic origin. Solar radiation is effectively scattered by air particles with sizes in the range of 0.1–1.0 μm, while particles with sizes of about 0.1 μm play an important role in cloud formation processes.

3.1 Layers of the Atmosphere

The atmosphere is subdivided into layers in the vertical direction according to the variation of temperature, pressure and density with altitude from the sea level. The temperature profile is determined by atmospheric absorption of solar radiation, and the decrease of density with height above sea level [53]. Additional classifications are made based on electromagnetic, radiative, and dynamic properties of the atmosphere, which are essential for understanding aerosol and optical measurements discussed in Chapters 4 and 6.

Division of the atmosphere according to electromagnetic properties:

- **Van Allen radiation belts:** The Van Allen radiation belts are two torus-shaped regions around Earth, held by its magnetic field, containing high-energy charged particles—primarily electrons in the outer belt and protons in the inner—originating from cosmic rays and solar wind, and are linked to aurora formation when these particles interact with the upper atmosphere.
- **Magnetosphere:** The Earth's magnetosphere, formed by the interaction of the solar wind with the Earth's magnetic field, traps charged particles and protects the planet from harmful solar radiation; it has an asymmetric, dewdrop-like shape, compressed on the Sun-facing side ($\sim$ 10–12 Earth's radii) and stretched into a long tail exceeding 200 Earth's radii on the opposite side.
- **Ionosphere:** The ionosphere is a region of Earth's upper atmosphere (50–600 km) that becomes ionized primarily by solar radiation, which ejects electrons from atoms and molecules and creates a plasma of free electrons and positive ions. Its structure varies with solar activity, time of day, season, and latitude. It is essential for atmospheric electricity, and forms part of the magnetosphere's inner boundary.

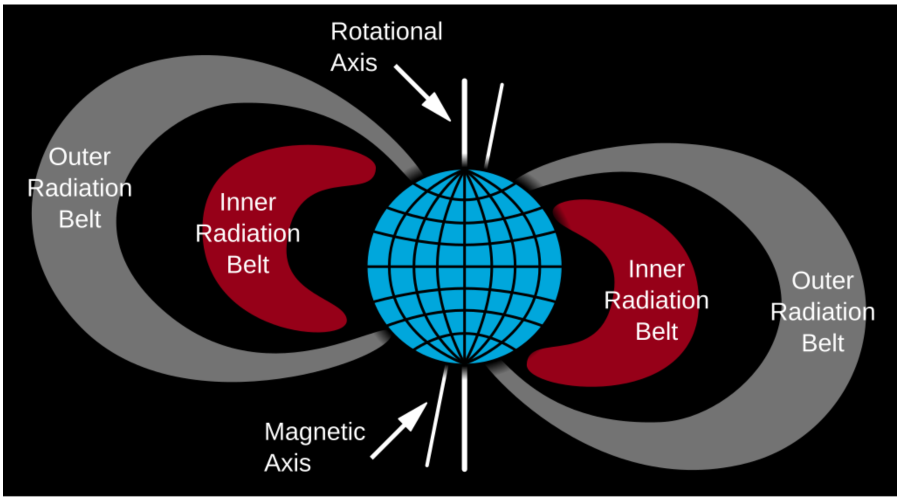

Figure 3.1: A cross section of Van Allen radiation belts [54].

Division of the atmosphere according to temperature:

- **Exosphere:** The exosphere is the outermost layer of Earth's atmosphere, starting at 800–3000 km above the surface, where extremely rarefied hydrogen and helium gases drift into space; temperatures can reach up to 1500 °C, and particles move at speeds around 11 km/s [55].
- **Thermosphere:** The thermosphere is the largest atmospheric layer, extending from 90 to 500 km, where temperatures rise up to 1500°C due to ionization by solar radiation; the air is extremely thin, and phenomena like the aurora occur within this layer (in Figure 3.2) [56].
- **Mesosphere:** The mesosphere lies between the stratosphere and thermosphere, roughly from 50 to 100 km altitude, with temperatures decreasing to below –100 $^{\underline{o}}$C at its upper boundary (mesopause). It experiences frequent atmospheric changes, and is where most meteoroids disintegrate, leaving metal traces; it sits above aircraft flight altitudes and below orbital spacecraft (in Figure 3.2) [57].
- **Stratosphere:** The stratosphere extends from approximately 18 km at the equator (8 km at the poles) to about 55 km. In this layer, temperature increases with altitude due to ozone absorption of UV radiation. This temperature inversion defines the tropopause and leads to the formation of multiple thermal tropopause events in certain meteorological conditions, which are relevant for high-altitude aerosol transport (in Figure 3.2).
- **Troposphere:** The troposphere is the lowest and densest atmospheric layer, extending from the surface up to 6–18 km depending on latitude, with temperature decreasing about 0.65°C per 100 m. It includes the planetary boundary layer (PBL), which is directly influenced by surface processes such as heating and friction, and dynamically evolves throughout the day. During nighttime, it collapses into a shallower *nocturnal boundary layer* (NBL) or *clear night boundary layer*, both relevant for aerosol dynamics and LIDAR returns (in Figure 3.2).

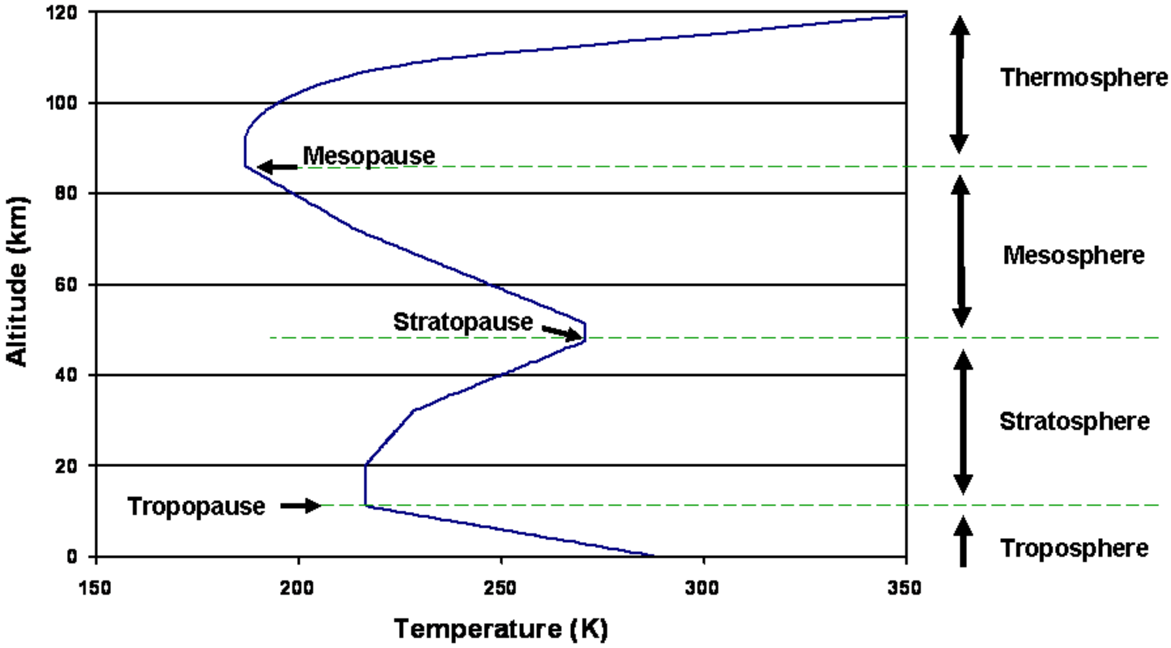

Figure 3.2: Thermal structure of the atmosphere [58].

Atmospheric properties such as air density and pressure also vary with altitude. At sea level, air density is approximately $1.225\,\mathrm{kg\,m^{-3}}$, while pressure decreases exponentially with height, following the barometric formula:

$$P_h = P_0 \ \exp\left(\frac{-mgh}{kT}\right), \tag{3.1}$$

where P_0 is the mean sea-level pressure ($\approx 1000\,\mathrm{hPa}$), m is the molecular mass, g is the gravitational acceleration, h is altitude, k is the Boltzmann constant, and T is temperature. The *temperature lapse rate* in the troposphere averages around $6.5\,^\circ\mathrm{C/km}$, although this rate can become negative in the tropopause, especially under inversion conditions common in marine boundary layers [59].

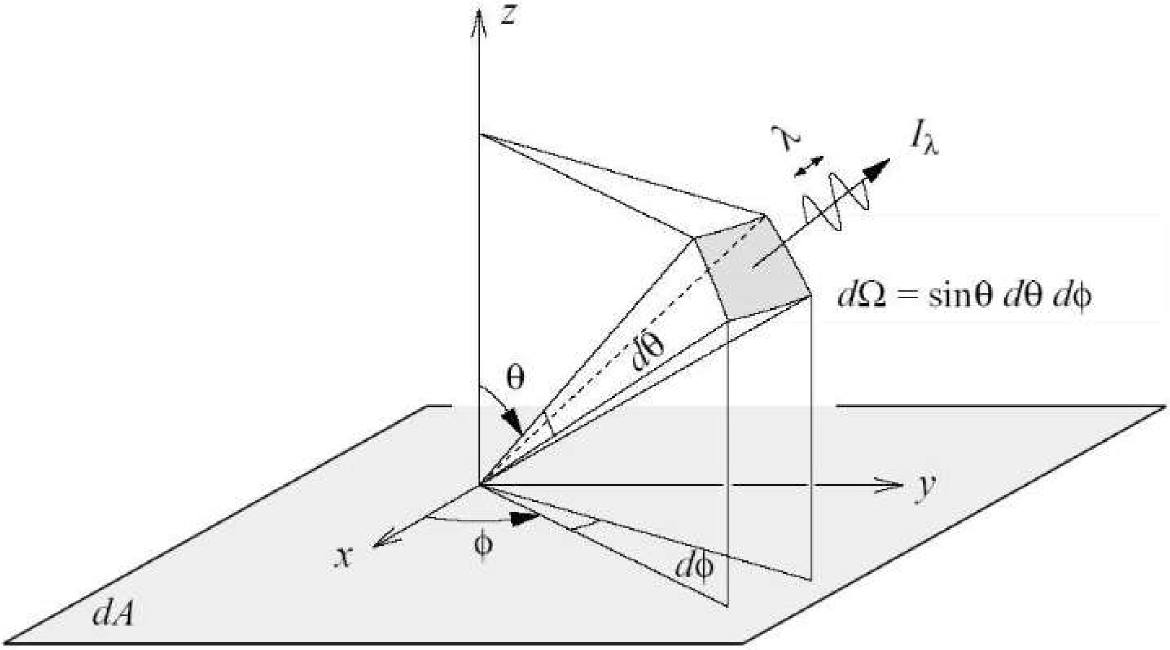

Figure 3.3: Intensity of the ray having wavelength between λ and $\lambda + \mathrm{d}\lambda$ that passes in time $\mathrm{d}t$ through the area $\mathrm{d}A$ into a solid angle $\mathrm{d}\Omega = \sin\Theta\, \mathrm{d}\Theta\, \mathrm{d}\Phi$ [14].

3.2 Propagation of Radiation Through a Medium

Intensity of the monochromatic radiation I_λ at the wavelength λ is defined as the amount of the energy $\mathrm{d}E_\lambda$ radiated at the wavelength between λ and $\lambda + \mathrm{d}\lambda$ through the surface area $\mathrm{d}A$ at an angle θ into a cone of solid angle $\mathrm{d}\Omega$ in a time interval $\mathrm{d}t$. The angle θ is measured from the direction perpendicular to the surface, so $\mathrm{d}A \cos\theta$ is the area $\mathrm{d}A$ projected onto a plane perpendicular to the direction in which the radiation is traveling (Figure 3.3). Therefore, intensity can be written as:

$$I_\lambda = \frac{\mathrm{d}E_\lambda}{\mathrm{d}\lambda\, \mathrm{d}A\, \mathrm{d}t \cos\theta\, \mathrm{d}\Omega}\,. \tag{3.2}$$

In vacuum, the intensity of radiation is conserved along a ray path. However, radiation interacts with the medium (dust, gas) via means of emission, scattering, and absorption processes. The characteristics of the medium also affect how radiation interacts with it; it is not solely dependent on the spectrum of the input radiation. As radiation travels through the medium, its intensity may be increased by emission and scattering into the beam, or it may be decreased by absorption or beam scattering. In the absorption and emission processes, respectively, opacity κ_λ and emissivity ϵ_λ define how radiation interacts with the medium. All processes that remove photons of a specific energy from the beam by interacting with the medium and lowering radiation intensity are collectively referred to as absorption.

Absorption processes are divided into:

1. scattering on the particles of the medium, when the photons are removed from the beam (e.g. Rayleigh scattering),
2. absorption of photons producing excitation of the particles in medium on higher energy levels (e.g. electron excitation in gas or phonon excitation in solid state).

With some approximations, the theory of electromagnetic scattering is applied to provide a fundamental description of the radiation scattering on the dust particles. In one-dimensional approximation, the rate of change of the radiation intensity $\mathrm{d}I_\lambda$ which travels through the medium of thickness $\mathrm{d}x$, with absorption properties determined by opacity or the absorption coefficient κ_λ, is proportional to the intensity of radiation I_λ:

$$\mathrm{d}I_\lambda = -\kappa_\lambda I_\lambda \mathrm{d}x\,. \tag{3.3}$$

The absorption coefficient, which is also known as the extinction coefficient $\kappa_{\lambda,\,ext}$, can be divided into two categories: the genuine absorption coefficient $\kappa_{\lambda,\,abs}$, which takes into account the nature of the processes involved, and the absorption coefficient $\kappa_{\lambda,\,scat}$ caused by beam scattering:

$$\kappa_{\lambda,\,ext} = \kappa_{\lambda,\,abs} + \kappa_{\lambda,\,scat}\,. \tag{3.4}$$

The total effective cross section σ_{lambda} for the absorption of photons of wavelength λ on N absorbers (particles of the medium) in the unit volume of the medium can be used to represent the absorption coefficient:

$$\kappa_\lambda = N\sigma_\lambda \,. \tag{3.5}$$

Absorption coefficient κ_λ depends on the nature of the interaction and characteristics of the medium such as: temperature, density and its composition.

The optical depth τ_λ is a dimensionless quantity that characterizes the attenuation of radiation due to absorption and scattering along its path. For a medium extending from the observer to a geometrical depth h, the optical depth at wavelength λ is defined as:

$$\tau_\lambda = \int_0^h \kappa_\lambda \mathrm{d}x \,. \tag{3.6}$$

The rate of change of intensity in equation (3.3) due to absorption can be rewritten using τ_λ instead:

$$\mathrm{d}I_\lambda = -I_\lambda \mathrm{d}\tau_\lambda \,. \tag{3.7}$$

By integrating (3.7) in the case of simple isotropic and homogeneous medium a well-known Beer law is obtained:

$$I_\lambda = I_{\lambda,0} \, \exp\left(-\tau_\lambda\right) . \tag{3.8}$$

Since intensity decreases by factor $1/\exp$ at geometrical depth on which $\tau_\lambda = 1$, the optical depth can be interpreted as the number of free mean paths of a photon passing through the medium, or as a number of scatterings or absorptions of photon on its way from the source to the observer. The attenuation of Cherenkov light in the atmosphere occurs both due to absorption and scattering.

3.3 Atmospheric Absorption

Earth's atmosphere is generally opaque to electromagnetic radiation, except in two "windows" of the spectrum, namely the optical window and the radio window (shown in Figure 3.4). Between the two is the infrared area of the spectrum, in which the atmosphere is

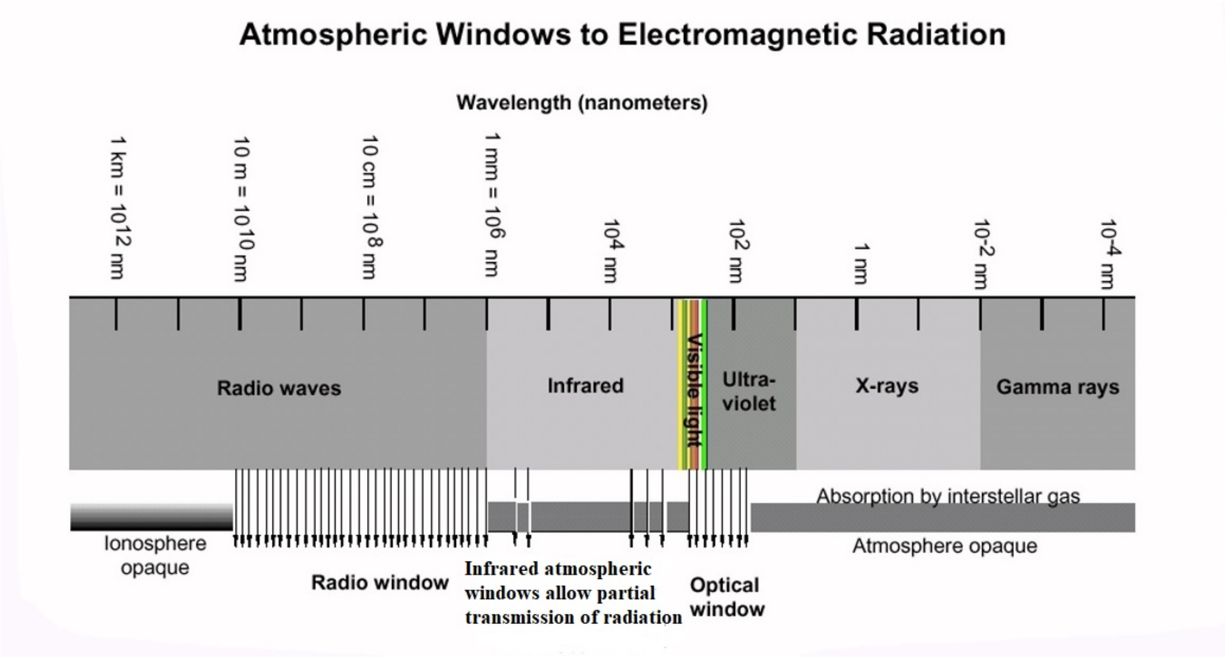

Figure 3.4: Atmospheric windows to electromagnetic radiation [60].

partly transparent (in limited bands) especially at great heights, where the presence of water vapor is very reduced. Several well-known near-infrared atmospheric windows also exist, including the J, H, K, L, and M bands commonly used in ground-based astronomy. In the ultraviolet, and even more so in X and gamma rays, the opacity of the atmosphere, at least at ground level, is total.

From a physical point of view, absorption occurs when the energy of radiation matches the allowed transitions of atomic or molecular electrons. Since these transitions occur at discrete energy levels, absorption takes place at specific wavelengths. In molecules, however, the energy levels are extremely numerous due to combinations of electronic, vibrational, and rotational states. As a result, absorption does not appear as isolated lines but rather as bands, composed of a dense series of closely spaced lines that can approximate a continuous spectrum over certain wavelength ranges.

Quantitatively it is possible to calculate the absorption by multiplying the density of column of air in the direction of the star considered (in atoms or grams per square centimeter) times the opacity of the air at that wavelength (in square centimeters per gram or per atom).

In this way the optical depth is obtained, whose natural logarithm gives the attenuation in nepers[1]. The column density of the individual gases is not easily calculated, both because the composition of the atmosphere varies with altitude, and because one of the most important sources of absorption, water vapor, varies greatly with meteorological conditions. Therefore, in the literature there are pre-calculated diagrams (or tables) for standard elevations and conditions, referring for example to the most important astronomical sites. As regards the atmospheric transparency in the infrared, it essentially depends on the column density of the water vapor, and therefore from the altitude (assuming optimal weather conditions). Desert sites and Antarctica are obviously favored.

3.4 Atmospheric Scattering

Unlike absorption that simply removes photons from a beam of radiation, scattering can change the beam direction, where it can be absorbed or scattered again. The intensity of the scattered radiation strongly depends on the wavelength λ and on the shape and the size of particle. For a spherical particle of radius d, scattering efficiency Q_λ can be represented as a function of a dimensionless size parameter x:

$$x = \frac{2\pi d}{\lambda}\,, \tag{3.9}$$

and the relative index of refraction n which is described as the ratio of the refractive index of the particle and the refractive index of the surrounding medium. The effectiveness of scattering depends on the size parameter. If the particles are relatively big compared to the wavelength of incident radiation, the particle-radiation interaction can be calculated

---

[1] The neper (symbol: Np) is a logarithmic unit for ratios of measurements of physical field and power quantities, such as gain and loss of electronic signals. The unit's name is derived from the name of John Napier, the inventor of logarithms. As is the case for the decibel and bel, the neper is a unit defined in the international standard ISO 80000. It is not part of the International System of Units (SI), but is accepted for use alongside the SI [61].

using basic optical principles, considering particle as a lens or a prism ($x \gg 1$). For x between 0.1 and 50, in which particle size is comparable to the wavelength, the extinction is explained by Mie theory [62]. For $x \ll 1$, Rayleigh scattering, that is strongly dependent on the wavelength of radiation, occurs. The Rayleigh scattering by molecules in the atmosphere and the Mie scattering by aerosols, haze and clouds are the most important for the attenuation of Cherenkov light [63].

3.4.1 Rayleigh Scattering

Rayleigh scattering occurs when the scattering particles are much smaller than the wavelength of the incident light; this equation is derived under that assumption:

$$\frac{d_{\text{molecules}}}{\lambda_{\text{Cherenkov}}} \approx 10^{-3}. \tag{3.10}$$

In the Rayleigh regime, the intensity of scattered light I_λ at a given wavelength λ is strongly dependent on both the size of the scattering particle d and the wavelength of the incident radiation. This relationship is described by the following proportionality:

$$I_\lambda \propto \frac{d^6}{\lambda^4}. \tag{3.11}$$

This equation indicates that the scattering intensity increases rapidly with particle size (as d^6) and decreases with the fourth power of the wavelength (as λ^{-4}). In the context of atmospheric Cherenkov radiation, this explains why shorter wavelengths (e.g., blue and UV) are scattered more strongly than longer wavelengths, contributing to the overall spectral shape and spatial distribution of detected Cherenkov light.

If a small homogeneous spherical particle of diameter d, which is much smaller than the wavelength λ of the incident radiation I_0, is considered, then the electric field of the incident radiation $\vec{E}_0$ induces a dipole moment $\vec{p}_0$ in the particle. According to classical electromagnetic theory, this relation can be expressed as:

$$\vec{p}_0 = \alpha \, \vec{E}_0 \, , \tag{3.12}$$

where α denotes the polarizability of the particle, quantifying how easily the particle's charge distribution can be distorted by the external electric field.

The scattered field at a distance r from a dipole is given by:

$$E = \omega\alpha \, E_0 \, e^{i\omega t} \, . \tag{3.13}$$

It represents the oscillating electric field induced in the particle, modeled as a driven harmonic oscillator with angular frequency ω. To describe the radiated (scattered) electromagnetic field observed at a distance r from this oscillating dipole, one must consider the solution of Maxwell's equations in the far-field (radiation) zone. The time-dependent dipole moment $\vec{p}(t) = \vec{p}_0 e^{i\omega t}$ acts as a source of electromagnetic waves. The radiated electric field $\vec{E}$ at a point located at distance r and in direction $\vec{r}$ is given by the expression [64]:

$$\vec{E}(\vec{r}, t) = \frac{\omega^2}{c^2 r} \, e^{i\omega\left(t - \frac{r}{c}\right)} \, \vec{r} \times (\vec{p} \times \vec{r}) \, , \tag{3.14}$$

where c is the speed of light.

This expression captures the spatial propagation of the dipole radiation as a spherical wave, with the $1/r$ decay of amplitude characteristic of radiated fields. The double vector product $\vec{r} \times (\vec{p} \times \vec{r})$ ensures the radiated electric field is transverse both to the direction of propagation $\vec{r}$ and the dipole moment $\vec{p}$. Thus, the transition from the simple oscillating field at the particle to the wave-like scattered field at distance r is achieved by solving Maxwell's equations for a harmonically oscillating dipole source and extracting the far-field asymptotic form of the solution.

With the assumption that the incident light is unpolarized, the intensity of the scattered light via Rayleigh's scattering is then given by:

$$I = \frac{\alpha^2 \omega^4}{c^4 r^2} \, \left(1 + \cos^2\theta\right) I_0 \, . \tag{3.15}$$

3.4.2 Mie Scattering

In most atmospheric conditions, aerosol particles are neither small enough for Rayleigh scattering to apply, nor large enough for classical geometrical optics to be valid. Instead, their interaction with light is accurately described by Mie scattering, which results from the full solution of Maxwell's equations for spherical particles [65]. Mie theory accounts for the scattering of electromagnetic waves by particles with dimensions comparable to the wavelength of the incident light.

Mie scattering is responsible for the optical behavior of a wide variety of atmospheric particles, such as dust, smoke, pollen, and especially water droplets that constitute clouds. The typical size of water droplets in clouds is on the order of $d \sim 10\ \mu$m, while the wavelength of visible light — and also of Cherenkov light — lies in the range $\lambda \sim 0.3$–$0.7\ \mu$m. Thus, the size-to-wavelength ratio is approximately:

$$\frac{d_{\text{droplet}}}{\lambda_{\text{Cherenkov}}} \approx 10\,, \tag{3.16}$$

which firmly places this scattering in the Mie regime (where the size parameter $x \gg 1$).

According to Mie theory, the interaction of light with a spherical particle is characterized by the scattering efficiency Q_{sca} and the extinction efficiency Q_{ext}, defined as:

$$Q_{\text{ext}} = \frac{\sigma_{\text{ext}}}{\pi r^2}\,, \qquad Q_{\text{sca}} = \frac{\sigma_{\text{sca}}}{\pi r^2}\,, \tag{3.17}$$

where σ_{ext} is the extinction cross-section, σ_{sca} is the scattering cross-section, and r is the radius of the droplet. These quantities are computed by solving Maxwell's equations for the boundary conditions at the surface of the particle, and they depend sensitively on the size parameter defined in equation 3.9:

For $x \gg 1$, scattering is efficient across the entire visible spectrum. Since all visible wavelengths are scattered with roughly equal efficiency, clouds consisting of millions of such droplets appear white under daylight illumination.

As shown earlier in Eq. (3.8), the attenuation of light intensity I_λ as it propagates through a scattering and absorbing medium is governed by the Beer–Lambert law. The optical depth τ_λ, defined in Eq. (3.6), represents the cumulative extinction (scattering and absorption) along the path and serves as a key parameter in quantifying radiative transfer through the medium.

In the case of tall clouds, this formalism directly applies. Light entering the upper layers of a cloud undergoes multiple scattering and absorption events, resulting in a gradual decrease in intensity with depth. As the optical depth increases ($\tau_\lambda \gg 1$), the transmitted intensity I_λ becomes significantly reduced compared to the initial intensity $I_{\lambda,0}$, consistent with Eq. (3.8).

Consequently, the base of the cloud appears darker — not due to intrinsic absorption, but because the majority of incident light has already been scattered out before it can reach the lower regions. This depth-dependent attenuation explains the characteristic appearance of clouds: bright white tops, where light is first scattered in all directions, and increasingly darker bottoms, where little direct light remains.

In summary, Mie scattering explains both the color and the brightness variation within clouds. The uniform scattering of all visible wavelengths produces whiteness, while the depth-dependent attenuation of light intensity due to multiple scattering events causes darkening at the cloud base.

3.5 Atmospheric Stratification and Aerosol Dynamics in Marine Environments

Understanding the vertical structure of the atmosphere is essential for interpreting radiative transfer processes and aerosol distributions, particularly in coastal and marine environments. Several key atmospheric layers and concepts directly influence the propagation of electromagnetic radiation and the interpretation of remote sensing data.

The *marine boundary layer* (MBL) represents a moist and thermally stable region near the ocean surface, commonly characterized by persistent temperature inversions. These inversions act to trap aerosols and suppress vertical mixing, leading to distinct layering of atmospheric constituents. Such conditions are particularly relevant in coastal regions, where they affect both satellite and ground-based retrievals [59].

Above the boundary layer lies the *dry free troposphere*, a region marked by lower humidity and reduced aerosol content. Despite its relative dryness, this layer plays a critical role in *long-range aerosol transport* and must be accounted for in optical modeling, especially under clear-sky conditions [59].

Temperature inversion layers, where temperature increases with altitude, further contribute to atmospheric stratification. These inversions, often observed during early morning hours or over oceanic regions, inhibit vertical mixing and enhance aerosol layering. Accurate identification and modeling of these layers are essential for interpreting atmospheric profiles, particularly in LIDAR observations [59, 66].

Another important concept is the *molecular atmosphere base height*, which denotes the altitude above which molecular (Rayleigh) scattering becomes dominant over aerosol scattering. This transition point is crucial for the calibration of remote sensing instruments and for modeling the molecular (background) contribution to extinction profiles [59].

Advanced radiative transfer models often assume a *stratified and spherically curved atmosphere*. These assumptions allow for more precise simulations of photon paths through the atmosphere, especially when dealing with *multi-angle satellite* or LIDAR observations. The curvature of the Earth and the vertical stratification of atmospheric constituents are both necessary for accurate retrieval algorithms [59, 66].

Standard atmospheric models, such as those derived from *Elterman profiles*, introduce empirical parameters including the *Elterman height* and *scale height*, which describe the vertical distribution of aerosol extinction and molecular density. These parameters serve as reference baselines and are frequently used for comparison with measured atmospheric profiles [67].

Finally, the *Ångström exponent* provides a measure of the spectral dependence of *aerosol optical thickness* (AOT) and serves as a proxy for aerosol particle size distribution [68]. It is a key parameter in aerosol classification and is integral to many aerosol retrieval algorithms across a range of remote sensing platforms.

3.6 Impact of Light Pollution on the Observatorio Roque de los Muchachos

The Roque de los Muchachos, located on the highest peak of the Canarian island of La Palma, is known as one of the best astronomical sites world-wide and lies between ∼2100 m and ∼2400 m a.s.l.

The site is distinguished by its high altitude above sea level and remarkably clean atmospheric conditions, which have been extensively characterized over the last 50 years [69, 70, 71, 72].

Aside from atmospheric conditions, professional observatories operate in a dark environment that is as free as possible from anthropogenic sources of light pollution that can degrade the quality of ground-based astronomical observations. Light pollution can be defined as any type of artificial light in the environment that is introduced directly or indirectly by humans. Avoidable light pollution refers to the nighttime luminous flux of artificial light sources that are inappropriate in terms of intensity, direction and/or spectral range. The problem also becomes ecological when artificial light is used in special places, such as natural areas or sensitive landscapes (see Figure 3.5) [73].

Figure 3.5: Nighttime light pollution on La Palma, mapped using VIIRS data from 2023 [74].

Chapter 4

Characterizing the Aerosol Atmosphere above the Observatorio Roque de los Muchachos

In the Canary archipelago a stable and robust temperature inversion layer (TIL) arises from the combination of large-scale atmospheric circulation on the descending branch of the Hadley cell [75, 76] and the Trade or "Alisios" winds originating from the Azores high area [77, 78]. The TIL's top is usually found at heights of approximately 1200m a.s.l. in summer and 1800m a.s.l. in winter [79, 59]. An "Alisio" inversion occurs when a temperature inversion can effectively divide the moist *marine boundary layer* (MBL) and the dry *free troposphere* (FT), two well-defined regimes, above each other. Approximately 80% of the time, this occurs [79].

The TIL weakens in the summer, and Saharan dust intrusions—also known as the "Calima" phenomenon—may happen. Higher aerosol densities are seen and the boundary layer may shift above the observatory [69]. At the ORM, dust intrusions last for about three to four days on average, but they can also last for two days or, in rare cases, up to five days [69]. Although dust intrusions can happen at any time of year, they are typically associated with June to October, with February to April seeing much fewer and less severe outbreaks [71]. Depending on where they originate — the Atlantic Ocean, the Sahara Desert, or Europe, respectively — dust particles are classified as *marine*, *desert*, or *anthropogenic aerosols* [76, 80].

Until now, measurements of aerosols at or above the observatories have been made using either direct dust counters and analyzers on the ground [81, 82, 83, 84, 85], on airplanes [86, 87], or integral light extinction measurements from the Sun [88, 71], or from reference stars [89, 90, 91, 92, 93, 94]. Although there has not been much success thus far, some attempts have been made to use satellite data for aerosol content monitoring at the observatories [95]. At ORM, a LIDAR measurement campaign was conducted across a range of characteristic scenarios [96]. Previous studies indicate that, under "calima" conditions, there is a predominance of relatively large particle sizes (> 1 µm), which results in gray (i.e., wavelength-independent) extinction. However, according to Kandler et al. 2007 [81], particles are generally non-spherical and exhibit a wide range of shapes.

All large, world-class observatories must operate in extremely dark environments, free from anthropogenic sources of light pollution, as such interference can significantly degrade the quality of ground-based astronomical observations.

To monitor and correct for the contribution of background light, a LIDAR system (Light Detection and Ranging) can be used. Specifically, it allows for the measurement of night-sky brightness and the subtraction of this contribution from the detected laser return signals. At the Observatorio del Roque de los Muchachos (ORM) on the Spanish Canary island of La Palma (28.78° N, 17.89° W, 2200 m a.s.l.), an elastic LIDAR system has been operating in semi-continuous mode, closely following the MAGIC Telescopes' observation schedule during nighttime.

Night-sky background rates measured under various atmospheric and illumination conditions have been used for continuous sky brightness monitoring. The results presented in this work are based on data collected using the MAGIC LIDAR system over a seven-year period, from March 2013 to March 2020. These measurements characterize the long-term evolution of night-sky conditions and their influence on ground-based observations.

Here, MAGIC's science data correction for aerosols and clouds within its field of view is predicated on two key assumptions:

1. The typical emission height of Cherenkov light from gamma-ray showers, as recorded by the MAGIC Telescopes, is typically found below the nocturnal boundary layer (refer to, for example, Fig. 10 of [97]). Thus, only its total transmission counts need to be determined while there is no need to resolve its structure.
2. When compared to the typical longitudinal shower profiles that span several kilometers, the vast majority of layers at higher altitudes can be regarded as thin. Therefore, only the overall transmission of the cloud layer needs to be resolved; their internal structure does not need to be resolved either [98].

For these reasons, retrieving the backscatter coefficient and achieving a range resolution finer than the geometric thickness of thin clouds are not essential. Instead, several other criteria define the required performance of a LIDAR system used in conjunction with Imaging Atmospheric Cherenkov Telescopes (IACTs).

These include good transmission resolution for optically thin aerosol and cloud layers, effective over distance ranges extending from the ground up to at least 25 km. Additionally, the system should be capable of pointing in any direction in the sky and must provide acceptable accuracy in the retrieval of atmospheric transmission.

During the night, the LIDAR is used in tandem with the MAGIC telescopes to point in the direction of the astrophysical sources that are observed by MAGIC (the fields of view are separated from each other by about 5 degrees so that the LIDAR's laser does not affect MAGIC's data acquisition). With the exception of the first two years of the system's regular operation and times during its upgrade, the coverage of MAGIC observations using LIDAR data is better than 85 %. The MAGIC telescopes themselves observe every night unless the relative humidity is greater than 90% or if the wind gusts are greater than 40 km/h.

The MAGIC site makes use of a number of additional monitoring instruments [100, 66, 101, 102]. Near the LIDAR dome on the roof of the MAGIC Counting House are

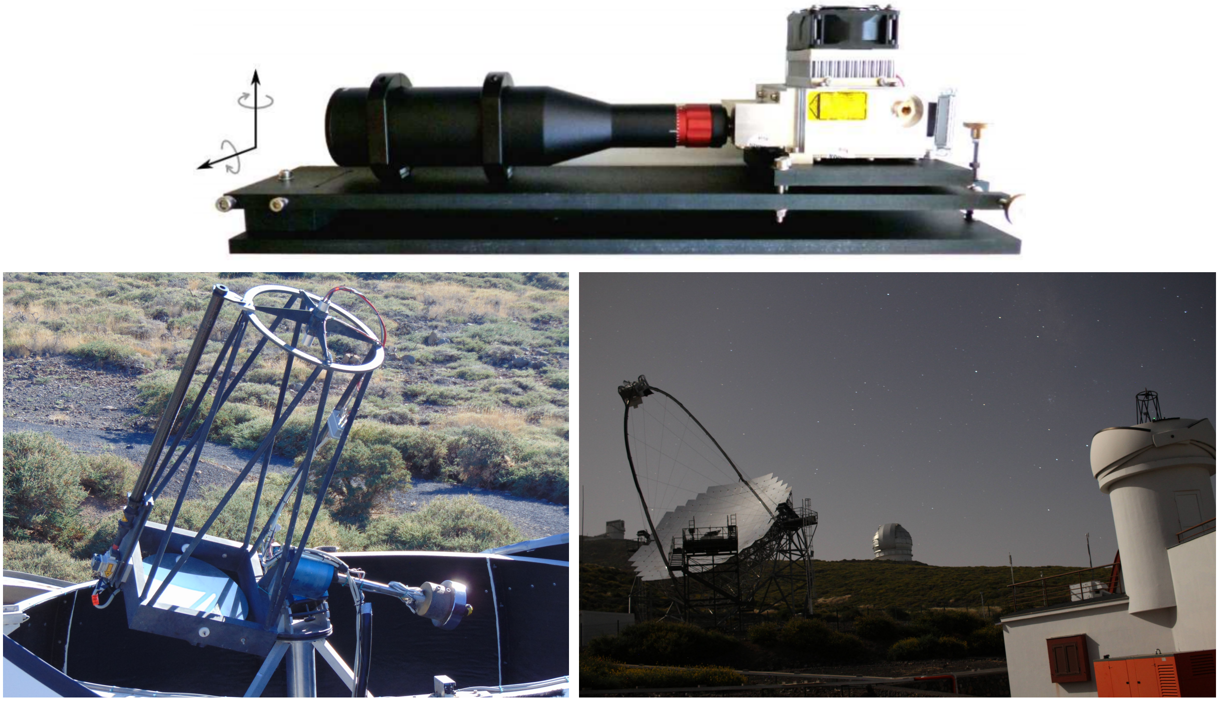

Figure 4.1: Top: Upgraded laser setup: the laser on the right is connected by cable to the laser controller in the LIDAR control room, the output beam of the laser (silver color box with a ventilator on top) is fed into the beam expander on the left. Both are mounted on a special plate assembly that can be easily adjusted in all directions to properly align the laser with the telescope and detector head. Bottom left: a picture of the LIDAR including structure, laser, mirror and light detector. On its left side, the baffle tube made of carbon-fiber is coupled to the exit lens of the beam expander. Its function is to block the scattered light from the laser and expander, which could directly hit the light sensor module of the LIDAR. Bottom right: a picture of one of the two MAGIC telescopes visible together with the MAGIC counting house with on top the opened dome in which the black structure of the LIDAR telescope can be seen [99].

an All-Sky camera and a commercial weather station. Furthermore, one of the MAGIC telescopes has an infrared pyrometer installed on its dish structure, pointing in the same direction as the telescope [102]. The weather station is read out every two seconds to determine whether the current circumstances are within the predetermined safety limits for operations. The MAGIC control programs maintain the cameras and telescopes in a safe state by monitoring the values and taking appropriate action if a safety limit is crossed. When the wind or humidity levels surpass those safety thresholds, the LIDAR control program verifies the data and shuts the LIDAR's dome. Every two minutes, the weather station data are archived for later analysis. There are also two Global Meteor Netork (GMN) cameras installed in April 2019 at the roof of the MAGIC counting house which are monitoring meteor activity every night throughout the year.

4.1 The MAGIC Micro-joule LIDAR System

The LIDAR is housed inside a protective dome above the LIDAR control room on the roof of the MAGIC counting house, which also houses computing and electronics for the main telescopes M1 and M2. The primary goal of LIDAR is to simultaneously monitor the atmospheric extinction profile of the observed field of view of the MAGIC telescopes during the nightly observations. For such monitoring, a 532 nm wavelength micro-Joule LIDAR system is employed (see 4.1).

The Cherenkov light detected by the MAGIC telescopes predominantly lies in the blue and near-UV region of the electromagnetic spectrum. At small zenith angles, its spectral distribution peaks around 320 nm. However, for a zenith angle of 15°, the median detected wavelength shifts toward longer wavelengths, reaching approximately 470 nm.

Given this spectral range, the use of a laser with a wavelength close to the effective range of Cherenkov detection is desirable for atmospheric calibration. Therefore, the third harmonic of an Nd:YAG laser at 355 nm represents a suitable compromise, falling within the relevant spectral window for Cherenkov light observed by MAGIC.

However, in the need for a safer and more practical handling and adjustment of a visible laser beam favored the use of the second harmonic at 532 nm, in combination with the use of an HPD with GaAsP photocathode, which for the wavelength range 500-600 nm provides an unprecedented quantum efficiency of $> 50\ \%$.

Using the derived atmospheric extinction to simulate Cherenkov light requires making certain assumptions about the local Ångström coefficient [1] and applying small wavelength-dependent corrections.

A low pulse energy was selected to reduce potential interference with MAGIC telescopes and other observatory operations on the ORM as well as to eliminate any potential safety issues, such as those involving eye safety. Fig. 4.2 depicts a rendering of the LIDAR with the primary hardware components. Table 4.1 provides more information on each component. Between 2014 and 2019, the system underwent a number of incremental upgrades, but overall functionality stayed the same.

The MAGIC LIDAR system is powered by a frequency-doubled, pulsed, passively Q-switched Nd:YAG laser with 5 µJ (25 µJ) of pulse energy and a 500 Hz (250 Hz) repetition rate. A photodiode integrated into the laser is used to activate the readout externally. The beam divergence is decreased to 10 mrad (12 mrad) using a 10 × (20 ×) beam expander. The laser setup is fixed atop a specially constructed assembly that enables quick and accurate laser alignment with the detector and LIDAR telescope.

To effectively reduce the beam divergence, the beam expander is positioned in front of the laser with as little gap as possible; however, dust particles on its exit window have the potential to scatter a very small amount of the laser light out of the beam. Even though the scattered light does not saturate the LIDAR detector, it may still find its way there and be discarded later on. Furthermore, scattered light originating from nearby air, the laser itself, or the beam expander may occasionally cause false triggers in the PMT cameras of the MAGIC telescopes. Nevertheless, at the level of basic data analysis, such events are easily distinguishable from genuine air-shower signals and can be reliably eliminated.

Detailed technical properties of LIDAR system and its configuration can be found in

---

[1] Ångström coefficient or Ångström exponent is a parameter that describes how the optical thickness of an aerosol typically depends on the wavelength of the light.

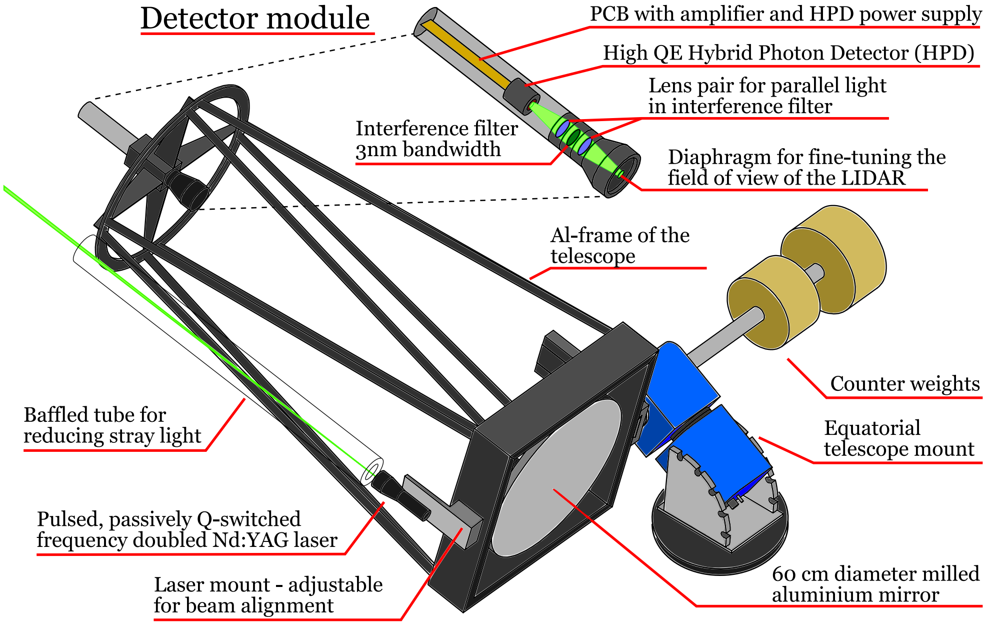

Figure 4.2: Hardware components of the MAGIC LIDAR system. Several individual components were modified or upgraded, but the overall scheme has remained the same [99].

[99].

Adapted signal inversion algorithm

The inversion of elastic LIDAR signals refers to the process of deriving atmospheric properties—such as the extinction or backscatter coefficient profiles—as a function of altitude, based on the measured return signal as a function of time (or range). This procedure has been extensively studied and documented in the literature [103].

In clean or barely turbid atmospheres, the accuracy of the aerosol inversion products is dominated by systematic uncertainties of the assumed molecular profile, and the molecular scattering contribution to the LIDAR return becomes significant, if not dominant. Numerous authors [104, 105, 106, 107, 108, 109, 110, 111, 112, 113, 114, 115] have all offered analytical solutions for a two-component atmosphere; however, none of them do so without making prior assumptions about the aerosol extinction-to-backscatter efficiency (LIDAR ratio) throughout the retrieval range. The single scattering LIDAR equation is

Table 4.1: Components of the LIDAR assembly before and after the major upgrade.

Component	Period 1 2013–2016	Period 2 since 2017
Telescope	Welded aluminum	
Mirror	Diamond-milled Al, 60 cm diameter, 150 cm focal length	
Mount	ASTELCO NTM-500 high precision equatorial robotic mount, 80 kg load capacity	
	Tracking accuracy: $5''$	
	max. acceleration: $10^\circ/\mathrm{s}^2$	max. acceleration: $20^\circ/\mathrm{s}^2$
Mount controller	ASCOM interface, driver control through LabView	
Laser	Teem Photonics STG-03E-1x0, 532 nm	Horus Lasers HLX-G-F001-11101, 532 nm
Pulse energy, Stability (rms)	5 µJ, 3%	25 µJ, 3%
Pulse duration (FHWM)	0.5 ns	1 ns
Beam divergence	10±2 mrad	12 mrad
Beam quality factor (M2)	1.3	1.2
Beam expander	10 ×, Thorlabs BE10M-A	20 ×, Thorlabs GBE20-A
Number of shots per data point, frequency	50 k, 500 Hz every 5 min	25 k, 250 Hz every 3 min
Baffle tube	–	1 m, 5 cm ∅, carbon fiber, 4 baffles
Light detector	Hamamatsu R9792U-40 HPD, QE ≈ 50% at 532 nm	
Detector module	Custom built PCB, Al case	Custom PCB, 3D-printed housing, Al case
Amplification	$2.6 \times 5 \times 10^2\,\mathrm{V\,A^{-1}}$	$\sim 390\,\mathrm{V\,A^{-1}}$ (differential, TI LMH6554)
Photon pulse FWHM	10 ns (2.1 ns without OpAmp)	2.3 ns
HV supply (7 kV, photocathode)	external (NIM module)	EMCO C series, external water-tight supply box
HV supply (400 V, AD)	Inside detector module	iseg APS, inside HV supply box
HV control	MCP Microchip DACs 4822 and 4922 series, 12-bit resolution, SPI controlled	
Temperature Compensation	Analogue	Software
FADC digitizer	Spectrum MI.2030, 8 bit, 200 MS/s	Spectrum M4i.4450-x8, 14 bit, 500 MS/s

usually the first step in the analysis of the LIDAR data:

$$N(r) = N_0 C G(r) \frac{A}{r^2} \beta(r) l \exp\left(-2 \int_0^r \alpha(r') \mathrm{d}r'\right). \tag{4.1}$$

where $N(r)$ is the number of observed photo-electrons detected within a digitization length l, corresponding to distances between r and $r + l$ of the back-scattered light. A is the geometrical area of the system (primary mirror of the LIDAR telescope), N_0 the number of photons emitted per laser pulse, C is the overall detection efficiency related to the experimental setup, $G(r)$ is the geometrical overlap factor, $\beta(r)$ is the local back-scatter coefficient and $\alpha(r)$ is the local extinction coefficient of the atmosphere. The local backscatter coefficient $\beta(r)$ and the local extinction coefficient $\alpha(r)$ characterize how the atmosphere interacts with the incident laser light at distance r. Specifically, $\beta(r)$ quantifies the fraction of light that is scattered back towards the LIDAR system per unit length and per unit solid angle, while $\alpha(r)$ represents the total attenuation of the laser beam due to both scattering and absorption along its path.

Both coefficients are composed of two main components:

- **Molecular scattering part** ($\beta_m(r)$ and $\alpha_m(r)$): This component arises from the scattering and extinction by air molecules, primarily nitrogen and oxygen. Molecular scattering follows Rayleigh scattering theory and is significant for particles much smaller than the wavelength of the light.

- **Aerosol scattering part** ($\beta_a(r)$ and $\alpha_a(r)$): This component is due to larger particles suspended in the atmosphere such as dust, smoke, pollen, and water droplets. Aerosol scattering can be described by Mie theory, which applies when particle sizes are comparable to or larger than the light wavelength.

Thus, the total backscatter and extinction coefficients are sums of their molecular and aerosol contributions:

$$\beta(r) = \beta_m(r) + \beta_a(r), \quad \alpha(r) = \alpha_m(r) + \alpha_a(r).$$

Furthermore, the extinction-to-backscatter ratio or the LIDAR ratio $S(r) = \alpha(r)/\beta(r)$ is introduced, for aerosols ($S_a(r)$) and molecules ($S_m = 8\pi/3$), respectively [116].

The inversion of the dual-component atmosphere [107, 108, 112, 117] in its non-logarithmic form [118] was used. In this formulation, the range-corrected LIDAR return (backscattered signal detected by the LIDAR system after emitting a laser pulse) is multiplied with a new function $Y(r)$:

$$Y(r) = S_a(r) \cdot \exp\left(-2\int_0^r \big(F(r') - 1\big)\alpha_m(r')\mathrm{d}r'\right), \tag{4.2}$$

where $F(r) = S_a(r)/S_m$. The LIDAR equation transforms then into

$$\begin{aligned} Z(r) &= \ln\big(N(r) \cdot r^2 \cdot Y(r)\big) \\ \frac{\mathrm{d}Z(r)}{\mathrm{d}r} &= \frac{1}{y(r)} \cdot \frac{\mathrm{d}y(r)}{\mathrm{d}r} - 2y(r), \end{aligned} \tag{4.3}$$

where the new variable $y(r)$ is defined as:

$$y(r) = \alpha_a(r) + F(r) \cdot \alpha_m(r). \tag{4.4}$$

Eq. 4.3 can be solved following the prescription of [119]:

$$\alpha_a(r) = -F(r)\alpha_m(r) + \frac{e^{(Z(r)-Z(r_f))}}{y_f^{-1} + 2\int_r^{r_f} e^{(Z(r')-Z(r_f))}\mathrm{d}r'}. \tag{4.5}$$

The LIDAR return can be calibrated almost always at reference points r_f of practically no aerosols and pure Rayleigh scattering (in case of MAGIC LIDAR at the ORM, few kilometers above ground). At these points,

$$y_f \simeq F(r_f) \cdot \alpha_m(r_f) \quad . \tag{4.6}$$

If the LIDAR operates at a zenith angle θ, it is sometimes useful to express Eq. 4.3 as a function of height $h = r/\xi$ with $\xi = 1/\cos\theta$ and $\mathrm{d}h/\mathrm{d}r = 1/\xi$:

$$\frac{\mathrm{d}Z(h)}{\mathrm{d}h} = \frac{1}{y(h)} \cdot \frac{\mathrm{d}y(h)}{\mathrm{d}h} - 2\xi \cdot y(h), \tag{4.7}$$

with the solution

$$\alpha_a(h) = -F(h)\alpha_m(h) + \frac{e^{(Z(h)-Z(h_f))}}{y_f^{-1} + 2\xi \int_h^{h_f} e^{(Z(h')-Z(h_f))} \mathrm{d}h'} \quad . \tag{4.8}$$

4.2 An Absolute Calibration of the LIDAR Return Signal

The system constant C_0 of the LIDAR depends on several instrumental and observational factors, including laser power, mirror reflectance, photon detection efficiency, and the efficiency of signal processing and analysis. It is defined as

$$C_0 = \ln\left(N_0 A l \langle \beta(h_{\text{LIDAR}}) \rangle\right), \tag{4.9}$$

where N_0 is the number of photons emitted per laser pulse, A the effective mirror area, l the digitization length, and $\langle \beta(h_{\text{LIDAR}}) \rangle$ the average backscatter coefficient at the LIDAR reference altitude h_{LIDAR}.

For calibration, it is assumed that the overlap factor — which quantifies the geometrical overlap between the laser beam and the telescope field of view — equals one. This means the full laser beam is within the receiver's field of view, ensuring that all backscattered photons from the probed volume are collected. Only data acquired under conditions of full overlap and free from detector saturation are considered reliable for calibration.

Using this approach, the system constant was determined for two measurement periods as $C_0 \approx 16.56 \pm 0.15$ for Period 1 and $C_0 \approx 18.87 \pm 0.15$ for Period 2.

Degradation of the mirror and diaphragm, as well as hardware or software changes, affect C_0. Variations have been noted after hardware installations, mirror cleanings, and updates to the photo-electron counting algorithm. A total of 24 hardware intervention periods were recorded between 2013 and March 2020, with 8 unlogged changes. Temperature and humidity may also influence the system constant.

To improve C_0 accuracy, a method was developed combining absolute LIDAR calibration during clear nights and a *calibrated degradation proxy.* This proxy assumes a two-stage exponential drop in aerosol extinction coefficient $\alpha_{\text{aer}}(h)$ with altitude during clear nights, allowing extrapolation to near-ground altitudes. The vertical aerosol optical depth (VAOD) is expressed as:

$$\begin{aligned} VAOD_{\text{clear night}} &= \int_0^\infty \alpha_{\text{aer}}(h)\,\mathrm{d}h \\ &= \int_0^{H_{\text{PBL}}} \alpha_0 \cdot \exp\left(-\frac{H_{\text{PBL}}}{H_{\text{aer}}}\right) \cdot \exp\left(-\frac{(h-H_{\text{PBL}})}{H_{\text{Elterman}}}\right)\mathrm{d}h \\ &\quad + \int_{H_{\text{PBL}}}^\infty \alpha_0 \cdot \exp\left(-\frac{h}{H_{\text{aer}}}\right)\mathrm{d}h \\ &= \alpha_0 \cdot \exp\left(-\frac{H_{\text{PBL}}}{H_{\text{aer}}}\right) \cdot \left\{ H_{\text{Elterman}} \cdot \left(\exp\left(\frac{H_{\text{PBL}}}{H_{\text{Elterman}}}\right) - 1\right) + H_{\text{aer}} \right\}, \end{aligned} \tag{4.10}$$

where $H_{\text{Elterman}} = 1.2$ km, H_{aer}[2] is the fitted aerosol scale height, and $H_{\text{PBL}} \approx 800\,\text{m} \cdot (\cos\theta)^{0.6}$ is the transition height. The retrieved values of $\alpha_{\text{aer}}(h)$ are fitted to an exponential decay above H_{PBL}[3], with selected data yielding acceptable fits.

The vertical aerosol optical depth derived from the Rayleigh fit is given by:

$$VAOD_{\text{Rayleigh fit}}(C_0) = \frac{(C_0 - C)\cos\theta}{2}\,. \tag{4.11}$$

A **proxy for the system constant** is formulated as:

$$P(C_0) := \frac{2 \cdot VAOD_{\text{Rayleigh fit}}(C_0)}{\cos\theta} + C\,. \tag{4.12}$$

This proxy indirectly accounts for the exponential decay model used for α_{aer}. To analyze changes in C_0 over time, two related expressions of the degradation proxy are defined:

$$P(\Delta C_0) := \frac{2 \cdot VAOD_{\text{exp. fit}}(C_0)}{\cos\theta} + C - C_{0,\text{initial}} \tag{4.13}$$

---

[2] Elterman height (also known as Elterman boundary layer height) is the altitude at which the planetary boundary layer (PBL) of the atmosphere ends.

[3] The planetary boundary layer (PBL) is the lower part of the atmosphere that is in direct contact with the Earth's surface. This layer extends from the surface up to an altitude that can range from several hundred meters to several kilometers, depending on weather conditions. The PBL is characterized by significant changes in temperature, wind speed, and other meteorological factors, as it is influenced by surface processes (such as daytime heating or nighttime cooling).

and

$$P\left(\frac{N_0 \cdot A}{N_{0,\mathrm{initial}} \cdot A_{0,\mathrm{initial}}}\right) := \exp\left(P(\Delta C_0)\right) \ . \tag{4.14}$$

These proxies allow for monitoring the system constant's degradation due to laser photon number and effective area changes.

4.3 Analysis of Seven Years of LIDAR Data

The data obtained over a seven-year period, from March 2013 to March 2020, using the MAGIC LIDAR is presented here. The LIDAR collected approximately 10^5 atmospheric profiles while operating in semi-continuous mode at night, closely adhering to the MAGIC Telescopes' observation schedule. The time coverage of these LIDAR data is displayed in Figure 4.3, first compared to the telescopes' observation up-time (complete lines), and subsequently compared to the total amount of available nighttime. The discrepancies are caused by the MAGIC Telescopes' reduced uptime, which occurs when the ground humidity reaches 90%, wind gusts exceed 40 km/h, the aerosol transmission falls to values well below 50% for an extended period of time (and when technical observations are not possible), or the telescopes require technical maintenance.

The LIDAR system is activated when astrophysical sources are observed at zenith angles below 70 degrees (above 20 degrees elevation) by the MAGIC Telescopes. Typically, LIDAR is not used in conjunction with the "very-large zenith angle" (VLZA) observation mode, which has grown in significance in recent years. The LIDAR's range is limited in that it cannot penetrate the area of the atmosphere where VLZA air showers originate. Also, LIDAR mount only reaches a certain zenith angle due to hardware limitations imposed by the LIDAR's dome. Observations made during the moonlight may not have sufficient LIDAR coverage if the Moon's background light overwhelms the instrument [120].

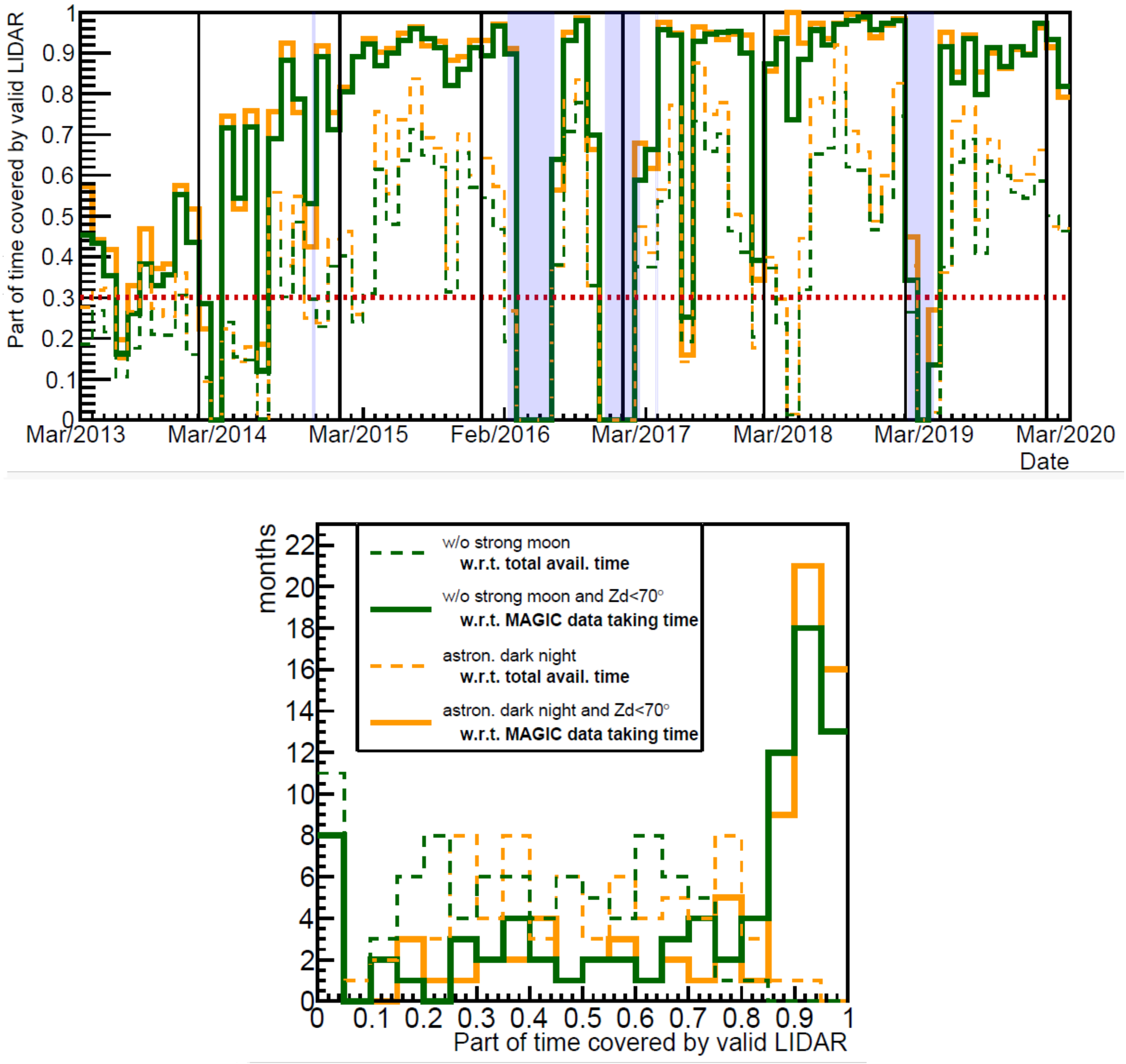

Figure 4.3: Coverage of the MAGIC LIDAR data as a fraction of the available time (dashed lines) or time actually used by the MAGIC Telescopes (full lines). Top: time-evolution of valid LIDAR coverage, every bin represents one month; in orange: valid LIDAR data taken during astronomical dark night, in green: part of the full night including astronomical twilight, after excluding strong moonlight and very high zenith angle ($\theta > 70^\circ$) observations. The blue shaded areas indicate the times when the LIDAR was not in operation. The dotted red line indicates the minimum full-time coverage required for a month to be included in the statistical analysis. Bottom: distribution of monthly LIDAR data coverage [99].

Because of this, Figure 4.3 displays two distinct scenarios: one using data collected at zenith angles below 70 during astronomical dark nighttime, when the LIDAR is expected to be operational continuously, and another using data collected during a period without a particularly strong moon. The MAGIC data, which should be accounted for contemporaneous LIDAR data, consistently achieve coverage levels well above 90% starting from 2015 due to the continuous hardware improvement. The blue shading designates three separate periods of system upgrades. In relation to the total amount of available nighttime, the overall coverage of LIDAR data during the night varies greatly and is highly dependent on the weather. Over time, there has been a general trend toward greater coverage, which is partially attributable to ongoing improvements in the MAGIC Telescopes' overall data-taking efficiency. Figure 4.4 shows the distribution of LIDAR pointing angles of the whole sample. The LIDAR has tracked the movement of multiple primary MAGIC observation targets across the sky, leaving a distinct signature. Nevertheless, with the exception of the northern and southern directions at large zenith angles, a significant portion of the sky has been observed and is represented in the dataset. When highlighting general atmospheric properties in the following sections, the entire data set will be used; otherwise, a subset of the data to derive some statistical properties will be used. The selection criteria have been set so that only months with a minimum of 30% nighttime coverage are included in statistical analyses. This criterion has been chosen to ensure sufficient overall statistics.

4.3.1 Aerosol Altitude Profiles of Clear Nights

Approximately 60% of the LIDAR data sample ($\sim 6 \times 10^4$ profiles) follows the ground layer aerosol extinction profile introduced in Eq. 4.10. This sample was collected during times when the LIDAR reached full overlap at less than 350 m. The profiles were categorized as representative for clear nights and further analyzed. Aerosol extinction scale heights H_{aer} ranging from 250m to more than 4000m were obtained for clear nights over seven years. The height dependence of aerosol extinction in a stratified atmosphere is independent of the direction of the LIDAR pointing. For the ORM, however, this is not the case. Figure 4.5

displays the distribution of fitted aerosol extinction coefficient scale heights as a function of a zenith angle of LIDAR pointing. In contrast to the stratification case, the scale heights do depend on the observation zenith angle, roughly given by;

$$H_{\mathrm{aer}} \approx H_{\mathrm{aer},0} \cdot (\cos\theta)^{\gamma} \;\; , \tag{4.15}$$

where the exponent parameterizes the curvature of the aerosol layer. A fully stratified atmosphere would reproduce $\gamma = 0$, whereas a round convex-shaped layer yields $\gamma = 1$. The average gamma value of $\gamma = 0.77$ indicates the intermediate shape of the aerosol ground layer at the ORM (see Table 4.2). Additional potential dependencies of H_{aer} on seasonal variations and azimuthal pointing directions are also indicated in Table 4.2. The aerosol layer has a smaller curvature in southern directions, as indicated by an average shallower drop in scale height with zenith angle. This is consistent with expectations given the elongated shape of the island of La Palma, where the ORM is situated near its northern edge. However, as was mentioned in the previous subsection, this result should be interpreted with some caution because of the significantly lower angular LIDAR coverage towards southern directions.

Apart from that, on clear nights, there is a faint indication of a slight seasonal dependency of the ground layer, with less stratification in the summer and a higher overall scale height. With a mean of roughly 870 meters, the vertical scale heights $H_{aer,0}$, exhibit an asymmetric distribution. It is represented in Fig. 4.6 and it can be fit to an exponentially modified Gaussian distribution.

4.3.2 Aerosol Transmission Statistics

With an absolutely calibrated elastic LIDAR it is possible to establish ground layer aerosol transmission statistics for observable night times.

In order to quantify a probability of occurrence of a given aerosol transmission, averaged over the seven years of data set, the month-wise (normalized) ground-layer probability of occurrence $P_{<T_{aer}}(m)$, obtained from those months with at least 30% absolute dark-night

Table 4.2: Results of fitting Eq. 4.15 to median aerosol scale heights H_{aer} for different azimuth pointing angles and separated by seasons. At the bottom, the total of all data are shown. Uncertainties are statistical only and do not take into account the effect of the assumption of a uniform LIDAR ratio across the ground layer. The months have been grouped in those of similar behavior. Note that September sometimes behaves rather like a summer month, whereas in other years it is more winter-like. In order to keep the small summer data sample clean, September is subsumed within the winter case.

	$H_{\mathrm{aer},0}$ (m)	γ
North	(581± 12)	(0.83 ± 0.04)
South	(552± 12)	(0.60 ± 0.04)
East	(553± 12)	(0.72 ± 0.04)
West	(578± 12)	(0.79 ± 0.04)
Winter (S,O,N,D,J,F)	(568± 12)	(0.75 ± 0.04)
Spring (M,A,M,J)	(580± 12)	(0.79 ± 0.04)
Summer (J,A)	(606± 12)	(0.88 ± 0.04)
All data	(577± 8)	(0.77 ± 0.03)

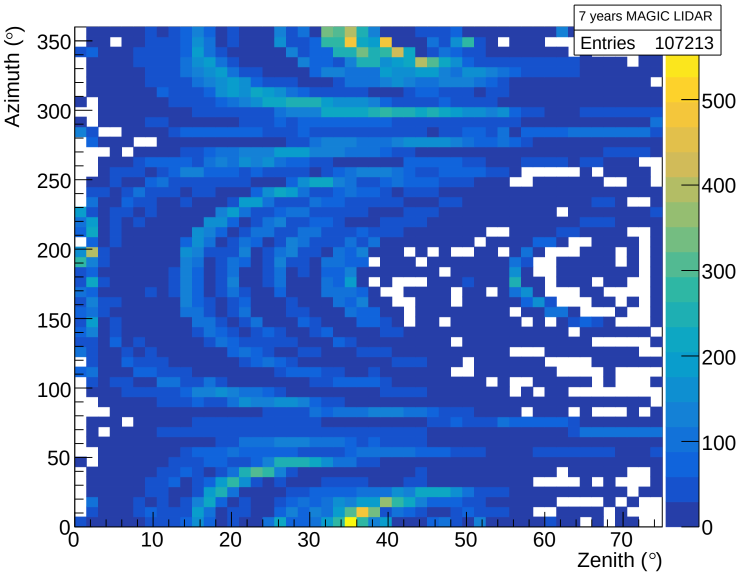

Figure 4.4: Distribution of LIDAR pointing angles of the analyzed data set. 0° azimuth corresponds to North, 90° to East [99].

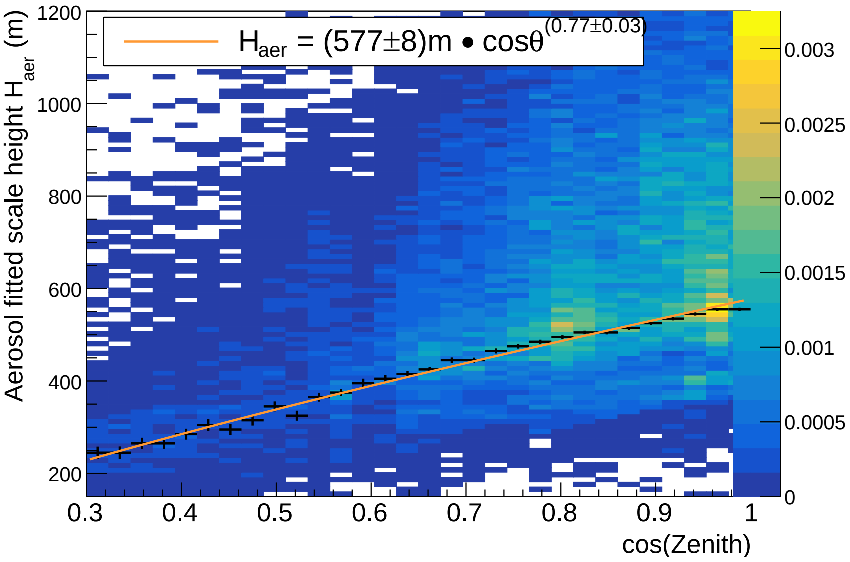

Figure 4.5: Distribution of fitted aerosol extinction coefficient scale heights H_{aer} (see Eq.4.15). The black crosses are located at the position of the weighted median at each bin and fitted to a linear dependency of the cosine of zenith angle [99].

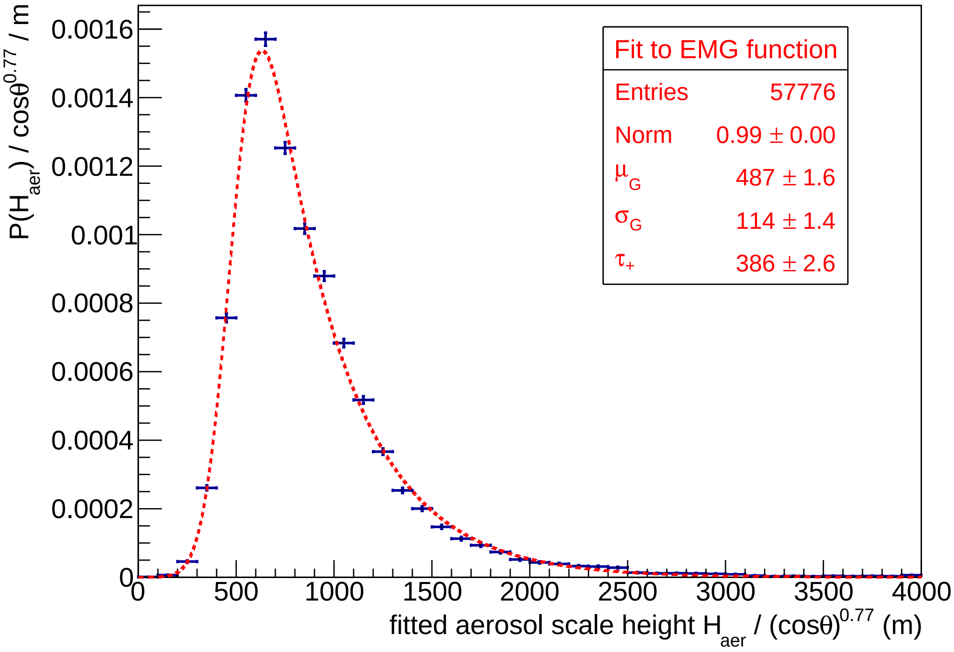

Figure 4.6: Distribution of zenith-corrected reconstructed aerosol extinction coefficient scale heights H_{aer}. The asymmetric distribution has been fitted to an exponentially-modified Gaussian probability distribution. Note that, due to the asymmetry of the distribution, its first moment of $(\mu_G + \tau_+) = 873 \pm 3\,\mathrm{m}$ does not coincide with the median used in Figure 4.5 and Table 4.2. Its standard deviation is $\sqrt{\sigma_G^2 + \tau_+^2} = 402 \pm 3\,\mathrm{m}$ [99].

coverage (as seen in Figure 4.3) has been calculated. To ensure that there are enough statistics for every month, this threshold has been set based on practical considerations of data availability and stability. It has been determined that the data from these months are adequately representative for the full month. Then, the probability distributions for each month were added and weighted as follows:

$$\begin{aligned} P_{<T_{aer}} &= \sum_{m=1}^{12} w(m)\, P_{<T_{aer}}(m) \Bigg/ \sum_{m=1}^{12} w(m) \quad \text{with :} \\ w(m) &= \epsilon(m) D(m) \ , \end{aligned} \tag{4.16}$$

where D_m is the average night-time available for a given month and $\epsilon(m)$ the average monthly data taking efficiency of the MAGIC Telescopes. The former provides higher numbers for the winter months, whereas the latter gives a somewhat higher weight to the summer months. The results for $P_{<T_{aer}}$ for various subsamples of the data are displayed in Figure 4.7. These subsamples include those for Periods 1 and 2 only, those divided by seasons, and the entire data set. Visible differences between Periods 1 and 2 arise at the level of occurrence probabilities of less than roughly 10%, which are likely the result of varying criteria for aborting the collection of data from the MAGIC Telescope, which grew more stringent over time. These requirements include, among other things, the application of the very large zenith angle (VLZA) observation types, which were introduced and have gained popularity in recent years, and involve aborting the collection of LIDAR data. Furthermore, aerosol transmission $T_{aer} < 0.4$ has frequently resulted in the cancellation of MAGIC Telescope science data collection, as such low transmission levels significantly reduce the telescope's sensitivity, leading to an increased systematic uncertainty that compromises the quality of the observations.

Therefore, there is more contamination of extremely poor ground-layer transmission in the Period 1 data set. A portion of the difference may also be explained by statistical fluctuations.

Additionally, Fig. 4.7 illustrates the unfavorable atmosphere that is obtained in the

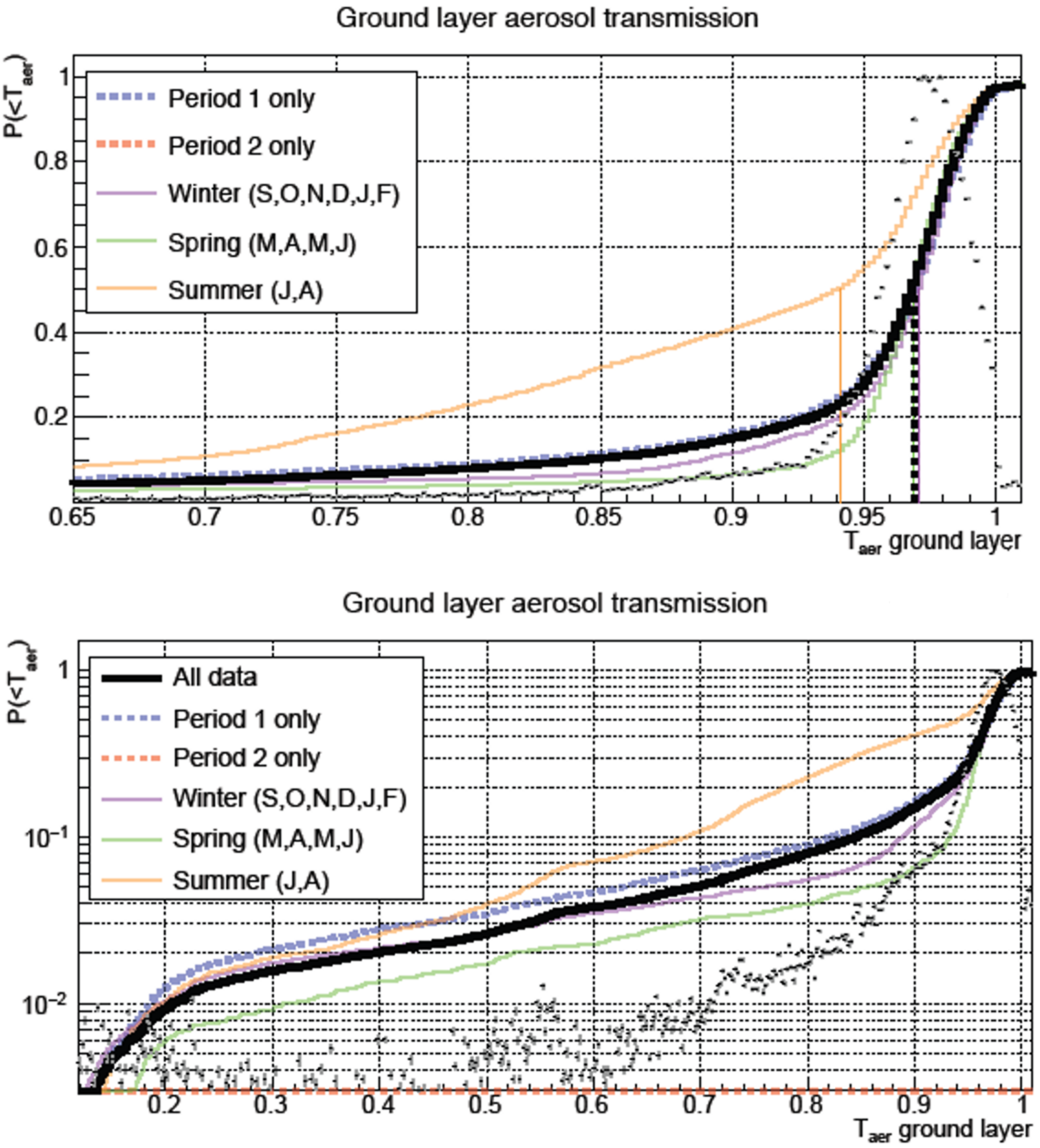

Figure 4.7: Cumulative vertical aerosol transmission probabilities of green light for ground-layer aerosols during MAGIC data taking conditions (RH $<$ 90%, wind gust $<$ 40 km/h) and weighted according to Eq. 4.16. The vertical lines refer to the medians of the distributions. Gray dots show the differential probability of the full data set, scaled to reach a maximum of 1 for better comparability. Top: in linear scale, Bottom: in logarithmic scale. Note the different axis ranges [99].

summer months of July and August. During these months, there is a lower median ground layer transmission, and occasionally, because of the recurring phenomenon of calima, transmission of green light falls below 70% [71]. March, April, May, and June are the spring months that typically have the best conditions. An overall occurrence of approximately 80% for the clear night was derived, taking into account $T_{aer} \approx 0.93$ as the approximate transition between the normally-distributed clear nights and non-clear nights (nights with higher aerosol load or outliers). This number is marginally less than the 84% TIL occurrence for the Western Canary Islands reported by [59], yet remains consistent with that result when taking into account differences in observational coverage, instrumentation, and local atmospheric variability. Employing the gradient method as described in [121]. Figure 4.8 displays the frequency of occurrence of molecular atmosphere base heights h_t and, for comparison, the Planetary Boundary Layer. The significant elevation-related exponential tails of the clear-night ground-layer aerosol density can be used to explain the differences between the two. The gradient method was unable to determine the PBL in approximately 25% of the cases, as the height at which full LIDAR overlap is reached and the first derivative's minimum coincide, leading to the latter's artificial determination.

Lastly, the frequency of vertical aerosol transmission probabilities from various altitudes to the ground is shown in Figure 4.9. These values are required in order to calculate the effects of clouds and aerosols on the Cherenkov light, which is emitted between the displayed altitudes by gamma-ray induced air showers. Clouds in the field of view are the reason for the differences between 6 and 9 kilometers above ground. It is also evident that clouds have less of an impact above 9 km (11.2 km a.s.l.).

4.3.3 The Effect of Clouds above the ORM

In the past, photometry measuring atmospheric extinction has been the primary method used to investigate the impact of clouds above the ORM [94]. However, the majority of these (narrow-band filter) observations do not allow to discriminate between dust and clouds. When clouds are found above roughly 6000 meters above sea level, they are most

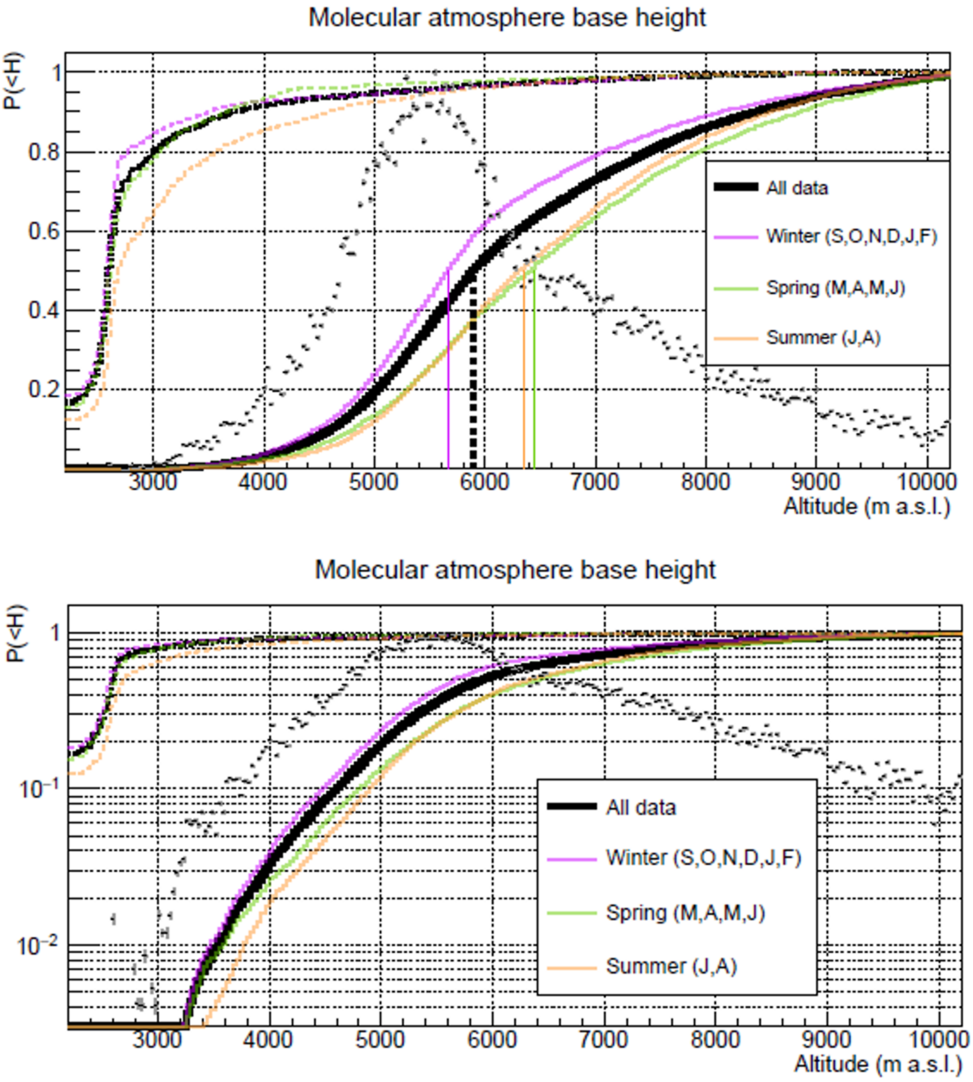

Figure 4.8: Cumulative probabilities for pure molecular atmosphere base heights (full lines) and the PBL heights using the gradient method [121] (dashed lines) during MAGIC data taking conditions (RH $< 90\%$, wind gust $< 40\,\mathrm{km/h}$) and weighted according to Eq. 4.16. Where the signal gradient coincides with the start range of full overlap of the LIDAR, a value of 2200 m has been artificially attributed to PBL height. The vertical lines refer to the medians of the molecular base height distributions. Gray dots show the differential probability of the full data set, scaled to reach a maximum of 1 for better comparability. Top: in linear scale, Bottom: in logarithmic scale [99].

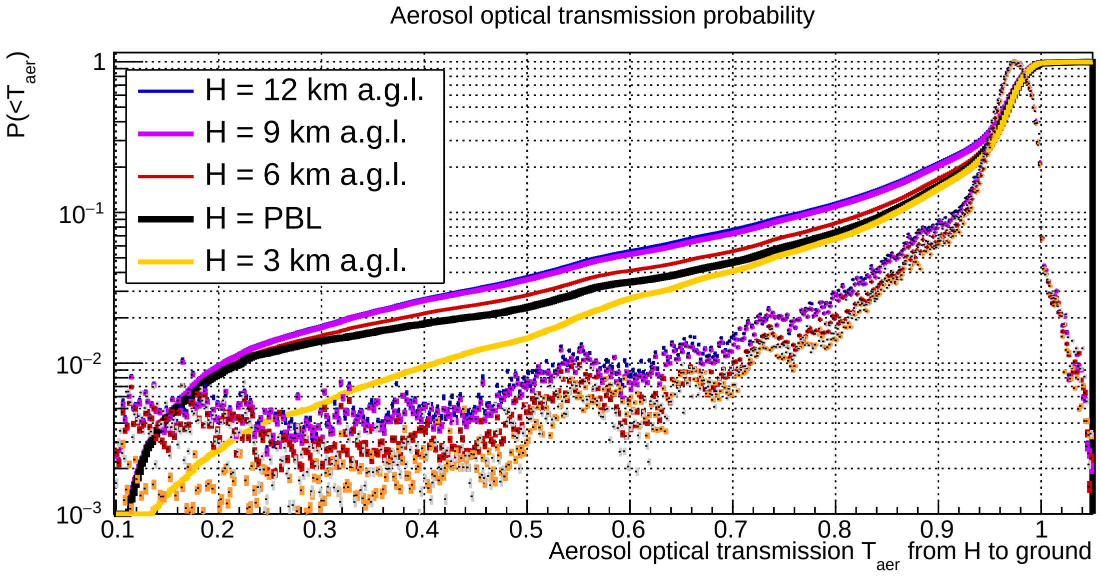

Figure 4.9: Cumulative probabilities for vertical aerosol transmission from different altitudes above ground, during MAGIC data taking conditions (RH $<$ 90 %, wind gust $<$ 40 km/h) and weighted according to Eq. 4.16. The dots show the differential probability of the full data set, scaled to reach a maximum of 1 for better comparability. Note that the blue curve (corresponding to 12 km above ground) is almost hidden behind the purple one (9 km above ground) [99].

frequently optically thin Cirrus clouds, or clouds made of ice crystals. Above the ORM, lower, optically thick clouds are typically of the Cumulonimbus and Altostratus types. Of the approximately 16,500 clouds in our seven-year data sample, 92 % are made up of a single cloud layer, and 8 % are made up of two layers divided by a pure molecular atmosphere portion. Although found, more than two layers are extremely uncommon (<0.4 %) and are all concentrated in December.

Nonetheless, this 7 year data sample is heavily biased towards nights without Cumulonimbus because these are the times when the MAGIC Telescopes and its auxiliary LIDAR system typically cease operations.

The part of the troposphere not affected by the ground layer, or the base height of the pure molecular atmosphere, is represented by Figure 4.10, which displays the cumulative vertical aerosol transmission probabilities from 12 km above ground. Then, about one-eighth of the collected data would require a cloud correction, a value consistent with the 84% relative number of photometric nights based on satellite observations [122]. Cloud occurrence probability peaks in the winter and troughs in the summer, with middle values in the spring. When rain or totally opaque clouds prevent MAGIC observations from being made, the MAGIC LIDAR is rendered inoperable. Because of this, the statistics displayed in Fig. 4.10 are only representative for standard astronomical observation conditions and are biased towards lower cloud occurrence probabilities. However, a comparison of this parameter between Periods 1 and 2 reveals excellent agreement, suggesting that the circumstances surrounding the cessation of MAGIC data collection have not changed over time.

The retrieved cloud profile is contaminated by clouds that are only partially illuminated by the laser and by tiny temperature fluctuations [59], which have not been included in the molecular particle model and could be mistaken for a cloud with very little optical depth. This occurs if the LIDAR moves away from the cloud during the course of its 100-second data collection cycle. Upon visual inspection of numerous LIDAR profile sequences, it has been observed that the emergence of a cloud in the field of view causes an artificial increase in LIDAR ratios. These ratios then remain steady at a physically feasible value,

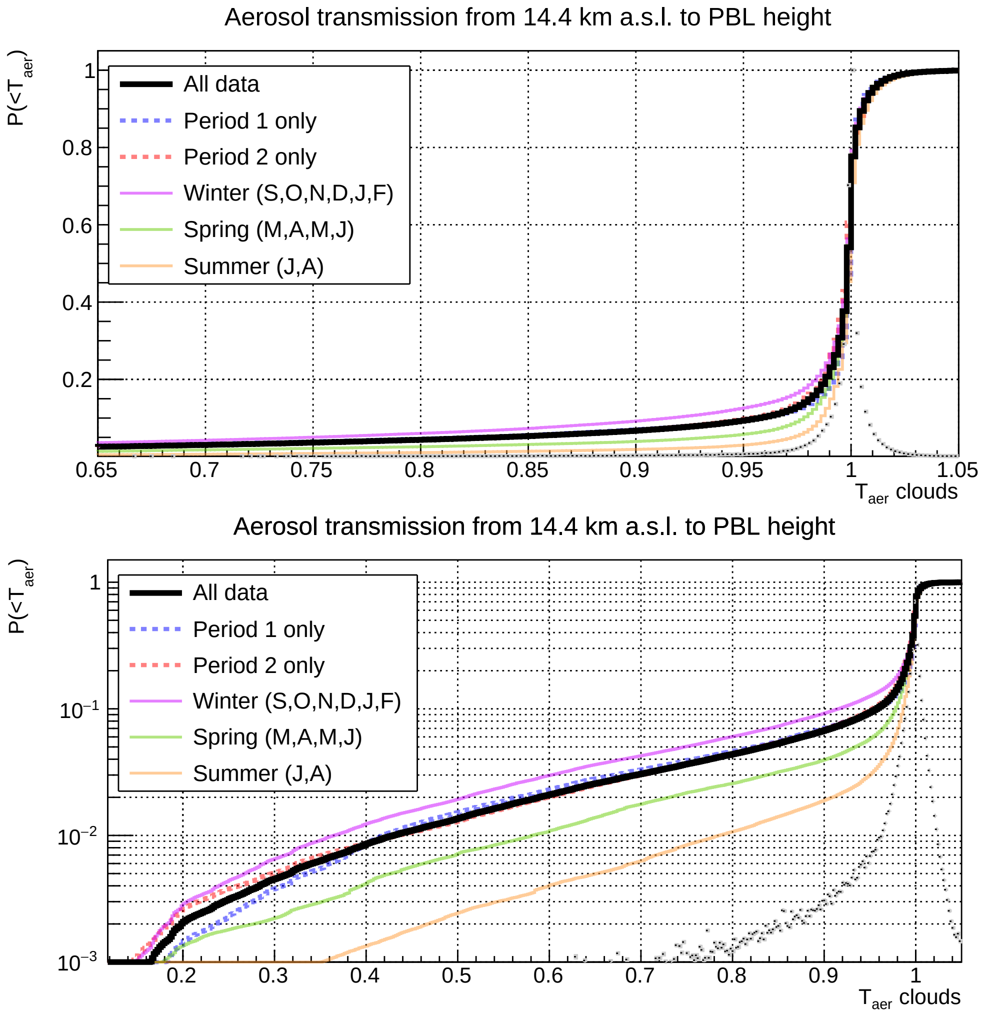

Figure 4.10: Lines: cumulative vertical aerosol transmission probability of green light for aerosols/clouds between 12 km above ground (14.4 km a.s.l.) and the molecular base height during MAGIC data taking conditions (RH $< 90\%$, wind gust $< 40\,\mathrm{km/h}$) and weighted according to Eq. 4.16. Gray dots show the differential probability of the full data set, scaled to reach a maximum of 1 for better comparability. Top: in linear scale, bottom: in logarithmic scale. Note the different horizontal axis ranges [99].

meaning a LIDAR ratio within the typical range expected for atmospheric aerosols and clouds, usually between about 20 and 80 sr^{-1} [59], before gradually increasing again as the cloud slowly vanishes. The LIDAR's field of view may only be partially covered by thin clouds with fine substructures. The reconstructed LIDAR ratios in each of these cases are artificially elevated. As a function of the reconstructed average cloud LIDAR ratio, Figure 4.11 displays mean cloud altitude and optical depth. It is evident that the reconstructed LIDAR ratio has no effect on cloud altitude; rather, an increase in LIDAR ratio causes an optical depth to decrease. Above a LIDAR ratio of roughly 40 sr, there is a transition from one behavior to the other, and vertical optical depths exceeding 0.1 are sporadically observed. Due to these factors, only the sections that follow the portions of the data sample that have a reconstructed LIDAR ratio of less than 40 sr will be described.

Lastly, LIDAR ratios below 7 sr are interpreted as temperature fluctuations and are typically associated with very low optical depths. Additionally, these data were eliminated from the sample.

The distribution of LIDAR ratios and vertical optical depths from the remaining cloud sample is displayed in Figure 4.12 (top). The vertical optical depths (VOD) exhibit a multimodal distribution with centers at 0.09 and 0.5, while the LIDAR ratios have a width of 6 sr and a center at 21 sr. These values are in line with expectations for C3 and C2 type Cirrus [123, 124], with a higher relative prevalence of C2-type Cirrus in the spring. Subvisible cirrus (SVC) [125] are part of the sample with VOD$<$0.01 and are detected primarily in the summer, but they are undoubtedly underrepresented here. Nevertheless, MAGIC LIDAR system is not particularly sensitive to SVC.

The graphs in Figure 4.13 display the altitudes of the cloud base and top. Clouds with base altitudes around 8 km a.s.l. and top altitudes around 10 km a.s.l. are seen in the summer data. These summer clouds have thinner geometric thicknesses than winter and spring clouds, which typically extend farther into the tropopause. Cloud top heights in the spring and winter are observed to reach altitudes of 8–14 km, which closely resembles the distribution of the lower part of the heights of multiple thermal tropopause events, such as double or triple tropopause occurrences characterized by distinct temperature inversions

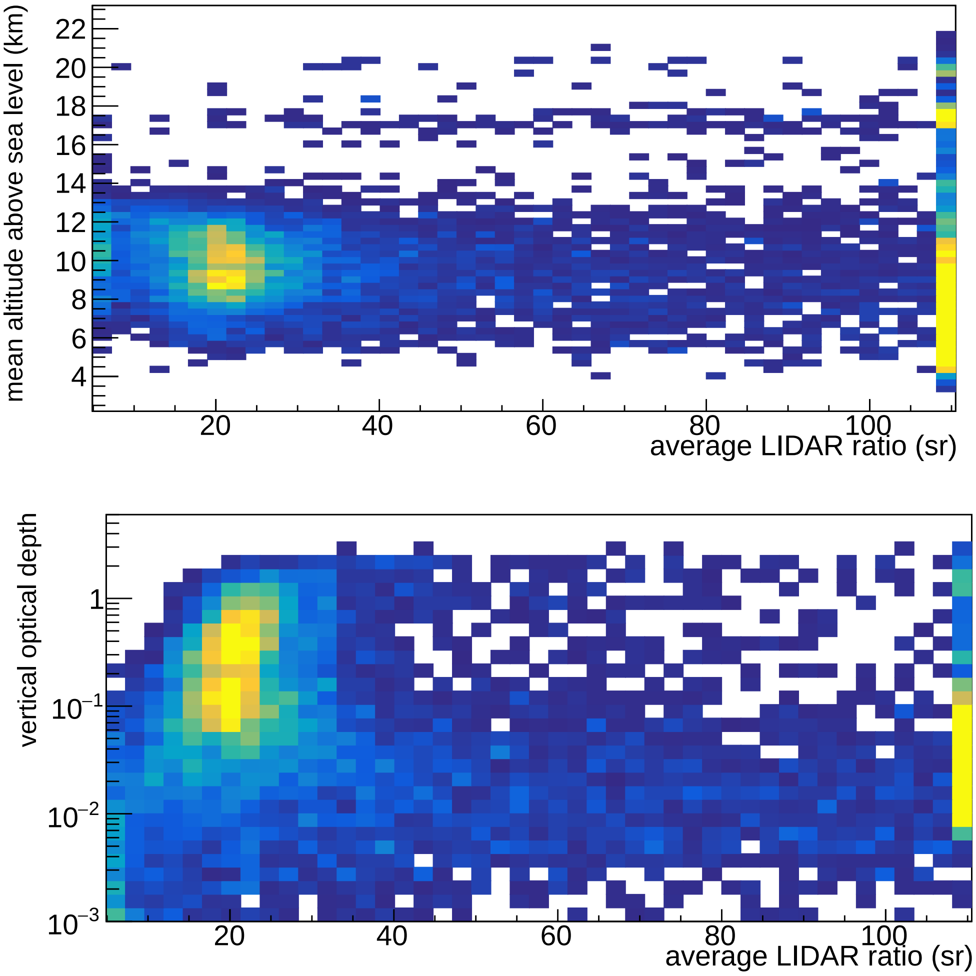

Figure 4.11: Distribution of cloud mean altitudes (top) and vertical optical depths (bottom) vs. reconstructed average LIDAR ratios. LIDAR ratios smaller than 5 sr have been collapsed into the first bin and larger than 110 sr into the last bin [99].

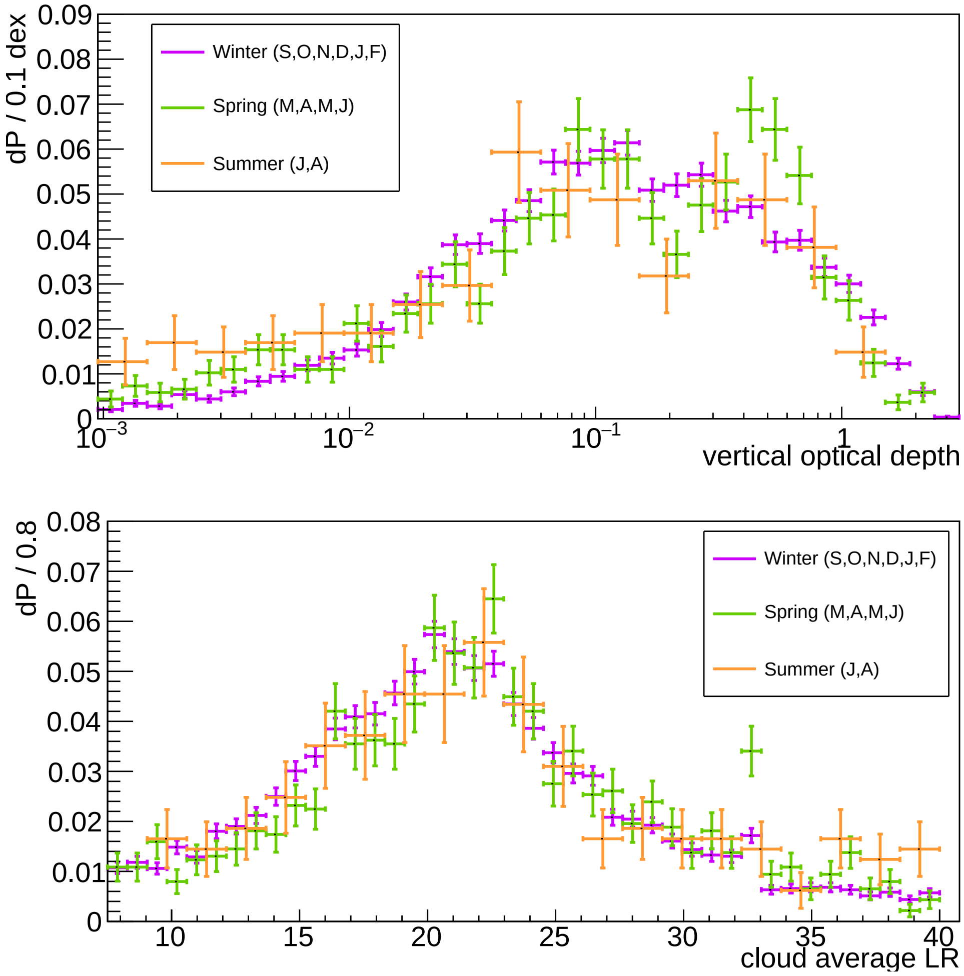

Figure 4.12: Distributions of vertical optical depths (top graph) and LIDAR ratios (bottom graph) for the sample with reconstructed LIDAR ratios larger than 7 sr and smaller than 40 sr [99].

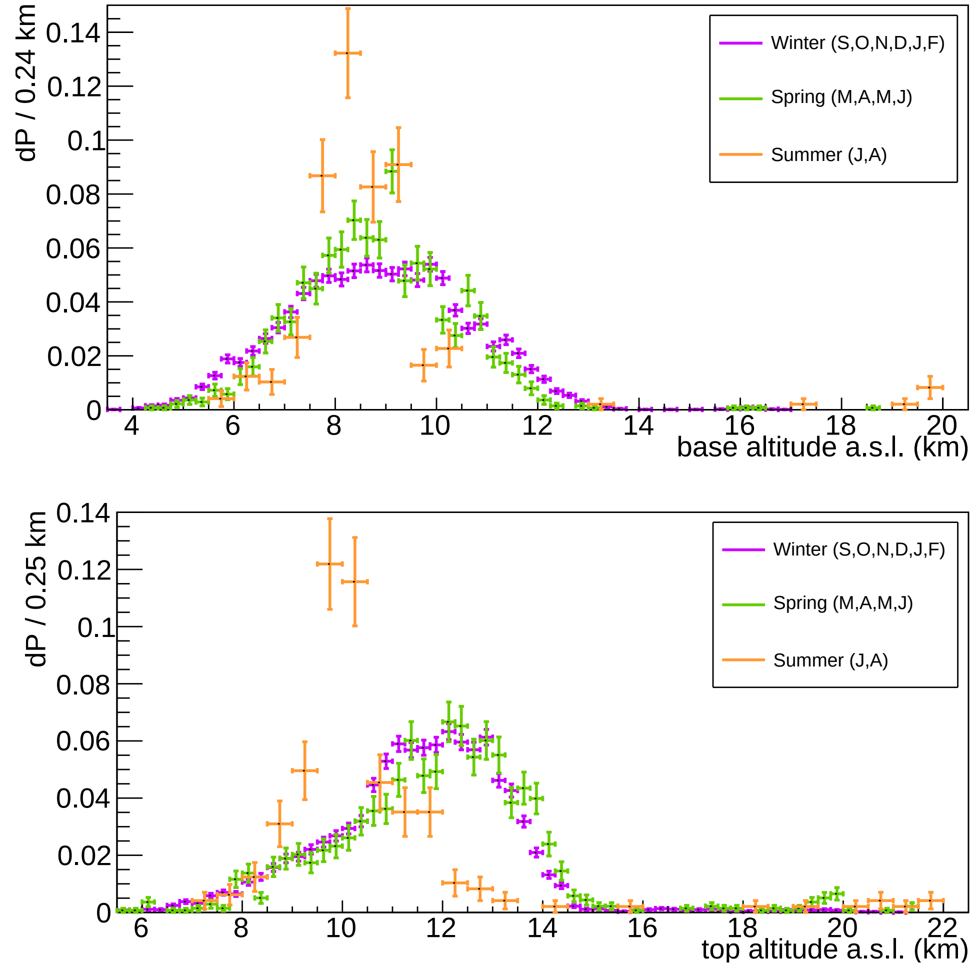

Figure 4.13: Distributions of cloud base altitudes (top panel) and cloud top altitudes (bottom panel) for the sample with reconstructed LIDAR ratios larger than 7 sr and smaller than 40 sr [99].

at different atmospheric layers [126].

Occasionally, in all seasons, exceptionally high clouds exceeding 14 km base height are observed, and these clouds are consistent with the thermal tropopause height distribution for individual tropopause events [126]. Single tropopause events occur at a frequency of around 20% in winter, rising to almost 100% in summer [126]. In spring and autumn, the frequency of occurrences is intermediate. This distribution of cloud top height does not reproduce such a large prevalence. Conversely, summer clouds typically occur at lower altitudes of 8–12 km, even though there is only one tropopause located well above 14 km. However, they can occasionally reach extremely high altitudes of up to 20 km a.s.l.

Figure 4.14 displays the reconstructed mean altitudes of clouds against the vertical optical depth for the entire cloud sample (i.e., including those reconstructed with unphysical LIDAR ratios), and divided into three seasons, makes the impact of a very high single tropopause more apparent. Here, in summertime clouds move up to the single thermal tropopause above 14 km asl, while winter and springtime clouds are typically trapped by the lower portion of a double or triple tropopause temperature inversion.

The seasonal cycle of the fundamental cloud parameters, including base and top heights and geometric thickness, is depicted in Figure 4.15. Additionally, the standard deviation of the vertical cloud extinction profile is displayed. As can be seen, the months of June, July, and August are when lower and thinner clouds are most common, while August and September are the months in which the highest clouds are concentrated. In winter and spring, geometric thicknesses range from two to three kilometers on average, while in June, July, and August, they are smaller (median thicknesses between one and 1.5 kilometers). During these three summer months, the spread between the vertical cloud extinction profile's geometric thickness and standard deviation also narrows, suggesting a more uniform distribution of extinction along the vertical profile. On the contrary, clouds in the winter and spring may exhibit a higher concentration of extinction within the cloud.

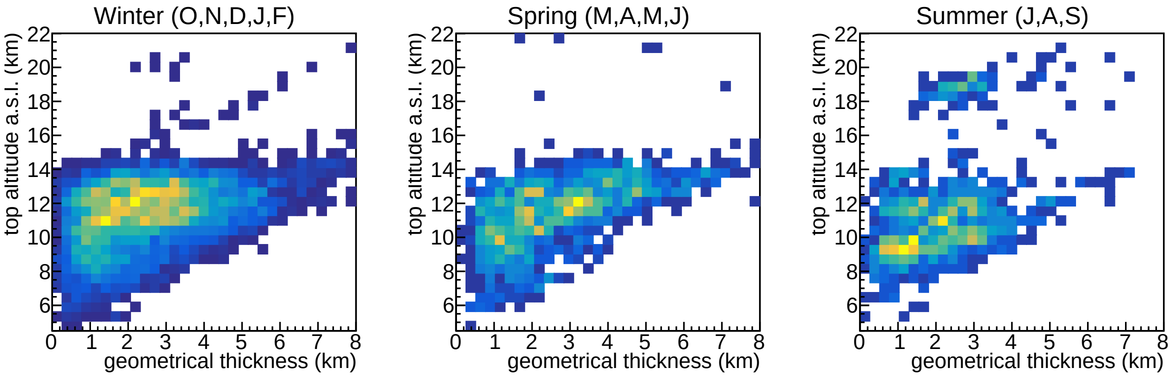

Figure 4.14: Distribution of reconstructed cloud top altitudes vs. geometric thickness. The figures have been separated into Winter (left, comprising October, November, December, January, February), Spring (March, April, May, June), and Summer (July, August, September). Note that in this case and unlike previously, September has been included in the summer data sample, because of its clear preference for high cloud top altitudes (see also Fig. 4.15, left) [99].

This is especially noticeable for the months of September, October, November, December, and January, when geometrical thicknesses ranging from several hundred meters to one kilometer are accompanied by very small standard deviations of the vertical cloud extinction profile, potentially less than several tens of meters.

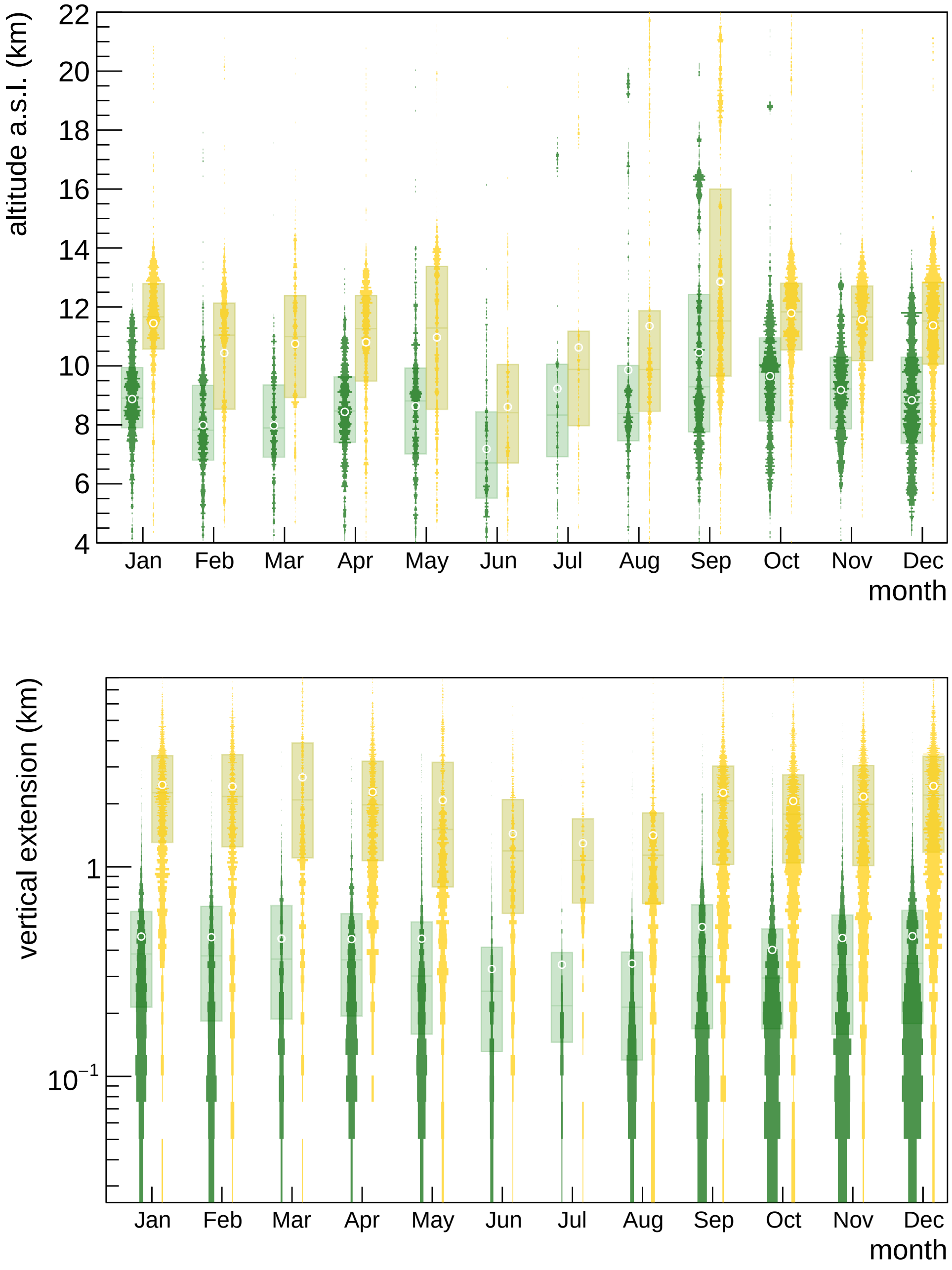

Figure 4.15: Top: seasonal cycle of cloud base heights (green) and top heights (yellow), bottom: seasonal cycle of standard deviations of clouds extinction-weighted vertical profile (green), and geometric thickness (cloud top minus cloud base height, yellow). The overlaid bars show the 25% to 75% percentiles of the distributions. Note the logarithmic scale of the bottom graph [99].

4.3.4 Night-Sky Brightness

Any LIDAR can measure the corresponding contribution from the night-sky brightness and subtract it from its laser return signals. When using the MAGIC LIDAR, the median photo-electron rate from the area prior to the laser return signal becoming visible is used to measure background light. Since MAGIC LIDAR uses an HPD with high quantum efficiency and charge resolution, it is ideal for measuring photo-electron rates falling through a well-defined diaphragm from a known solid angle. This function is independent of the LIDAR's laser shooting. The obtained photo-electron background rate depends on the light of the night sky (LoNS), which is affected by potential anthropogenic contributions, star fields, zodiacal light, and the presence of the moon. The mirror reflectance and HPD photon detection efficiency affect the measured rate. Additionally, the observed background has changed over time due to changes in the size of the diaphragm in front of the receiver optics. The instrumental contributions must be adjusted for ageing and hardware changes before using the background rates for a characterization of the night sky background conditions at the site. This was accomplished by using the degradation proxy for each of the two laser periods independently.

Here, the implicit assumption that the laser power has been constant over time for both periods was made. It is verified that, following correction, the median NSB remained constant using the degradation proxy, supporting the earlier hypothesis. The impact of each contribution is displayed in the following after all data collected during twilight have been eliminated, leaving only data collected during astronomical darkness (solar zenith angle $\theta_\odot > 108^\circ$). Furthermore, galactic observation fields that require galactic latitudes $l > 10^\circ$ have been excluded (see Appendix A).

The median background rates with the presence of the Moon are depicted in Figure 4.16 (top). Background rates can rise by up to a factor of 20 as the LIDAR points are taken closer to the Moon and as the Moon's phase gets brighter. Although even greater increases have been observed in some cases, these data points are considered unreliable due to inaccuracies in the LIDAR measurements near the Moon. The influence of clouds on the background photo-electron rates is further highlighted in Figure 4.16 (bottom). The background rates rise with the amount of clouds covering the LIDAR field of view; more background light is produced by optically thicker clouds. The back-reflection of moonlight from the clouds explains this behavior.

The effect of zodiacal light [127, 128] is visible on the background rates after the data contaminated by the Moon is removed. The median background rates in ecliptic coordinates are displayed in Figure 4.17 (left). Background light is observed to increase by up to 150%, mainly for the evening zodiacal light. In the following representation, the data with ecliptic latitudes smaller than 30° and longitude differences with respect to the Sun smaller than 90° are removed. The median background rates in galactic coordinates are displayed on the right side of Fig. 4.17. The galactic plane appears noticeably brighter, especially the Galactic Center, where there is an apparent 100% increase in background light relative to the extra-galactic fields. The remaining sample is left with airglow [128], diffuse star light, anthropogenic contributions such as light pollution, and spurious bright stars in the field of view (see Appendix A).

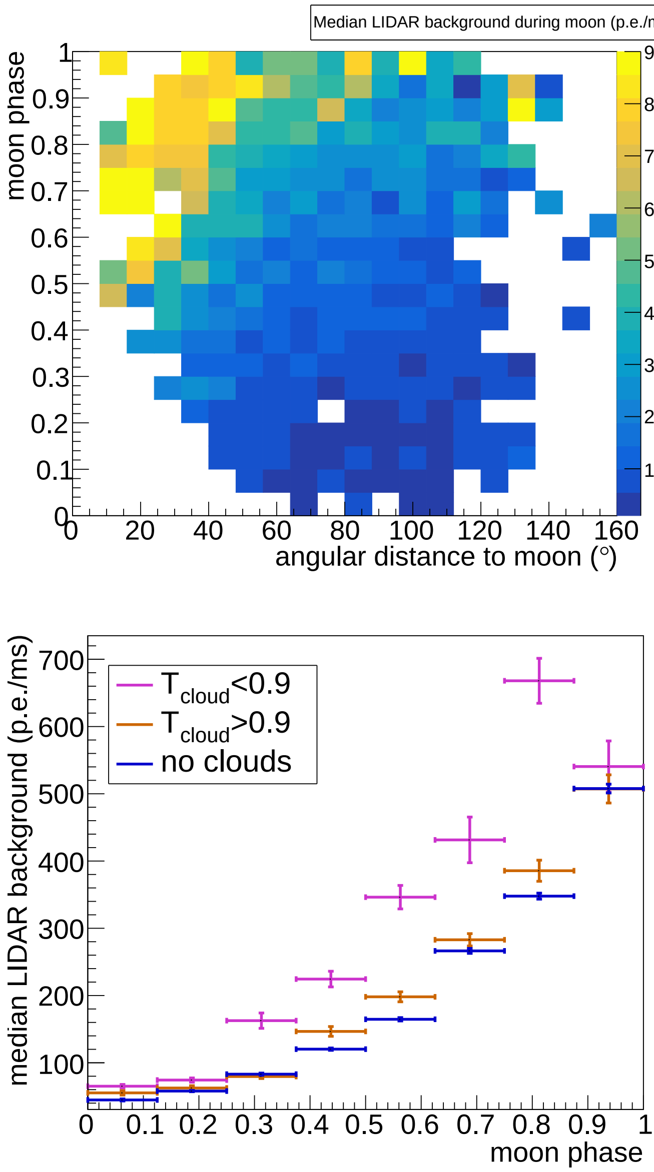

Figure 4.16: Top: Median LIDAR background rates observed as a function of angular distance to the Moon and the moon phase for cloudless nights. Bottom: median background rates as a function of moon phase, for data with cloud base higher than 2 km and cloud top lower than 12 km above ground. The cloud data has been divided into those with cloud transmissions higher and lower than 0.9. For comparison, also the cloudless data are shown. Only angular distances between 40° and 110° from the moon have been used here, in order to ensure a similar coverage of all angular distance and moon phase bins. Galactic star fields and those affected by zodiacal light had been excluded previously [99].

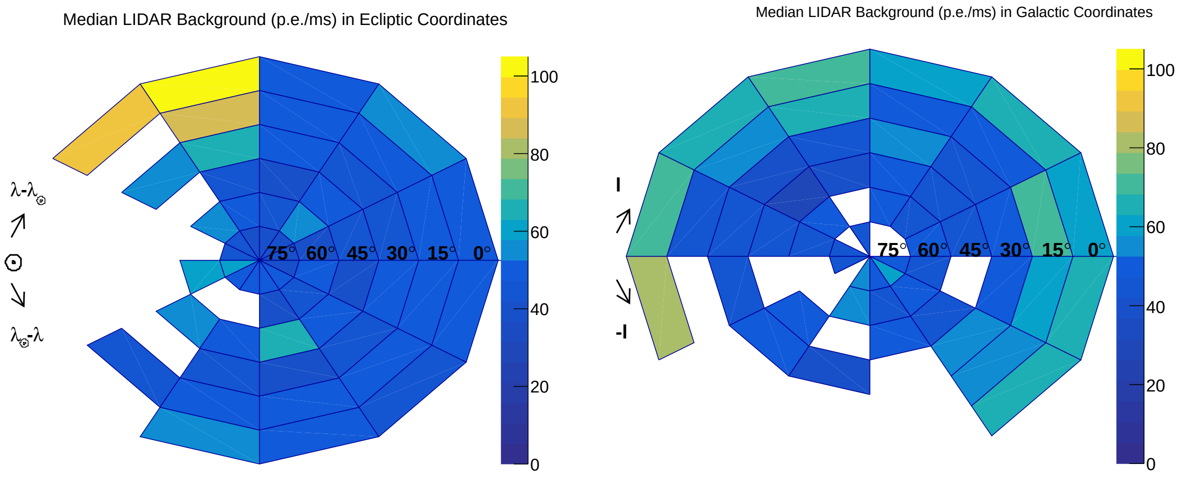

Figure 4.17: Observed median LIDAR background rates in ecliptic (left) and galactic (right) coordinates. The Sun (Galactic Center) is located at the left, the ecliptic (galactic plane) is represented by the outer circle, whereas the ecliptic (galactic) pole is found in the center. The numbers show absolute ecliptic (galactic) latitudes. Moon and twilight data have been excluded previously, as well as data taken before 23 h UTC time. In the left plot, galactic fields have also been excluded, whereas in the right plot zodiacal light has been removed. Empty fields denote lack of data [99].

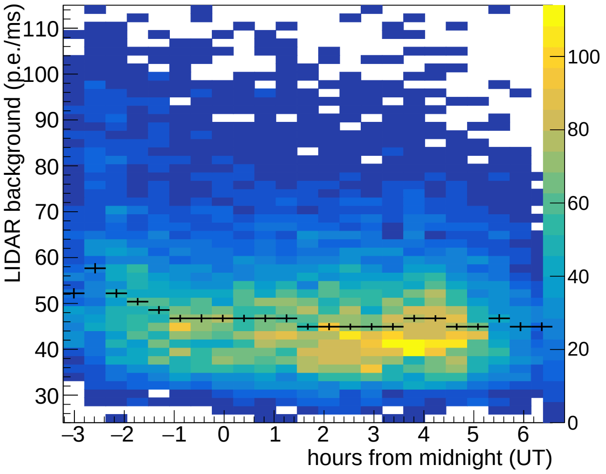

Figure 4.18: Observed LIDAR background rates as a function of local time. Moon, twilight, zodiacal light and galactic fields have been excluded previously [99].

The latter are primarily originated from La Palma's two largest towns, Los Llanos, which is situated south-south-west, and Santa Cruz, which is situated southeast of the ORM. Additionally, the airport and its environs contribute to artificial light backgrounds on the southeast of ORM. The northern coast of the 130 km distant, but considerably more densely populated, island of Tenerife, is also located in that direction. La Palma's street lighting is governed by law (BOE-A-1992-8705 1988, 2017) [129, 130], and the IAC's Sky Protection Unit (Instituto de Astrofísica de Canarias, Oclinica Técnica Proteccion del Cielo (OTPR) 1988) [131] provides guidance for any kind of light installation. Thanks to these actions, light pollution on the Canarian observatories has significantly decreased, particularly since 2017 with the implementation of updated lighting regulations, and is now at levels typical for observatories of the highest world standard.

Nonetheless, when the LIDAR photo-electron rates are plotted against local time, the impact of lingering anthropogenic lights becomes apparent (see Figure 4.18). After 23:00 UT (24:00 local time), when the street lights go out, there is a noticeable decrease in light pollution because only sodium lamps, which are invisible at 532 nm wavelength, remain switched on.

The arrival directions of the residual light backgrounds are shown in Figure 4.19, divided into two samples: before and after 23 UT. As expected by airglow, light pollution increases toward the horizon [128]. However, a noticeable increase in residual background is observed in some azimuthal directions, reaching up to 50% before midnight and 25% after. Before midnight, light pollution is detected from Los Llanos, Santa Cruz/Tenerife, and the west-north-west, where the small town of Puntagorda is located. The remaining light from the observatory house, situated northwest of the MAGIC LIDAR, could also contribute. After midnight, large zenith angle observations show a 5–10% increase in LIDAR background rates toward Los Llanos and Santa Cruz/Tenerife.

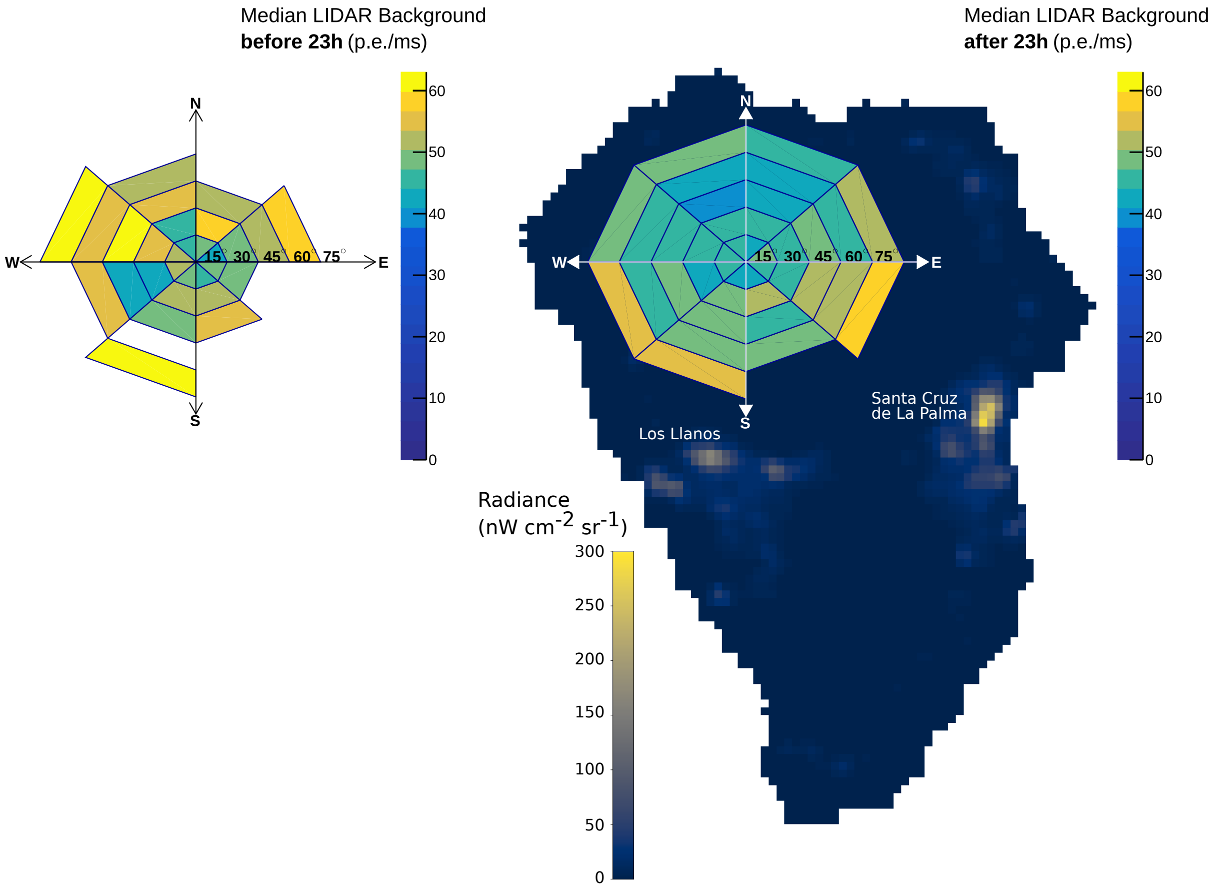

Figure 4.19: Observed median LIDAR background rates in local coordinates. Left: only data before 23h UT, right: after 23h UT. Moon, twilight, zodiacal light and galactic fields have been excluded previously. Empty fields contain no data. In addition, the averaged and bidirectional reflectance distribution function (BRDF) adjusted for temporal radiance during snow-free periods in 2020 is shown [132]. These satellite observations were performed using the panchromatic (500 nm – 900 nm) Day-Night-Band (DNB) of the Visible Infrared Imaging Radiometer Suite (VIIRS) onboard the Suomi-National Polar-orbiting Partnership (Suomi-NPP). All Suomi-NPP data were gathered after 23h UT as a consequence of its Sun-synchronous orbit [99].

Chapter 5

IACTs Performance in Conditions of Reduced Atmospheric Transmission

The next-generation ground-based observatory for gamma-ray astronomy at very-high energies, known as the *Cherenkov Telescope Array Observatory* (CTAO), will be composed of two arrays: the Southern CTAO, located in Paranal, Chile, and the Northern CTAO, located in La Palma, Spain, in the vicinity of already existing fully operative MAGIC telescopes. By combining three different types of Imaging Air Cherenkov Telescopes (IACTs) - Large-, Medium-, and Small-Sized Telescopes - the CTAO will cover a wide energy range from 20 GeV to 300 TeV.

In IACTs, the energy of broad air showers caused by primary gamma-rays is measured using the atmosphere as a calorimeter. The refractive index of air determines the Cherenkov emission conditions and thus affects the amount of Cherenkov light produced in the shower. The atmospheric profile has a significant influence on the Cherenkov light yield at small core distances. Here, the core distance refers to the lateral distance between the air-shower axis (shower core) and the telescope on the ground. Seasonal variations in the light yield have been observed at mid-latitude sites [133], ranging from 15% to 20%; however, recent research indicates that the effect is significantly smaller at the CTAO sites [134].

Aerosols and molecules can both absorb and scatter Cherenkov light (a processes known as Rayleigh or Mie scattering, see Section 3.4) [135, 133]. The Cherenkov camera records fewer Cherenkov photons when clouds are present, which could lead to a bias towards lower energies, decreased sensitivity, and erroneously reconstructed spectra. The influence of cloud altitude and transmission on the CTAO-North performance in terms of differential sensitivity, effective area, angular resolution, and energy resolution is presented in this study, which is based on Monte Carlo (MC) simulations.

5.1 Monte Carlo Simulations and Analysis Chain

Simulations of extensive air showers initiated by primary gamma-rays, electrons, and protons were generated with CORSIKA version 7.6400 [136] and the hadronic interaction model QGSJET-II [137].

The emission of Cherenkov light in the wavelength range from 240 nm to 700 nm was simulated using the IACT/ATMO extension. Simulations for primary directions of 20 degrees in Zenith and 180 degrees in Azimuth (pointing southward) have been carried out. Using atmospheric models produced with the MODerate resolution atmospheric TRANsmission (MODTRAN) code version 5.2.2, the effects of cloud altitude and optical depth on the CTAO-North performance have been simulated while `sim_telarray` software has been utilized to replicate different responses of the telescopes. The radiative transfer equation was solved to determine the atmospheric transmission in the wavelength range from 200 nm to 1000 nm in the presence of 1 km thick altostratus clouds.

The analysis of the data was performed by using the MAGIC Analysis and Reconstruction Software (MARS) [141]. The analysis is performed in the following steps:

1. **Signal extraction and calibration** - the signal extraction is performed using the sliding window algorithm [142] in the first pass, and the fixed window extractor in the second pass.

2. **Image cleaning and parametrization** - the two-level absolute image cleaning algorithm is used for image cleaning to suppress signals in the camera induced by the

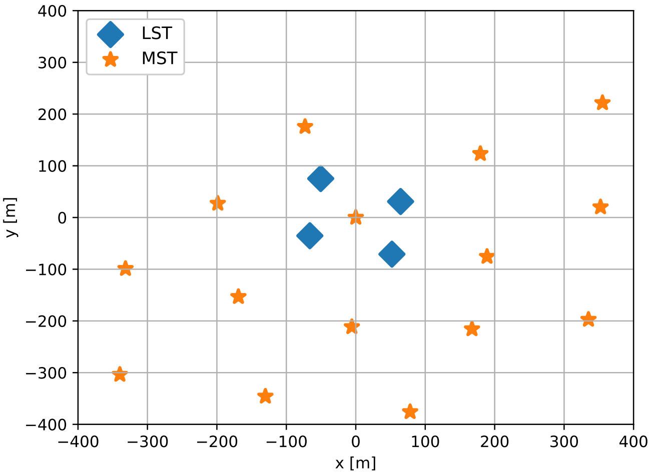

Figure 5.1: Simulated configuration for the CTAO-North array. The observatory level is at 2147 m a.s.l., while the North is oriented towards the top of the page [138]. Current configuration includes 4 LSTs and 9 MSTs [139, 140].

night sky background and electronic noise; the cleaned image is parameterized with the so-called Hillas parameters [143, 144].

3. **Reconstruction of direction and energy** - the arrival direction is calculated as the point in the camera that minimizes the weighted sum of squared distances between the source and the shower axis (the weights are found using the look-up tables filled with the square of mean *miss* in bins of *size* and *width* over *lenght*. The energy reconstruction and gamma-hadron separation are performed using the random forest algorithm [145].

4. **Performance estimation** - performed by optimizing gamma-ray selection cuts using simulated data sets that model both gamma-ray and background events. These optimized cuts are then applied to the simulated reconstructed events to obtain the instrument response functions (IRFs), including effective area, differential sensitivity, angular resolution, and energy resolution. This approach enables accurate telescope performance estimates before data acquisition.

Hillas Parameters in IACT Analysis

The Hillas parametrization is a classical method for characterizing the shape of Cherenkov images in IACTs [144]. It reduces the complex light distribution in the camera into a set of geometric and statistical parameters, enabling efficient gamma/hadron discrimination and reconstruction of arrival direction and energy.

Before computing these parameters, the camera image is cleaned to remove noise from the night-sky background, typically using tail-cut algorithms. The remaining pixels, assumed to contain real shower signal, are used for parameter extraction.

The most commonly used Hillas parameters, which describe the image intensity, orientation, and spatial extent in the camera plane, are listed below:

- **Size:** The total signal content in the image, measured in photoelectrons (p.e.). It is proportional to the energy of the primary particle.

- **Centroid:** The center of gravity (barycenter) of the image, computed as the amplitude-weighted mean of pixel positions.

- **Length and Width:** Respectively, the RMS extent of the image along the major and minor axes of the fitted ellipse (in mm). They describe the longitudinal and lateral spread of the shower in the camera plane.

- **Miss:** The angular distance (in degrees) between the image axis and the center of the camera (optical axis). A small *miss* is expected for well-reconstructed gamma-ray showers.

- **Distance:** The Euclidean distance between the image centroid and the camera center. This is useful for direction reconstruction.

- **Alpha (α):** The angle between the major axis of the image and the line connecting the centroid to the assumed source position. Gamma-ray images from a point source tend to have small alpha.

Note that the definitions and interpretations of parameters such as miss, distance, and alpha assume that the target source is located at or near the center of the camera, as is typically the case for pointed IACT observations.

A schematic illustration of the Hillas parameters, which are used to describe the shape and orientation of a Cherenkov shower image as recorded by a single IACT, is shown in Figure 5.2. These parameters characterize the image in the camera plane of one telescope and serve as the basis for further stereoscopic reconstruction when multiple telescopes observe the same shower.

In stereoscopic observations, Hillas ellipses from multiple telescopes can be geometrically intersected to reconstruct the incoming direction and core impact point of the shower. Although more advanced reconstruction methods exist today, such as deep-learning approaches based on convolutional neural networks (CNNs) applied to Cherenkov images, Hillas parameters remain a robust and computationally efficient approach widely used in IACT data pipelines.

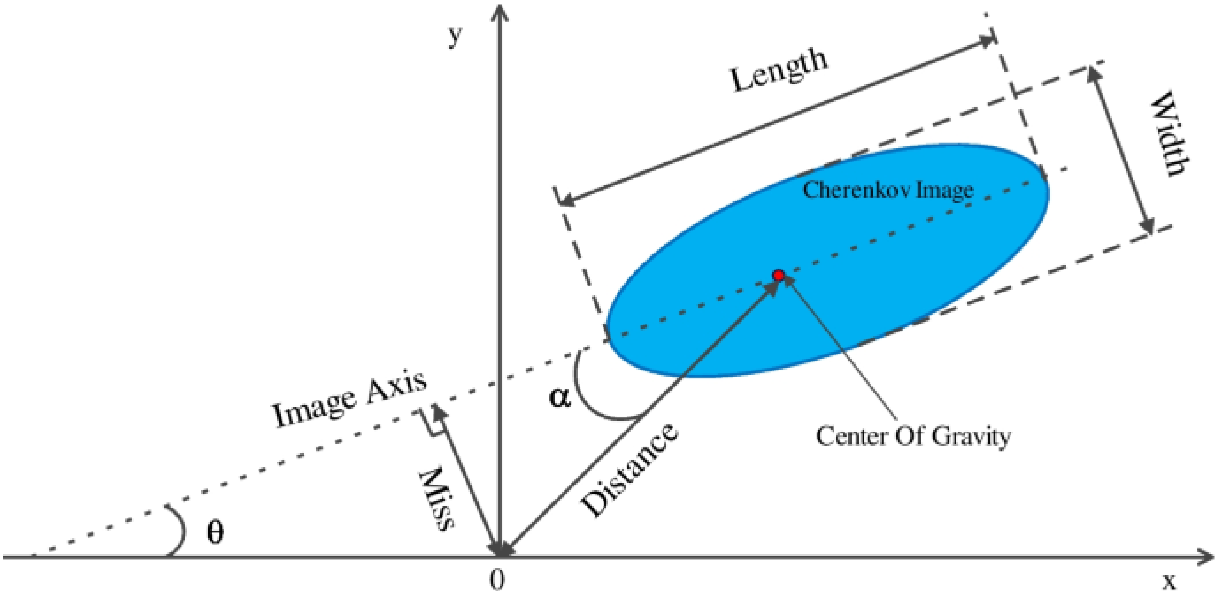

Figure 5.2: Schematic illustration of Hillas parameters used to describe the shape and orientation of a Cherenkov shower image. Concept originally introduced by [144]. Image taken from [146].

5.2 Results of the Performed CTAO-North Analysis

5.2.1 Angular Resolution

The angular difference between the reconstructed and actual source directions is represented by θ (as seen in Figure 5.2). The angular resolution, which is derived from the θ distribution, is used to evaluate direction reconstruction. The value that contains 68% of all reconstructed gamma-like events in a specific energy bin is used to represent the angular resolution. Depending on the characteristics of the clouds, the angular resolution ranges from 0.18 deg to 0.22 deg at the energy of $\approx$ 40 GeV to 0.06 deg at the energy of 1 TeV, plateauing at $\approx$ 0.05 deg above 1 TeV (Figure 5.3 top). The direction reconstruction is generally more severely affected by clouds with lower transmissions, which can result in an angular resolution reduction of up to 15% (Figure 5.3 bottom). Clouds have very small or even negligible impact on direction reconstruction at the highest energies.

5.2.2 Effective Area

The reduced sensitivity is primarily due to a decrease in the effective area, which occurs because the camera detects fewer Cherenkov photons under certain atmospheric conditions. The effective area is defined as the geometrical area around the telescope where a gamma-ray shower produces a trigger, folded with the gamma-ray efficiency of all cuts applied in the analysis. Figure 5.4 shows its reduction in relation to the effective area for the atmosphere without clouds. Effective area is drastically decreased below $\approx$ 250 GeV, reaching a maximum of 60% at transmission $T = 0.50$. Effective area stabilizes at roughly 20% above a few hundreds of GeV when clouds with $T = 0.50$ are present, and at roughly 10% when clouds with $T = 0.75$ are present.

5.2.3 Differential Sensitivity

The differential sensitivity, defined here as the lowest flux that can be identified with a statistical significance of five standard deviations for 50 hours of observations, is computed with the requirements of a minimum of 10 signal counts per energy bin and that the number of signal counts exceeds 5% of the residual background counts. The calculation is performed in five non-overlapping logarithmic energy bins per decade. Differential sensitivity of CTAO-North as a function of energy is presented on the graph at the top of Figure 5.5, while its ratio to the clear atmosphere is presented on the graph at the bottom of Figure 5.5. Differential sensitivity is drastically reduced in the presence of clouds. The most visible effect of clouds is at energies $\leq$ 150 GeV. At energies $\geq$ 1 TeV the stability in reduction is achieved, approaching $\approx$ 25% in the presence of clouds with $T = 0.50$, and $\approx$ 10% in the case of $T = 0.75$. Higher clouds have a smaller effect as only a faction of the Cherenkov light emitted by the shower is affected by the clouds. However, as more energetic showers penetrate deeper into the atmosphere, the fraction is dependent on the energy of the primary gamma-ray.

5.2.4 Energy Resolution

The energy resolution describes how accurately the instrument can determine the real energy of gamma primary, E_{true}. It is calculated bin-wise as a half width of the interval which contains 68% of the distribution in a respective bin, symmetric around $E_{\text{rec}}/E_{\text{true}} = 1$, where E_{rec} is reconstructed, or estimated, energy. Energy resolution varies between 0.18 and 0.24 in the lowest energy bin to $\approx$ 0.10 at the energy of 15 TeV (at the top of Figure 5.6). It is significantly degraded at energies below 250 GeV, by 30% for $T = 0.50$ and by less then 10% for $T = 0.75$ (at the bottom of Figure 5.6).

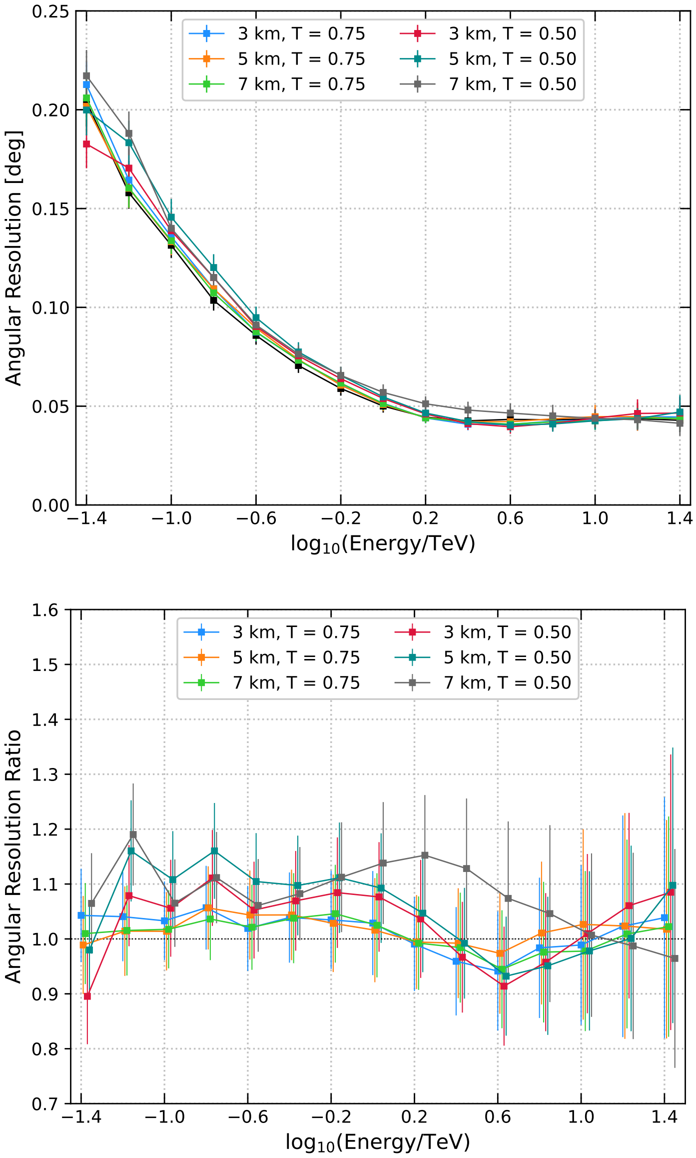

Figure 5.3: Top: angular resolution of CTAO-North for 50 hours of observations as a function of energy. Bottom: angular resolution ratio of CTAO-North for 50 hours of observations as a function of energy with respect to the clear atmosphere. The lower ratio value corresponds to a better resolution. Black dots represent a clear atmosphere case. Note: the points are slightly shifted to the right to achieve better visibility of error bars [138].

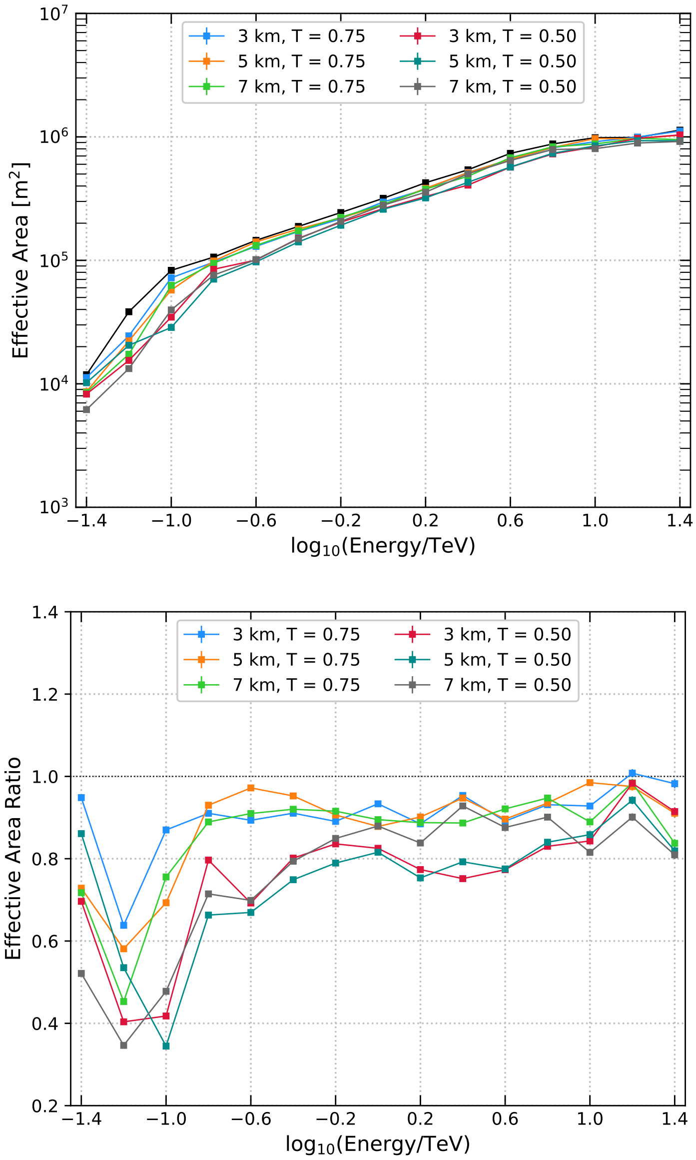

Figure 5.4: Top: effective area of CTAO-North for 50 hours of observations as a function of energy. Bottom: effective area ratio of CTAO-North for 50 hours of observations as a function of energy with respect to the clear atmosphere. Black dots represent a clear atmosphere case. Lower values correspond to lower effective areas [138].

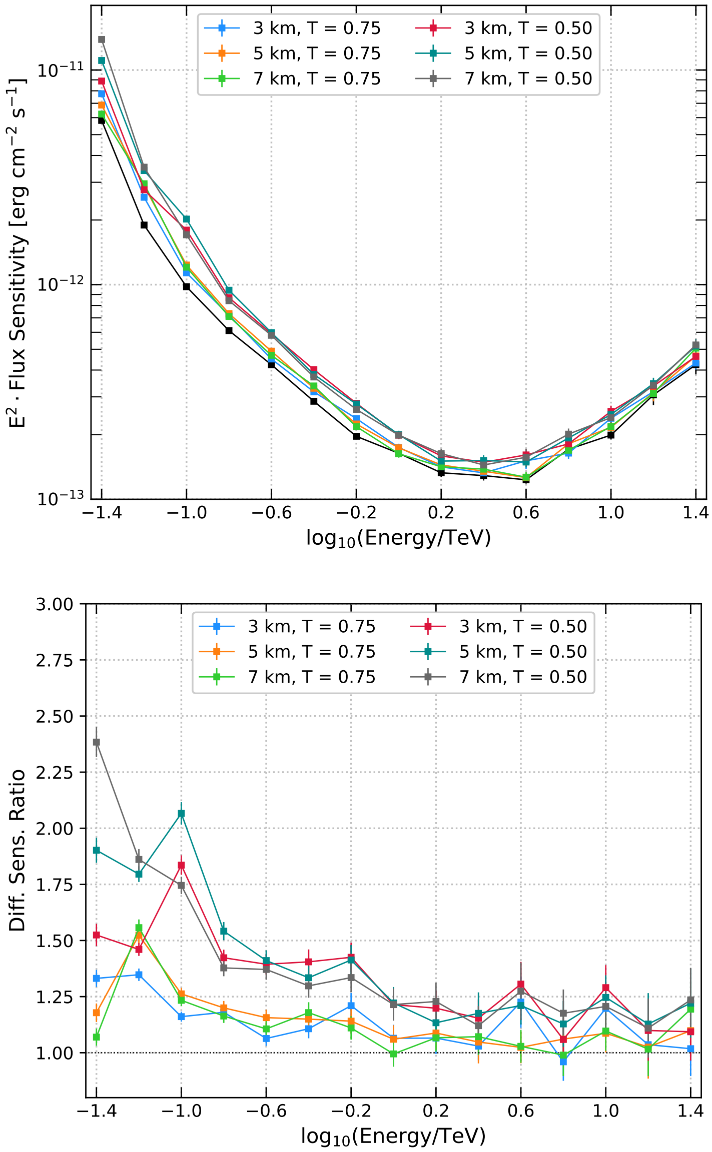

Figure 5.5: Top: differential sensitivity of CTAO-North for 50 hours of observations as a function of energy. Bottom: differential sensitivity ratio of CTAO-North for 50 hours of observations as a function of energy with respect to the clear atmosphere. Black dots represent a clear atmosphere case. Lower values correspond to better sensitivities [138].

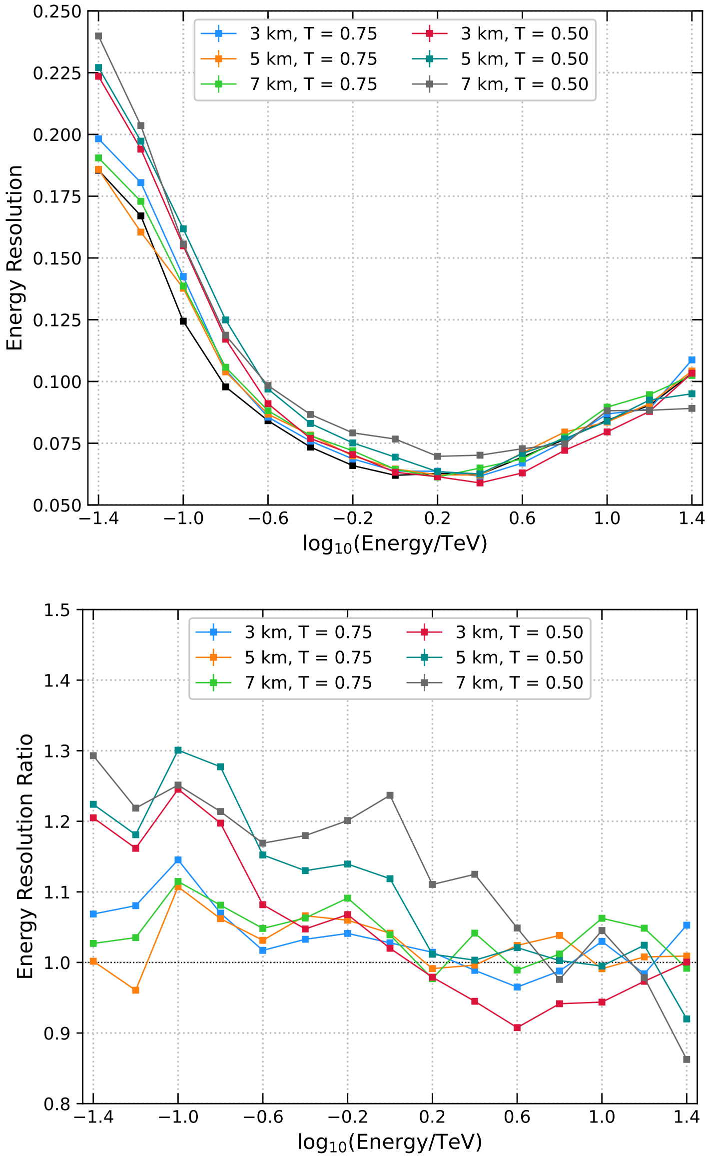

Figure 5.6: Top: Energy resolution of CTAO-North for 50 hours of observations as a function of energy. Bottom: Energy resolution ratio of CTAO-North for 50 hours of observations as a function of energy with respect to the clear atmosphere. Black dots represent a clear atmosphere case. Lower values correspond to better resolution [138].

5.3 Bura Supercomputer

Figure 5.7: The supercomputer Bura, located on the premises of the University of Rijeka.

For the CTAO-North simulations and analysis, the supercomputer Bura from the University of Rijeka, depicted in Figure 5.7, was used. The system offers a total processing capacity exceeding several hundred teraflops, supported by a large memory pool and high-speed storage solutions, enabling efficient handling of large-scale Monte Carlo simulations and data analysis workflows. Further technical specifications and information about the system's architecture, processing power, memory capacity, and available software tools can be found on the University of Rijeka's website [147].

Chapter 6

TeV Detection and Multi-wavelength View of the Flaring Blazar B2 1811+31

The blazar B2 1811+31, located at R.A. 18h13m35.2028s, Dec. +31d44m17.621s (J2000) [148], is classified as a BL Lac object in the *Fermi*-LAT Fourth Source Catalog (4FGL) [149] and as an IBL (Intermediate BL Lac object) [150]. The blazar was also identified as one of the most promising VHE γ-ray candidates based on multi-wavelength luminosity correlations predicting a VHE flux above the sensitivity threshold of current-generation IACTs within less than 25 hours of observation [151]. The redshift of the source was determined to be $z = 0.117$ based on optical spectroscopic observations [152].

Following the detection of a high state by *Fermi*-LAT from the source in the $E > 100$ MeV energy range on October 1, 2020 (MJD 59123) [153], a multi-wavelength (MWL) observational campaign on B2 1811+31 was organized. Observations conducted during this high-state period with the MAGIC telescopes led to the first detection of VHE γ-ray emission from the source [154]. *The Neil Gehrels Swift Observatory telescopes*, sensitive to the optical-to-X-ray range, joined the follow-up campaign, along with several optical and radio ground-based telescopes. These observations allowed for a detailed characterization of the source's high state across the entire electromagnetic spectrum, from radio to VHE γ-rays.

6.1 Instruments and Multiwavelength Analysis of the Blazar B2 1811+31

This section presents the MWL datasets and analyses performed in each energy band for B2 1811+31. Table 6.1 provides a list of the instruments whose data from the 2020 γ-ray high state were included in the analysis, along with the time ranges of the observations. Long-term data from the same instruments were also collected. In addition, long-term optical data from KAIT, KVA, and CRTS were incorporated. Further details on each dataset are provided in the following sections. The long-term MWL light curve of B2 1811+31, covering the period from 2005 to 2023, is shown in Figure 6.1, while the MWL light curve for an 80-day period surrounding the MAGIC observations during the 2020 γ-ray high state is shown in Figure 6.2.

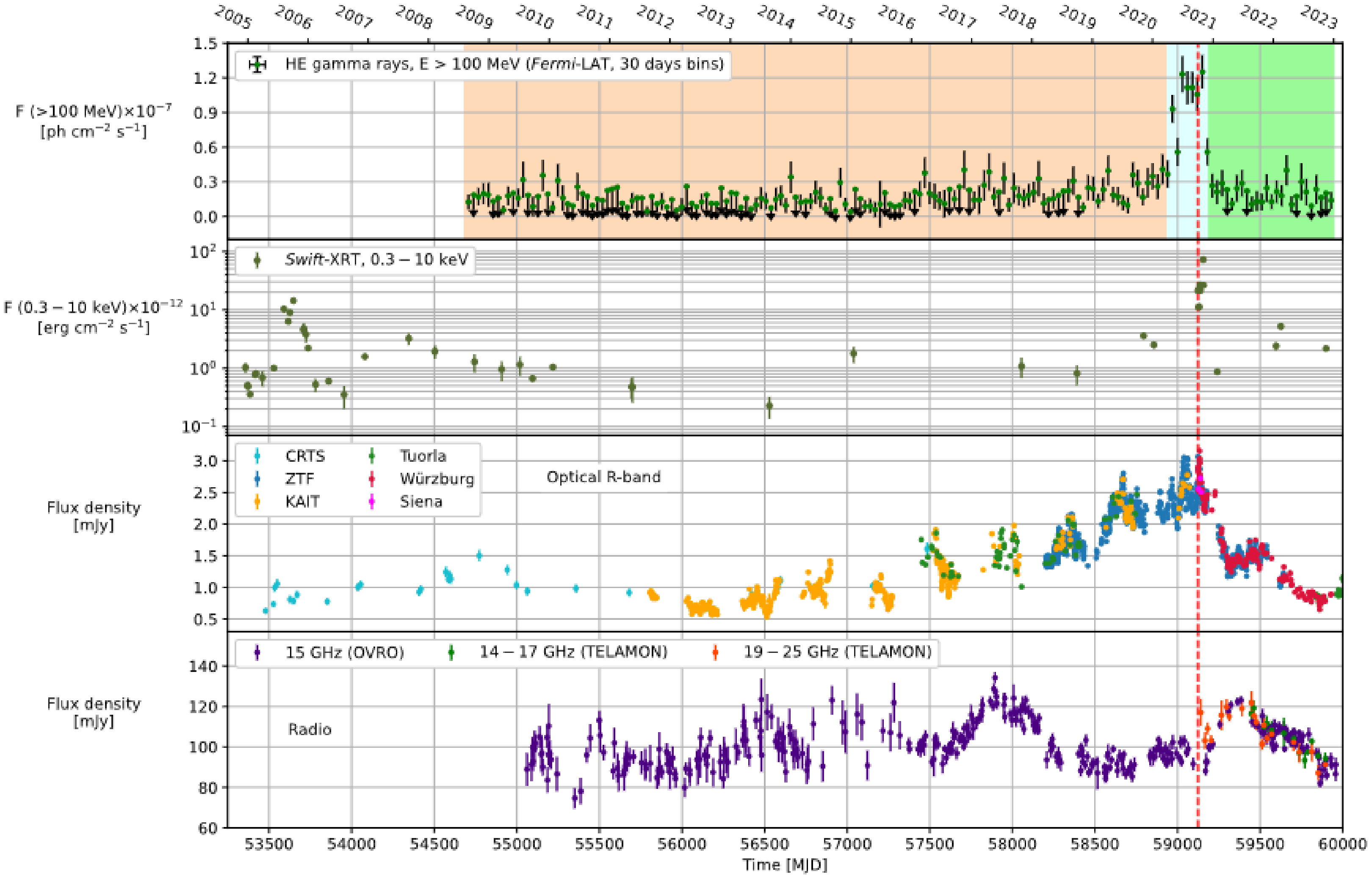

Figure 6.1: The long-term light curve of B2 1811+31, covering the period from 2005 to 2023, is divided into panels from top to bottom representing: HE γ-ray flux above 100 MeV from the Fermi-LAT monthly-binned data, X-ray flux in the 0.3–10 keV range from Swift-XRT, optical R-band data, and radio flux measurements. The red dashed line indicates the high-state detection by Fermi-LAT on October 1, 2020 (MJD 59123). The shaded bands, colored in light orange, light blue, and green, mark the ‘Pre-flare’, ‘Flare’, and ‘Post-flare’ periods, respectively (see Table 6.4) [155].

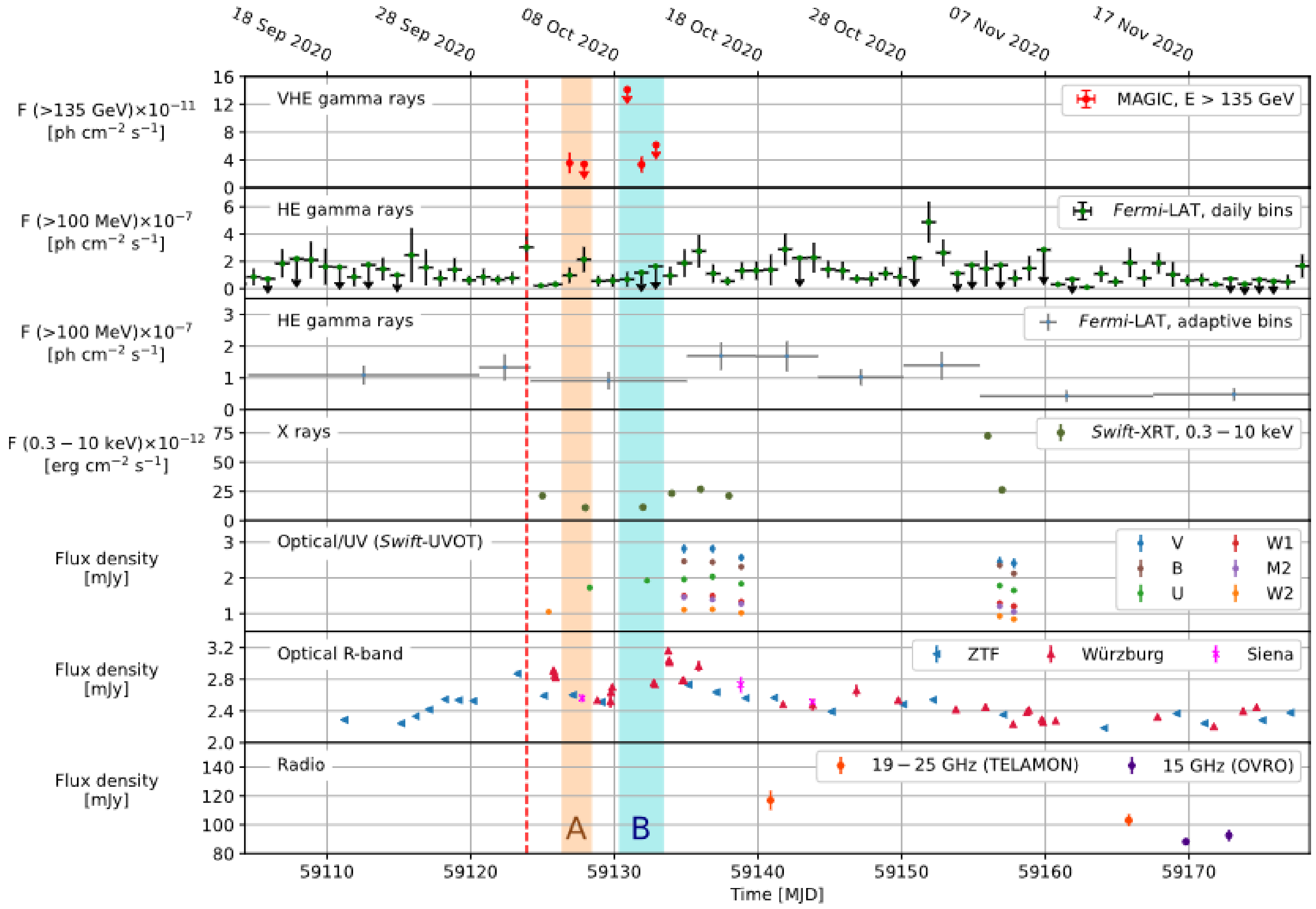

Figure 6.2: The MWL light curve for B2 1811+31, spanning approximately 80 days around the Fermi-LAT high-state detection on MJD 59123 (marked by the red dashed line), is divided into panels showing: VHE γ-ray flux above 135 GeV from MAGIC, HE γ-ray flux above 100 MeV from Fermi-LAT in daily bins with the ‘adaptive-binning’ method, X-ray flux in the 0.3–10 keV range from *Swift*-XRT, optical/UV data from the *Swift*-UVOT photometric filters, optical R-band data, and radio flux measurements. The light orange and blue bands represent 48-hour and 72-hour periods surrounding the two sets of consecutive MAGIC observation nights, respectively, defined as Periods A and B in Section 6.5 and Tables 6.3 and 6.9 [155].

Table 6.1: This table summarizes the instruments that participated in the multi-wavelength (MWL) campaign on B2 1811+31 during the 2020 γ-ray flare, along with their respective sensitivity ranges. For the optical and UV telescopes, the photometric filters used in this study are also provided. The *Fermi*-LAT detected the high state of the source on October 1, 2020 (MJD 59123). Since *Fermi*-LAT operates in sky survey mode, the approximate MJD start and stop times are provided, indicating the beginning and end of the 2020 γ-ray flare (as shown in Figure 6.1). For all other instruments, the MJD start and stop times correspond to observations conducted within the MJD 59100 - 59180 period (as depicted in Figure 6.2).

Instrument	Sensitivity range	MJD start	MJD stop
MAGIC	20 GeV - 100 TeV	59127	59133
Fermi-LAT	30 MeV - 1 TeV	58940	59190
Swift-XRT	0.2 - 10 keV	59125	59158
Swift-UVOT	v, b, u, w1, m2, w2 ($\approx 190 - 600$ nm)	59125	59158
ZTF Observatory	g, r, i ($\approx 400 - 800$ nm)	59111	59180
Wurzburg, Siena Observatory	R ($\approx 520 - 800$ nm)	59126	59174
TELAMON	14 - 25 GHz	59141	59166
OVRO	15 GHz	59169	59177

6.1.1 MAGIC Observations

After the high-state detection by Fermi-LAT in the HE γ-ray band, the MAGIC telescopes conducted observations of B2 1811+31 from October 5, 2020 (MJD 59127) to October 11, 2020 (MJD 59133). A total of about 5 hours of high-quality data, collected under atmospheric transmission greater than 85%, dark time, and a wide zenith range from 20° to 65°, was obtained over five observation nights. The night-wise time intervals and zenith ranges of the MAGIC observations are listed in Table 6.2. Data analysis was performed using the MAGIC analysis and reconstruction software, MARS [141]. Cuts based on the variable θ^2, defined as the squared angular distance between the reconstructed shower direction and the source direction, was employed to search for any significant VHE γ-ray excess with respect to the background. A combined dataset from all five observation nights was used for the analysis. The presence of VHE γ-ray emission from B2 1811+31 was confirmed with a statistical significance of 5.3σ. The statistical significance was estimated using the formula from [156].

Table 6.2: Summary of MAGIC observations of B2 1811+31. For each night, the observing time after quality cuts, the zenith range, the significance of the excess of γ-ray signal from the source and the gamma-ray flux integrated above 135 GeV are reported. Upper limits (ULs) at 95% confidence level are provided for the observations with significance of the γ-ray signal from the source below 3σ.

Start time [MJD]	Stop time [MJD]	Observing time [h]	Zenith range [deg]	Significance	Flux (E > 135 GeV) [10^{-11} ph cm^{-2} s^{-1}]	UL [10^{-11} ph cm^{-2} s^{-1}]
59126.84	59126.86	0.48	20 – 30	4.7 σ	3.55 ± 1.50	–
59127.84	59127.88	0.73	20 – 37	1.2 σ	–	3.37
59130.93	59130.97	0.98	50 – 64	-0.7 σ	–	14.1
59131.83	59131.95	1.96	20 – 64	4.3 σ	3.32 ± 1.15	–
59132.86	59132.91	1.30	30 – 50	2.1 σ	–	6.17

The night-wise VHE γ-ray flux for energies above 135 GeV was derived. The energy threshold was optimized to ensure accurate flux estimation for each night, accounting for observational conditions such as zenith range, weather, and night sky background levels. The MAGIC light curve for $E > 135$ GeV is provided in Table 6.2, along with the night-wise significances of the VHE γ-ray signal from B2 1811+31. The light curve is shown in the top panel of Figure 6.2, where 95% confidence level upper limits are indicated as downward arrows in VHE γ-rays when the significance is below 3σ. Since the flux levels for each observation night are consistent within the 1σ statistical uncertainty band, no significant variability was observed in the VHE light curve. The weak signal prevented further investigation of intra-night variability.

The B2 1811+31 MAGIC observations were divided into two datasets based on the results of dedicated MWL analyses conducted in the periods surrounding the MAGIC observations listed in Table 6.2. The first dataset consists of the initial two observations, carried out around MJD 59126.9 and MJD 59127.9, corresponding to October 5-6, 2020. The subsequent three MAGIC observations, forming the second dataset, were carried out from approximately MJD 59123.9 to MJD 59133.9, corresponding to October 9-11, 2020. In Figure 6.2, the light orange vertical band indicates a 48-hour region centered on the first two MAGIC observation times ('Period A'), extending from MJD 59126.4 to MJD 59128.4, while the blue band represents a 72-hour period centered on the next three MAGIC observations ('Period B'), extending from MJD 59130.4 to MJD 59133.4.

Dedicated *Fermi*-LAT analyses were performed to search for differences in the source states during these two periods.

For each period, the overall spectrum was evaluated by combining the data obtained during the observations within the same period and fitting it with a power-law (PL) function

$$\frac{\mathrm{d}N}{\mathrm{d}E} = N_0 \left(\frac{E}{E_0}\right)^{-\Gamma_{\mathrm{PL}}} , \tag{6.1}$$

with photon index Γ_{PL}, normalization constant N_0, and decorrelation energy E_0. To reconstruct the intrinsic spectra of the source in the two periods, the observed spectra were unfolded using the Tikhonov method [157] and corrected for γ-ray absorption due to interaction with the Extragalactic Background Light (EBL) using a model for the EBL in the co-moving frame at different redshifts [50]. The intrinsic spectra are soft, with $\Gamma_{\mathrm{PL}} = 4.16 \pm 0.63_{\mathrm{stat}}$, $E_0 = 130.95$ GeV, and $N_0 = (4.21 \pm 1.51_{\mathrm{stat}}) \times 10^{-10}$ TeV^{-1} cm^{-2} s^{-1} for Period A, and $\Gamma_{\mathrm{PL}} = 3.75 \pm 0.40_{\mathrm{stat}}$, $E_0 = 125.16$ GeV, and $N_0 = (7.36 \pm 1.99_{\mathrm{stat}}) \times 10^{-10}$ TeV^{-1} cm^{-2} s^{-1} for Period B (Table 6.3). The soft spectra in the VHE γ-ray range suggest that the HE bump of the SED is likely peaking at lower energies.

Table 6.3: Summary of the VHE γ-ray spectral analyses of MAGIC data on B2 1811+31 during the two observing periods. The periods were denoted as A and B, as indicated in the text. The resulting SEDs are shown in Figure 6.7.

Period	Start time [MJD]	Stop time [MJD]	Γ_{PL}	$N_0 \times 10^{-10}$ [TeV^{-1} cm^{-2} s^{-1}]	E$_0$ [GeV]
A	59126.84	59127.88	4.16 ± 0.63	4.21 ± 1.51	130.95
B	59130.93	59132.91	3.75 ± 0.40	7.36 ± 1.99	125.16

6.1.2 *Fermi*-LAT Monitoring

The *Fermi Large Area Telescope* (LAT) on the Fermi satellite is an imaging, wide field-of-view ($\sim$ 2.4 sr at a few GeV) γ-ray instrument sensitive to photons between 30 MeV and 1 TeV [158]. On October 1, 2020 (MJD 59123), *Fermi*-LAT detected a hard-spectrum GeV flare from B2 1811+31. The daily γ-ray flux at $E > 100$ MeV increased by a factor of 11 compared to the average value in the 4FGL, with a photon index of 1.4 ± 0.2, harder than the 2.14 ± 0.6 value in the 4FGL. Several photons above 10 GeV were also detected, including one at 61 GeV, with a $>$ 99% probability of emission from B2 1811+31 [154].

The analysis utilized standard tools for data processing and modeling [159, 160]. Photon events from the relevant data class, with energies between 100 MeV and 1 TeV and directions within 15° of B2 1811+31, were selected. Instrument response functions were applied, and quality cuts were enforced. A zenith angle cut of 90° was made to minimize contamination from the Earth limb. Sources within 20° of B2 1811+31, as well as the Galactic and isotropic background emissions, were included in the model.

To evaluate the γ-ray signal significance, a maximum-likelihood test statistic (TS) was employed, defined as $\mathrm{TS} = 2\left(\log L_1 - \log L_0\right)$, where L is the likelihood of the data given the model with ($L1$) or without ($L0$) a point-like source at B2 1811+31. Spectral analyses were performed for the low, high, and post-flare states. The "Flare" period corresponds to the 2020 γ-ray high state, while the "Pre-flare" spans from August 2008 to the start of the

2020 outburst, and the "Post-flare" extends from the end of the flare to January 2023. The boundaries of these periods were determined from the long-term *Fermi*-LAT light curve. The three periods are marked in the top panel of Figure 6.1.

In each period, a binned maximum-likelihood analysis was performed with energy bins of 8 per decade and angular coordinates of 0.1° per pixel. The normalizations of diffuse components and significantly detected sources within 5° from B2 1811+31 were left free, while the spectral parameters of other 4FGL sources were fixed to published values. The high-energy (HE) γ-ray spectrum of the source was modeled with a power-law (PL) function (eq. 6.1) with free normalization and spectral index. The resulting spectral energy distributions (SEDs) for the three periods are shown in 6.3a, and the PL best-fit parameters are reported in Table 6.4.

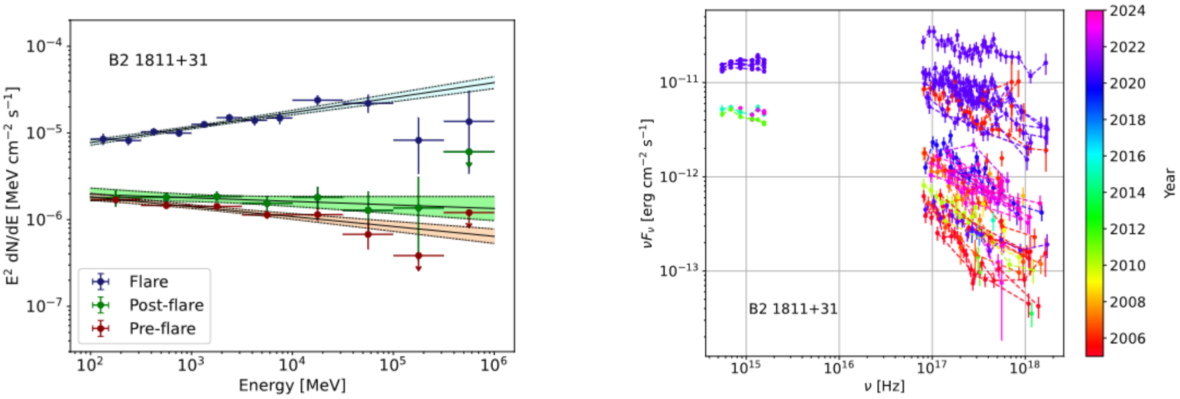

(a) SED of B2 1811+31 in the 100 MeV - 1 TeV energy range resulting from Fermi-LAT data

(b) Long-term evolution of the optical-to-X-ray SED of B2 1811+31

Figure 6.3: Two SEDs for B2 1811+31: (a) in the 100 MeV - 1 TeV energy range, and (b) in the optical-to-X-ray range [155].

During the flare, the source exhibited an average flux enhancement in the HE γ-ray band by a factor of ~ 6 compared to the low and post-flare states. The spectral index hardened from 2.11 ± 0.03 in the low state to 1.83 ± 0.02 in the high state, suggesting that the spectral break in the HE bump shifted to higher energies.

The curvature of the HE γ-ray spectra during the three periods was tested by fitting log-

Table 6.4: Summary of *Fermi*-LAT spectral analyses on B2 1811+31 during the high state in γ-rays occurred in 2020 ('Flare' period), from August 2008 up to the 2020 outburst ('Pre-flare') and after the high state up to January 2023 ('Post-flare').

Period	Start [MJD]	Stop [MJD]	$\Gamma_{\rm PL}$	F (>100 MeV) $\times 10^{-8}$ [ph cm^{-2} s^{-1}]
Pre-flare	54682	58940	2.11 ± 0.03	1.7 ± 0.1
Flare	58940	59190	1.83 ± 0.02	9.6 ± 0.5
Post-flare	59190	59945	2.04 ± 0.05	1.9 ± 0.3

Table 6.5: Summary of the curvature tests performed on the HE γ-ray spectra from *Fermi*-LAT data of B2 1811+31 during the 'Flare', 'Pre-flare' and 'Post-flare' periods. The table reports the TScurv values for the LP, PLEC and BPL models, defined as TScurv = $2\,(\log L_{\rm curved\ model} - \log L_{\rm PL})$.

Period	Start [MJD]	Stop [MJD]	TScurv, LP	TScurv, PLEC	TScurv, BPL
Pre-flare	54682	58940	4.1	6.6	2.0
Flare	58940	59190	4.8	7.7	1.7
Post-flare	59190	59945	2.3	2.2	1.5

parabola (LP), power-law with exponential cutoff (PLEC), and broken power-law (BPL) models [161]. The TS$_{\rm curv}$ test statistic, defined as TS$_{\rm curv}$ $= 2\,(\log L_{\rm curved\ model} - \log L_{\rm PL})$, was used. No significant improvement in the fit was found up to the 3σ significance level. The spectral break of the HE bump in the 2020 flare SED lies around tens of GeV, where uncertainties due to *Fermi*-LAT's sensitivity become relevant.

To investigate the long-term variability, the light curve from August 2008 to January 2023 was evaluated in 30-day bins using maximum-likelihood fits in each bin. The fit left free the normalization of the B2 1811+31 PL spectral model, while the photon index and spectral parameters of other sources were fixed. The resulting light curve is shown in Figure 6.1. Upper limits at 95% confidence are indicated as downward arrows for bins with a TS < 4 ($\sim 2\ \sigma$ significance). A sanity check confirmed that the flux-to-error ratio is approximately proportional to $\sqrt{TS}$ for all time bins, as prescribed by [162].

The long-term light curve shows that the source entered a high state several months before the flare on MJD 59123. The flaring state began around MJD 58940, where the flux increased by at least a factor of 2. The end of the flaring state was set to MJD 59190, when the flux dropped significantly. No other high states were recorded between 2008 and the 2020 flare or after that event.

A notable feature is the gradual evolution of flux during the 2010-2012 period, while the flux began to increase as the 2020 flare approached. This long-term evolution, as observed in other wavebands, is discussed in the following sections.

The fast variability during the 2020 flare was examined by computing the daily light curve in a period of approximately 80 days surrounding the MAGIC observations. Time bins were centered on the MAGIC observing times, and the light curve was also constructed using an adaptive-binning method [163] with adjustable bin widths to ensure constant relative flux uncertainty σ_F/F. Both the daily and adaptive-binned light curves are shown in Figure 6.2. Upper limits at 95% confidence are indicated for bins with TS < 4. On the day of the *Fermi*-LAT high-state observation, the flux was found to be $(3.0 \pm 1.0) \times 10^{-7}\,\mathrm{cm^{-2}\,s^{-1}}$, indicating a daily increase in flux by factor 18 ± 6 relative to the quiescent state.

Further analyses focused on differences in the γ-ray states within the MAGIC observation nights are presented in 6.5.1.

6.1.3 *Swift* Observations

The Neil Gehrels Swift satellite is a rapidly slewing, multi-wavelength observatory primarily designed for observing gamma-ray bursts and their X-ray and optical/UV afterglows [164]. It features three onboard instruments: the *Burst Alert Telescope* (BAT) [165], sensitive in the 15 - 350 keV range, the *X-Ray Telescope* (XRT) [166], sensitive to 0.2 - 10 keV photons, and the *UV/Optical Telescope* (UVOT) [167] covering the 190 - 600 nm range. Data from *Swift*-BAT were excluded from this analysis, as the hard X-ray fluxes from blazars are typically below the BAT sensitivity for typical exposure times of several ks. Standard *Swift* data-taking involves simultaneous observations with all three telescopes.

In addition to long-term monitoring, B2 1811+31 was observed 8 times in 2020 as part of the MWL campaign, with a total exposure time of 14.1 ks for both *Swift*-XRT and *Swift*-UVOT.

Swift-XRT

The reduced XRT data used for this study were obtained from the UK *Swift Science Center* [168]. Calibrated source and background files, along with the corresponding response files, were used as inputs for spectral fitting with XSPEC v12.13.1 [169], through the PyXspec v2.1.2 interface.

XRT observations in photon-counting (PC) mode were analyzed. Spectra in the 0.3 - 10 keV range were fitted using the `tbabs` photon absorption model in XSPEC, combined with a power-law (PL) model (Eq. 6.1) and a broken power-law (BPL) model of the form:

$$\frac{\mathrm{d}N}{\mathrm{d}E} = \begin{cases} K\left(\frac{E}{E_0}\right)^{-\Gamma_{1,BPL}} & \text{if } E < E_{\text{break}} \\ KE^{\Gamma_{2,BPL}-\Gamma_{1,BPL}}\left(\frac{E}{E_0}\right)^{-\Gamma_{2,BPL}} & \text{if } E \geq E_{\text{break}}\ . \end{cases} \tag{6.2}$$

The neutral hydrogen (HI) column density, $N_H = 6.09 \times 10^{20}\,\text{atoms/cm}^2$, was fixed based on the value from [170], and molecular abundances were adopted from [171]. The spectral fitting used the Cash-statistic [172], with free parameters for the normalization and spectral index (or indices, in the case of the BPL model). The F-test [172] was employed to determine if the BPL model was preferred over the PL model at the 3σ significance level.

The results for B2 1811+31 from *Swift*-XRT during the 2020 γ-ray high-state period are reported in Table 6.6 In 2 of the 8 observations, the BPL model was preferred, showing a spectral break at $2\,\text{keV} - 3\,\text{keV}$. X-ray spectra were corrected for ISM extinction to reconstruct the intrinsic X-ray SED. A bin-by-bin correction was performed using the previously reported N_H value, with $\sigma_{\rm ISM}(E)$ representing the total photo-ionization cross-section of the ISM.

During the MAGIC observation period, two *Swift*-XRT observations (MJD 59128 and MJD 59132) yielded X-ray fluxes of $(11.0\pm0.6)\times10^{-12}$ and $(11.4\pm0.6)\times10^{-12}$ erg cm^{-2} s^{-1}, with PL spectral indices $\Gamma_{\rm PL} = 2.5 \pm 0.1$ and 2.6 ± 0.1, respectively. These measurements provided insights into the particle population in the source.

Table 6.6: Results from the spectral analyses of the *Swift*-XRT data from the B2 1811+31 high state, using HI column density of $N_{\rm H} = 6.09 \times 10^{20}$ atoms/cm^2. Cash statistic values assuming PL and BPL models for the source intrinsic spectrum are reported, as well as the corresponding F-statistic values and p-values for the spectral curvature test. The BPL model was preferred over the single PL model if p-value $< 2.7 \times 10^{-3}$, corresponding to 3σ confidence level. For the observations with BPL model favored over the PL one, the BPL best-fit spectral indices $\Gamma_{\rm 1,BPL}$, $\Gamma_{\rm 2,BPL}$ and energy break $E_{\rm break}$ are indicated rather than the PL index $\Gamma_{\rm PL}$. The normalization energy E_0 of the PL and BPL functional forms in Equations 1 and 2 was set to $E_0 = 1$ keV.

Start time [MJD]	Exposure [s]	C_{PL}/dof	C_{BPL}/dof	F-statistic/p-value	$\Gamma_{\rm PL}$ ($\Gamma_{\rm 1,BPL}$, $\Gamma_{\rm 2,BPL}$)	E$_{\rm break}$ [keV]	Flux [0.3 - 10 keV] [10^{-12} erg cm^{-2} s^{-1}]
59125.442	2476	221/245	220/243	0.55/0.58	2.54 ± 0.06	-	21.3 ± 0.8
59128.283	1303	125/153	124/151	0.61/0.54	2.50 ± 0.11	-	11.0 ± 0.6
59132.286	1171	126/149	126/147	0.58/0.56	2.58 ± 0.10	-	11.4 ± 0.6
59134.853	1489	171/201	171/199	0.58/0.56	2.56 ± 0.08	-	23.5 ± 1.1
59136.848	2003	246/271	235/269	$6.3/2.1 \times 10^{-3}$	$2.09 \pm 0.09, 2.83 \pm 0.26$	1.9 ± 0.4	24.5 ± 2.7
59138.851	1841	253/271	237/269	$9.08/1.5 \times 10^{-4}$	$2.14 \pm 0.08, 4.72 \pm 1.13$	3.0 ± 0.4	18.4 ± 3.5
59156.828	1948	277/322	276/320	0.57/0.56	2.22 ± 0.04	-	73.0 ± 2.1
59157.823	1839	242/248	241/246	0.51/0.60	2.36 ± 0.06	-	26.4 ± 1.0

The long-term evolution of B2 1811+31's X-ray SED in the 0.3 - 10 keV range (0.7×10^{17} - 2.4×10^{18} Hz) is shown in Figure 6.3b. Variability of more than two orders of magnitude at 10^{18} Hz is observed, with most high-flux SEDs corresponding to the 2020 flare. Some high-state X-ray SEDs, shown in red, were derived from 2005 observations during an X-ray

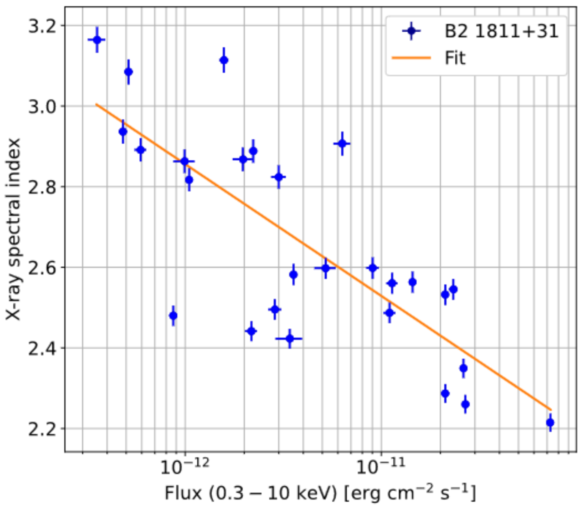

Figure 6.4: A scatter plot of the intrinsic power-law spectral index Γ_X and flux F_X in the 0.3 - 10 keV energy range from the long-term *Swift*-XRT observations of B2 1811+31. The orange line represents the fit with a linear function in the Γ_X - $\log_{10} F_X$ plane (Eq. 6.3) [155].

flare. Optical data from 2005 (CRTS) did not show a corresponding high state in the optical R-band (Figure 6.1). The SED evolution indicates a harder-when-brighter trend, where higher X-ray fluxes correspond to harder spectra. Both harder-when-brighter and softer-when-brighter trends have been observed in blazar X-ray emissions (e.g. for Mrk 421 and BL Lacertae, respectively) [173] [174].

Figure 6.4 represents the scatter plot of the intrinsic X-ray spectral index Γ_X and flux F_X in the 0.3–10 keV range, fit with a linear function:

$$\Gamma_X = p_0 + p_1 \log_{10} F_X \tag{6.3}$$

The Pearson coefficient $r = -0.77$, with a p-value of 2.2×10^{-6}, indicates a significant anti-correlation. The trend was fit with a linear function in the Γ_X-$\log_{10} F_X$ plane, yielding best-fit values of $p_0 = -1.1 \pm 0.6$ and $p_1 = -0.33 \pm 0.05$.

***Swift*-UVOT**

The UVOT data were processed using the `uvotimsum` and `uvotsource` tasks from the HEASOFT 6.32 software package, along with the Swift/UVOTA Calibration Database (CALDB) v20211108. Observations were made with the optical v, b, u and UV $w1$, $m2$, $w2$ broad-band filters [175, 176]. The `uvotsource` tool performed aperture photometry on the source, extracting counts from a 5 arcsecond radius region and background counts from a 20 arcsecond radius in a nearby contaminant-free area. To account for Galactic extinction, the method from [177] was applied using $E(B - V) = 0.0431 \pm 0.0017$ [178].

Table 6.7: Results from spectral analyses on B2 1811+31 *Swift*-UVOT observations taken during the MWL campaign organized during the γ-ray outburst in 2020. The table reports the intrinsic magnitudes, corrected for Galactic extinction effects.

Start time [MJD]	Exposure [s]	V [mag]	B [mag]	U [mag]	W1 [mag]	M2 [mag]	W2 [mag]
59125.442	2473	-	-	-	-	-	14.60 ± 0.02
59128.283	1260	-	-	14.83 ± 0.02	-	-	-
59132.286	1168	-	-	14.69 ± 0.02	-	-	-
59134.853	1449	15.34 ± 0.05	15.62 ± 0.03	14.69 ± 0.03	14.46 ± 0.03	14.29 ± 0.03	14.48 ± 0.03
59136.848	1953	15.34 ± 0.04	15.64 ± 0.03	14.63 ± 0.03	14.46 ± 0.03	14.33 ± 0.03	14.48 ± 0.02
59138.851	1787	15.44 ± 0.04	15.67 ± 0.03	14.74 ± 0.03	14.58 ± 0.03	14.43 ± 0.03	14.57 ± 0.03
59156.828	2003	15.54 ± 0.06	15.78 ± 0.03	14.85 ± 0.03	14.64 ± 0.03	14.50 ± 0.03	14.66 ± 0.03
59157.823	1798	15.56 ± 0.06	15.87 ± 0.03	14.92 ± 0.03	14.72 ± 0.03	14.66 ± 0.03	14.78 ± 0.03

The reconstructed magnitudes from the 2020 high-state observations are listed in Table 6.7. The long-term optical/UV SED evolution, shown in Figure 6.3b, indicates that during the 2020 high state, the optical/UV flux doubled compared to the quiescent state.

6.1.4 Optical Data

This study includes optical data from several surveys, observatories, and programs: the Zwicky Transient Facility (ZTF), [179], Katzman Automatic Imaging Telescope (KAIT)

[180], at Lick Observatory, Catalina Real-Time Transient Survey (CRTS) [181], the 0.3 m telescope at the Astronomical Observatory of the University of Siena, Würzburg Observatory (0.5 m), and the Tuorla blazar monitoring program [182]. The Tuorla program used data from the Kungliga Vetenskapsakademien (KVA) telescope until 2019 and since 2022 from the Jean Orò Telescope (TJO).

Survey data were extracted from their respective databases, while dedicated observations from Siena, Würzburg, and Tuorla were analyzed using standard differential photometry methods with a 5 arcsecond aperture.

The long-term light curve was constructed by combining survey data with dedicated observations, following the methodology outlined in [183]. The dedicated observations were carried out in the R-band, while the survey data encompassed various filters. Instrumental systematic discrepancies between data from different telescopes, such as variations in apertures and comparison stars, were corrected using offset adjustments based on Tuorla data, with the reference being simultaneous or quasi-simultaneous observations.

The B2 1811+31 fluxes were corrected for the contribution of the host galaxy, which was estimated to be 0.015 mJy within a 5 arcsecond aperture [184], and for Galactic extinction, which amounted to 0.094 mag in the R-band [178].

The 2020 flare corresponds to a significant high state in optical, X-ray, and γ-ray emissions. The long-term optical light curve reveals that this high state occurred at the apex of a gradual increase that had been ongoing since 2015-2016. Following the high state, the optical flux showed a faster decline compared to the timescale of the rise. The long-term evolution of the γ-ray flux exhibited a similar rising-peaking-falling pattern.

6.1.5 Radio Data

Radio data at 15 GHz were included from the AGN monitoring program of the 40 m Telescope at the Owens Valley Radio Observatory (OVRO) and from the TELAMON program conducted with the Effelsberg 100 m telescope at 14 - 17 GHz and 19 - 25 GHz. The TELAMON flux densities represent averages over multiple sub-frequencies within each band. The two sub-frequencies for the 14 - 17 GHz band are 14.25 GHz and 16.75 GHz, while the four sub-frequencies within the 19 - 25 GHz band are 19.25 GHz, 21.15 GHz, 22.85 GHz, and 24.75 GHz. High-level data were provided by the respective instrument teams. The data analysis procedures for the two radio telescopes are detailed in [185] for OVRO and [186] for TELAMON.

B2 1811+31 has been part of the OVRO monitoring program since 2009, offering long-term radio coverage that enables cross-correlation of the radio emission with data from the optical and γ-ray bands. The long-term radio light curve qualitatively follows a distinct trend compared to the light curves at higher frequencies. Notably, the two radio flares in 2017 and 2021, visible in the bottom panel of Figure 6.1, do not show a trivial correspondence with emissions at higher frequencies.

6.2 Variability of the Blazar B2 1811+31

6.2.1 Variability Analysis

The amplitude of variations in the radiative emissions from AGNs can be several orders of magnitude greater compared to astrophysical sources such as stars and non-active galaxies. The timescales of fast, coherent variations in the blazar emission in a given waveband are typically used, through causality arguments, to constrain the size R_b of the emission region dominating the radiative output in the same waveband. The observed variability timescales t_{var} for radiation are longer than the light-crossing time, which leads to the constraint

$$R_b \lesssim \frac{c\,\delta_D\,t_{\text{var}}}{1+z}\,, \tag{6.4}$$

where the Doppler boosting between the observer frame and the reference frame comoving with the emission region, as well as cosmological effects through the source redshift z, have been taken into account.

The relativistic Doppler factor is defined as:

$$\delta_D = \left[\Gamma(1-\beta\cos\theta)\right]^{-1} \,, \tag{6.5}$$

where $\Gamma = \left(1-\beta^2\right)^{-1/2}$ is the Lorentz factor, β denotes the velocity of the moving emission region, and θ is the angle between the velocity vector and the line of sight of the observer.

6.2.2 Short-timescale Variability

Constraints on the emission region size have been estimated from fast variability across various wavebands, including X-rays, HE γ-rays, and VHE γ-rays [187, 188]. In this work, the method from [188] is applied to infer the short-timescale variability of the HE γ-ray flux during the high-state period and quantify the significance of the estimate. The approach involves scanning the *Fermi*-LAT daily light curves (Figure 6.2 to determine the minimum doubling/halving time τ, defined by

$$F(t) = F(t_0)\, 2^{-(t-t_0)/\tau} \,, \tag{6.6}$$

where t and t_0 represent the centers of two consecutive time bins in which the source fluxes $F(t)$ and $F(t_0)$ were reconstructed from time bins with statistically significant detections, excluding those where only upper limits were derived. The significance of the estimated τ is calculated as

$$S = \frac{|F(t) - F(t_0)|}{\sqrt{\sigma^2_{F(t)} + \sigma^2_{F(t_0)}}} \,, \tag{6.7}$$

where $\sigma_{F(t)}$ and $\sigma_{F(t_0)}$ are the uncertainties on $F(t)$ and $F(t_0)$, respectively.

The resulting variability timescale with the highest significance levels are reported in Table 6.8. The MWL follow-up campaign on B2 1811+31 was triggered by the *Fermi*-LAT detection of elevated γ-ray emission. The days corresponding to the most significant variability timescales coincide with the periods surrounding the detection of the high state. The derived variability timescale with the highest significance is $t_{\mathrm{var}} \approx (3-6)\,\mathrm{h}$, implying

Table 6.8: Summary of the short-timescale variability analysis of the B2 1811+31 *Fermi*-LAT daily light-curves in Figure 6.2. Only the two variability timescales with the highest significance S are reported. If $F(t) > F(t_0)$, the corresponding τ is a doubling time, otherwise τ corresponds to a halving time.

t_0	t [MJD]	F(t_0) $\times 10^{-8}$ [ph cm^{-2} s^{-1}]	F(t) $\times 10^{-8}$ [ph cm^{-2} s^{-1}]	τ [h]	S
59122.9	59123.9	7.8 ± 4.4	30 ± 10	6.1	2.1
59123.9	59124.9	30 ± 10	2.1 ± 1.4	3.1	2.8

that the emission region size dominating the γ-ray flux, with relativistic Doppler factor δ_D, must satisfy

$$R_{\max} \approx (3-6) \times 10^{14}\,\delta_D\,\mathrm{cm}\,.$$

Variability timescales on the order of a few hours are consistent with those observed during flaring states of other TeV blazars [189, 190].

6.2.3 Variability in Timescales of Several Days

This section presents the analysis of the HE γ-ray flux variability on timescales of several days over a period of approximately 250 days surrounding the *Fermi*-LAT high-state observation. As shown in the long-term MWL light-curve (Figure 6.1), B2 1811+31 remained in a relatively high state from April 2020 (MJD $\approx$ 58940) to December 2020 (MJD $\approx$ 59190), preceding the *Fermi*-LAT high-state detection. This period is labeled 'Flare' in Table 6.1.

Figure 6.5 displays the *Fermi*-LAT light-curve with 7-day bins and the optical R-band light-curve during the Flare period. The two light-curves show a qualitatively similar flux evolution. Both light-curves exhibit repeating rising and falling trends. A double-exponential function

$$F(t) = A \cdot \begin{cases} 2^{\frac{t-t_{\text{peak}}}{t_{\text{rise}}}} & \text{if } t \leq t_{\text{peak}} \\ 2^{\frac{t_{\text{peak}}-t}{t_{\text{decay}}}} & \text{if } t > t_{\text{peak}} \end{cases} \tag{6.8}$$

was used to fit the peaks of the *Fermi*-LAT light-curve in the three highest-flux bins, which show similar trends to the optical R-band light-curve. In the MJD 58940–58970 range, the fit yielded $t_{\text{rise}} = (5.6 \pm 1.6)$ d and $t_{\text{decay}} = (4.5 \pm 1.6)$ d for the bump peaking at $t_{\text{peak}} = (58962 \pm 2)$ MJD. For the MJD 59020–59050 interval, the fit gave $t_{\text{rise}} = (7.4 \pm 2.1)$ d and $t_{\text{decay}} = (6.2 \pm 2.0)$ d, with $t_{\text{peak}} = (59042 \pm 2)$ MJD. The double-peak structure in the MJD 59110–59160 interval was modeled using two double-exponential functions (Eq. 6), resulting in $t_{\text{rise}} = (18 \pm 4)$ d for the first peak and $t_{\text{decay}} = (11 \pm 3)$ d for the second, although other temporal parameters were poorly constrained.

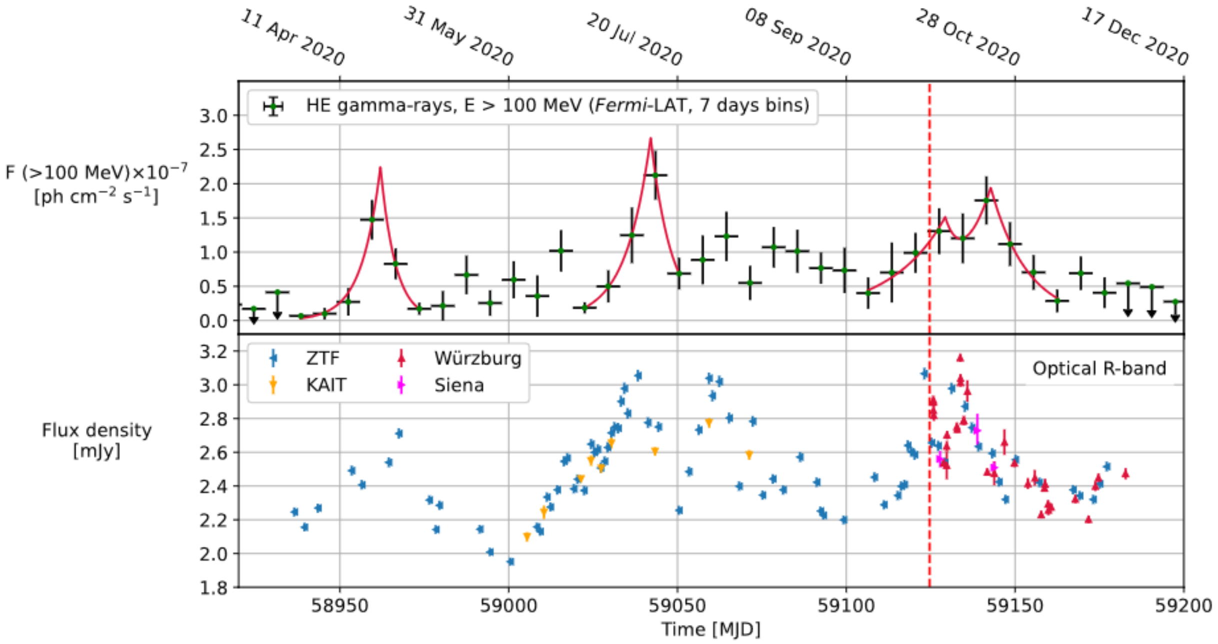

Figure 6.5: The MWL light-curve for B2 1811+31 in HE γ-rays (*Fermi*-LAT data in weekly bins, upper panel) and optical R-band (instruments are reported in the legend, lower panel) over a period of approximately 250 days surrounding the high state in October 2020. The red dashed line marks the *Fermi*-LAT high-state detection on MJD 59123. In the upper panel, the solid red lines show the double-exponential fit (Eq. 6.8) of the rising and falling trends in the *Fermi*-LAT light-curve [155].

6.3 Source Classification

BL Lac objects can be classified based on the frequency of the low-energy bump in their SED, into LBL, IBL, and HBL categories, as described in Section 1.1. During high states, the synchrotron peak frequency may shift significantly [191], and the classification in the high state can differ from that in the low state [192]. This section addresses the classification of the source in both low and high states.

B2 1811+31 is classified as IBL [150]. Figure 6.3b represents the evolution of the optical-to-X-ray SED from 2005 to 2024 using data from Swift-UVOT and Swift-XRT. Given the significant variability in the optical-to-X-ray SED, priority was given to simultaneous observations in order to select characteristic source states, as they ensure that all data correspond to the same emission state of the source and reduce the risk of combining fluxes from different variability phases. The observations considered representative of the low state are those from *Swift*-UVOT and *Swift*-XRT between May 13-24, 2011 (MJD 55694 - 55705). To improve statistics and flux estimation, additional *Swift*-UVOT and *Swift*-XRT observations from January 2015 were included, as they were fully compatible with the 2011 data. For the low state, infrared data from WISE [193], taken in March 2010, were also included at 3.4, 4.6, 12, and 22 μm (W1, W2, W3, W4 filters), extending the coverage to the infrared band.

For the high state, simultaneous *Swift*-UVOT and *Swift*-XRT data from 2020 were used. The synchrotron peak frequency was estimated by fitting the infrared-to-X-ray SED with a quadratic function in the log ν - $\log_{10} \nu F_\nu$ plane, given by:

$$\nu F(\nu) = f_0 10^{-b(\log_{10}(\nu/\nu_s))^2} \tag{6.9}$$

The resulting synchrotron peak frequency ν_s for the low and high states are:

- Low state: $\log_{10}(\nu_s/\mathrm{Hz}) = 14.71 \pm 0.03$
- High state: $\log_{10}(\nu_s/\mathrm{Hz}) = 15.21 \pm 0.23$

The fit of the selected data is shown in Figure 6.6. The quiescent state behavior aligns with that reported in The RGB Sample of intermediate BL Lacertae objects [150]. For the high state, the reconstructed synchrotron peak frequency is compatible, within uncertainties, with values around 10^{15} Hz. Consequently, the source classification during the high state is consistent with the transition region between IBL and HBL. Although the best-fit value of ν_s suggests an upward shift of the synchrotron peak frequency with respect to the quiescent state, the peak positions of the low and high states are compatible within approximately 2σ. The relatively large uncertainty on the high-state ν_s is likely related to the lack of quasi-simultaneous measurements in the relevant waveband, for example from *WISE* or similar instruments.

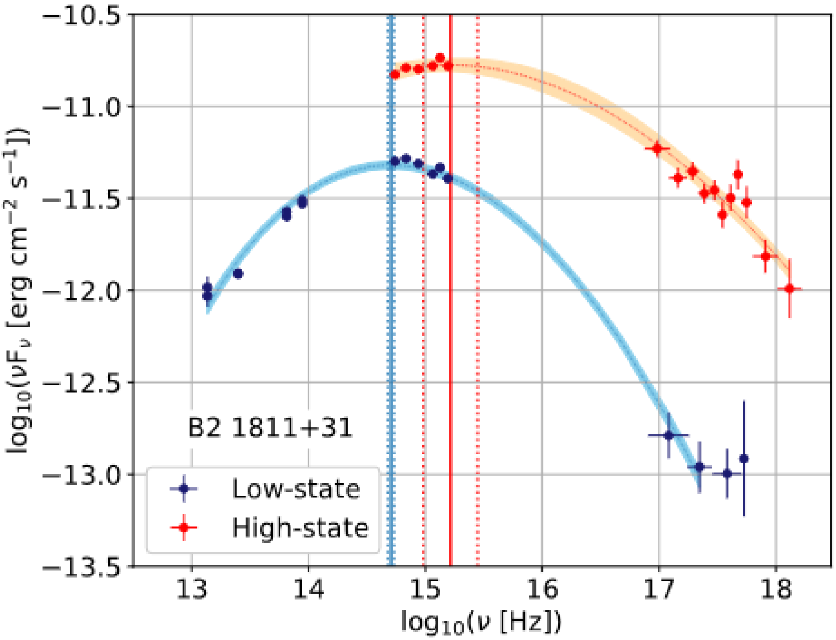

Figure 6.6: The infrared-to-X-ray SEDs characteristic of the low and high states of B2 1811+31 were fitted with a log-parabola function, shown in blue and red, respectively. The spectral points in the optical/UV range were reconstructed from *Swift*-UVOT observations, while the X-ray data were obtained from *Swift*-XRT. Infrared data were sourced from WISE. The observation periods for the data selected to represent the high and low states are discussed in the text. The shaded areas represent the 1σ uncertainty bands, while the best-fit synchrotron peak frequencies and their uncertainties are indicated by the solid and dashed vertical lines [155].

In Section 6.1.3, the harder-when-brighter trend of the X-ray emissions in the 0.3 - 10 keV range was analyzed. For HBLs and IBLs with ν_s close to 10^{15} Hz, this energy range typically corresponds to the falling edge of the synchrotron bump. These sources often display the harder-when-brighter trend, where freshly accelerated particles populate the high-energy tail of the particle distribution, enhancing flux and hardening the spectrum in the *Swift*-XRT energy range.

For LBLs and IBLs with ν_s near 10^{14} Hz, such as BL Lacertae, this energy range may correspond to the rising edge of the high-energy bump during the low state. Conversely, during high states, the falling edge of the synchrotron bump may extend into the X-ray band, leading to a softening of the spectral features during higher flux periods, i.e., the softer-when-brighter trend [194].

6.4 Redshift Estimation

The estimation of the redshift of BL Lac objects is challenging due to the weak or absent spectral lines in their optical/UV spectra. However, precise redshift measurement is crucial for γ-ray blazars, as γ rays above a few hundred GeV suffer extinction due to pair-production with the EBL (see Section 2.3). This results in a redshift-dependent suppression of the VHE γ-ray spectrum, which intensifies for higher energies and redshifts [195]. In BL Lac objects, photon fields external to the jet are expected to have little effect on VHE γ-ray absorption.

The redshift of B2 1811+31 was initially determined to be $z = 0.117$ based on spectroscopic observations with the *Isaac Newton Telescope* (INT) [152]. However, in 2003 it was suggested that the redshift could be higher [184]. The analysis presented in [184], based on imaging data from the *Nordic Optical Telescope* (NOT), showed that the host galaxy's effective half-light radius was inconsistent with typical BL Lac objects when assuming $z = 0.117$. By forcing the radial profile to follow the Kormendy relation for elliptical galaxies, they derived a higher redshift of $z = 0.28 \pm 0.03$.

To further refine the redshift estimate, the method from [196] was applied using simultaneous MAGIC and *Fermi*-LAT spectra. This method assumes that the slope of the EBL-corrected VHE spectrum should not be harder than the *Fermi*-LAT spectrum. An iterative procedure was used to correct the MAGIC data for EBL extinction and fit the spectral points with a power-law. The redshift range where the corrected spectral index agrees with *Fermi*-LAT data provides an estimate of z^*. Using the empirical relation between z^* and the true redshift [196], the estimate of the redshift for B2 1811+31 was found to be $z_{rec} = 0.22 \pm 0.14_{\text{stat}} \pm 0.05_{\text{syst}}$. This is consistent with the literature value $z = 0.117$ [152] and the value derived from the Kormendy relation. Despite the large statistical uncertainty due to the low significance of the detection, the result is coherent with the literature redshift $z = 0.117$, which was used as the reference for the broad-band modeling.

6.5 SED Modeling

The broad-band radiative emission from blazars is generally interpreted as originating from non-thermal particles accelerated to relativistic speeds within the jet. In the simplest model, the emission region is described as a spherical blob populated by electrons spiraling in a comoving magnetic field. This blob represents an idealized emission zone, which can correspond to various relativistic plasma configurations in the jet, such as superluminal knots, recollimations, or standing shocks. Observations of superluminal motion in AGN jets, at both pc-scales in radio and kpc-scales in optical and X-rays, support the existence of this bulk relativistic motion [197, 198, 199, 200]. Furthermore, the radiation observed in the Earth's reference frame is highly Doppler-boosted due to the bulk motion of the emission region and the small viewing angle, typically just a few degrees, from the jet axis.

In blazar jets, efficient particle acceleration occurs through processes like magnetic reconnection [201]. Various cooling mechanisms, both radiative and non-radiative, contribute to the overall cooling of particles [202]. Electrons lose energy through synchrotron radiation and inverse Compton (IC) scattering of low-energy photons. In BL Lacs, the intensity of external photon fields, such as from the accretion disk or BLR, is considered minimal compared to the non-thermal radiation from the jet. This is reflected in the weak or absent spectral lines in optical/UV observations. SSC (synchrotron self-Compton) models, where electrons upscatter their own synchrotron photons via IC scattering, are typically used to describe the SEDs of BL Lacs.

Alternatively, hadronic models have been employed to model the radiative states of some blazars [203, 204, 205]. These models gained increased interest following results from the *IceCube Neutrino Observatory*, which suggested a connection between high-energy neutrinos and blazars. In these models, neutrinos are produced from the decay of mesons formed during the interactions of relativistic protons with low-energy photon fields or nuclear targets. For example, a neutrino track event was linked to the IBL TXS 0506+056 during a γ-ray high state, with the detected neutrino having an energy of approximately 290 TeV, while several active galaxies were associated with neutrino hot spots. [206, 207]. However, B2 1811+31 is not associated with any IceCube neutrino events [208], so a purely leptonic model was used to describe the radiative state of the source during its 2020 flare.

6.5.1 Data Selection for the Broad-band SED Modeling

The B2 1811+31 MAGIC observations were divided into two datasets based on results from multi-wavelength (MWL) analyses around the times of these observations (Table 6.2). The first dataset includes the initial two observations, conducted on MJD 59126.9 and MJD 59127.9 (October 5-6, 2020). The second dataset includes three subsequent observations from MJD 59130.9 to MJD 59133.9 (October 9-11, 2020). In Figure 6.2, the light orange vertical band represents a 48-hour period centered on the first two observations ('Period A'), from MJD 59126.4 to MJD 59128.4, while the blue band marks a 72-hour period centered on the next three observations ('Period B'), extending from MJD 59130.4 to MJD 59133.4. The apparent offset arises because the time intervals are defined as symmetric windows centered on the MAGIC observation times, rather than starting at the first MAGIC data point. This choice is motivated by the requirements of the *Fermi*-LAT analysis.

To investigate differences in the source states, dedicated *Fermi*-LAT analyses were performed. Results are summarized in Table 6.9 and shown in Figure 6.7. The test statistics (TS) for source detection were $TS_{\mathrm{A}} = 24$ and $TS_{\mathrm{B}} = 37$. The reconstructed HE γ-ray spectra for both periods revealed a harder spectrum in Period B compared to Period A, with PL spectral indices of $\Gamma_{\mathrm{A}} = 2.5 \pm 0.3$ and $\Gamma_{\mathrm{B}} = 1.7 \pm 0.2$. The fluxes in the energy range above 100 MeV also differed between the two states: 21 ± 7 and 8 ± 4, in units of 10^{-8} ph cm^{-2} s^{-1}. Shorter 24-hour *Fermi*-LAT analyses centered on each MAGIC

Table 6.9: Summary of the HE γ-ray spectral analyses of *Fermi*-LAT data on B2 1811+31 during the periods of 48 and 72 hours centered on the two groups of observations performed with the MAGIC telescopes. The periods were denoted as A and B, as indicated in the text. Figure 6.7 shows the resulting SEDs.

Period	Start time [MJD]	Stop time [MJD]	Γ_{PL}	F ($>$ 100 MeV) $\times 10^{-8}$ [ph cm^{-2} s^{-1}]	$\mathrm{TS}_{\mathrm{PL}}$
A	59126.39	59128.39	2.5 ± 0.3	21 ± 7	24
B	59130.39	59133.39	1.7 ± 0.2	8 ± 4	37

observation showed similar trends, although with lower statistical significance. The EBL-corrected MAGIC spectra from periods A and B (Figure 6.7) were well-connected in Period B, but not in Period A, suggesting that rapid variations in the γ-ray spectrum observed by MAGIC were smoothed out in the *Fermi*-LAT analysis over longer integration times.

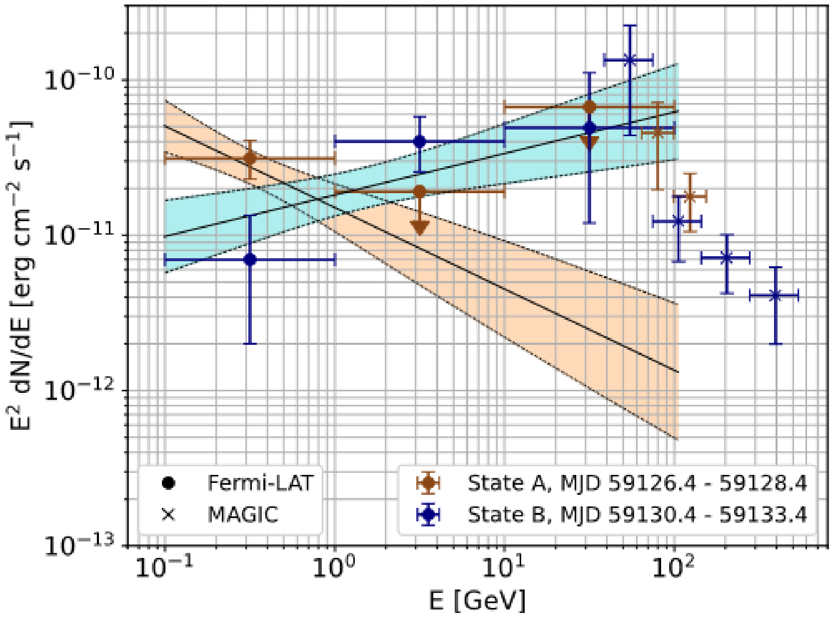

Figure 6.7: SED at HE and VHE γ-rays for B2 1811+31 during periods A and B, as defined in the main text, are shown in orange and blue, respectively. The points marked with round markers are derived from *Fermi*-LAT data. For both periods, the best-fit parameters of the spectrum reconstructed from *Fermi*-LAT observations are presented in Table 6.9, with the shaded regions indicating the corresponding 1σ uncertainty bands. The points marked with cross markers represent the MAGIC EBL-corrected SEDs, with the best-fit parameters given in Table 6.3 [155].

For state B, a broad-band SED was constructed using data that were simultaneous or quasi-simultaneous with the MAGIC observations. This SED includes the average EBL-corrected spectrum from the three MAGIC observations, along with the *Fermi*-LAT HE γ-ray SED and corresponding MWL data points. A similar analysis was not performed for state A due to the poor constraints in both HE and VHE γ-ray bands, leading to the modeling of the source in a single flaring state snapshot, specifically during Period B.

6.5.2 Broad-band SED Modeling

The synchrotron and SSC SEDs for modeling the emission from the source during its high state were computed using the open-source code `agnpy` [209]. The models were analyzed through a 'fit-by-eye' approach. As previously mentioned, the broad-band SED of BL Lacs is typically modeled using SSC models, primarily due to the minimal intensity of external photon fields within the jet.

6.5.3 One-zone Modeling of the SED

A one-zone SSC scenario was initially adopted, where a spherical emission region, moving with relativistic bulk Lorentz factor Γ, produces the majority of the radiative output. The emission region is populated by relativistic electrons with energy density $n_e(\gamma)$, where γ represents the Lorentz factors in the comoving frame. The electron energy distribution (EED) was modeled as a broken power-law:

$$n_e(\gamma) = k_e \left[\left(\frac{\gamma}{\gamma_b} \right)^{-p_1} H(\gamma; \gamma_{\min}, \gamma_b) + \left(\frac{\gamma}{\gamma_b} \right)^{-p_2} H(\gamma; \gamma_b, \gamma_{\max}) \right] , \tag{6.10}$$

where $H(x; a, b)$ is the Heaviside function, and k_e is the EED value at γ_b. The electron density is given by $K_e = \int_{\gamma_{\min}}^{\gamma_{\max}} d\gamma \, n_e(\gamma)$. The magnetic field in the region is B, and the energy densities in electrons and magnetic field are $u_e = m_e c^2 \int_{\gamma_{\min}}^{\gamma_{\max}} d\gamma \, \gamma n_e(\gamma)$ and $u_B = \frac{B^2}{8\pi}$, respectively. The energy equipartition parameter is defined as $k_{eq} = \frac{u_e}{u_B}$.

The EED indices p_1 and p_2 can be estimated from the MWL spectral data. Synchrotron radiation theory predicts that an electron population with $n_e(\gamma) \propto \gamma^{-p}$ radiates a synchrotron spectrum $\nu F_{\nu,\mathrm{synch}} \propto \nu^{\frac{3-p}{2}}$. During Period B, the X-ray spectrum of B2 1811+31 follows a power law with index $\Gamma_X = 2.58 \pm 0.10$ (Table 6.6), leading to $p_2 = 2\Gamma_X - 1 \approx 4.2 \pm 0.2$. The *Swift*-UVOT data in the optical/UV range show that $\nu F_\nu \propto \nu^{0.25 \pm 0.10}$, implying a spectral index of 2.5 ± 0.2 for the electron population. However, the high-state synchrotron peak lies near the optical/UV band, meaning that the electrons in this range have $\gamma \approx \gamma_b$, where the EED index changes.

The Doppler factor δ_D plays a crucial role in SSC models, influencing the observed radiation properties ($\nu F_\nu \propto \delta_D^4$). Typical values for blazars are $\delta_D \sim 10 - 20$ [210]. A one-zone SSC solution with $\delta_D = 20$ is shown in Figure 6.8, where the model parameters are provided in Table 6.10. This solution gives an upper limit for the emission region size of $R_{\max} \sim (6-12) \times 10^{15}$ cm. For lower values of δ_D, larger region sizes and magnetic fields were required to match the observed SED and variability constraints.

Table 6.10: SED modeling parameters for the one-zone and two-zone SSC model of the 2020 VHE γ-ray high state of B2 1811+31. Columns: (1) Model. (2), (3), (4) Minimum, break and maximum electron Lorentz factors. (5), (6) Slopes of the electron spectrum around the break. (7) Magnetic field strength. (8) Electron density. (9) Radius of the emission region. (10) Doppler factor. (11) Energy equipartition parameter.

Model (region)	$\gamma_{\rm min}$ [$\times 10^3$]	$\gamma_{\rm b}$ [$\times 10^4$]	$\gamma_{\rm max}$ [$\times 10^5$]	p_1	p_2	B [G]	K_e [cm^{-3}]	R_b [$\times 10^{15}$ cm]	δ_D	u_e/u_B
One-zone	0.7	3.2	3.0	1.9	4.4	0.13	7.6	10.6	20	31.3
Two-zone (blob)	6.0	4.0	3.0	2.0	3.8	0.38	7.95	4.0	10	18.3
Two-zone (core)	0.5	0.38	0.7	1.8	2.7	0.17	0.74	210	4	1.0

The magnetic field strengths in single-zone models are often lower than those required for equipartition [211]. In the solution presented in Figure 6.8, the equipartition parameter is $k_{eq} = 31.3$, significantly lower than the typical values found for single-zone models ($k_{eq} \sim 100$). Despite this, the solution still deviates from perfect equipartition ($k_{eq} = 1$) and requires a substantial break in the EED, with $p_1 = 2.0$ and $p_2 = 4.4$. This break is consistent with the estimate of $p_2 \sim 4.2 \pm 0.2$ from the X-ray spectrum. Due to synchrotron self-absorption at radio frequencies, single-zone models often fail to reproduce the observed radio flux, which is a common problem in modeling high-state SEDs [212].

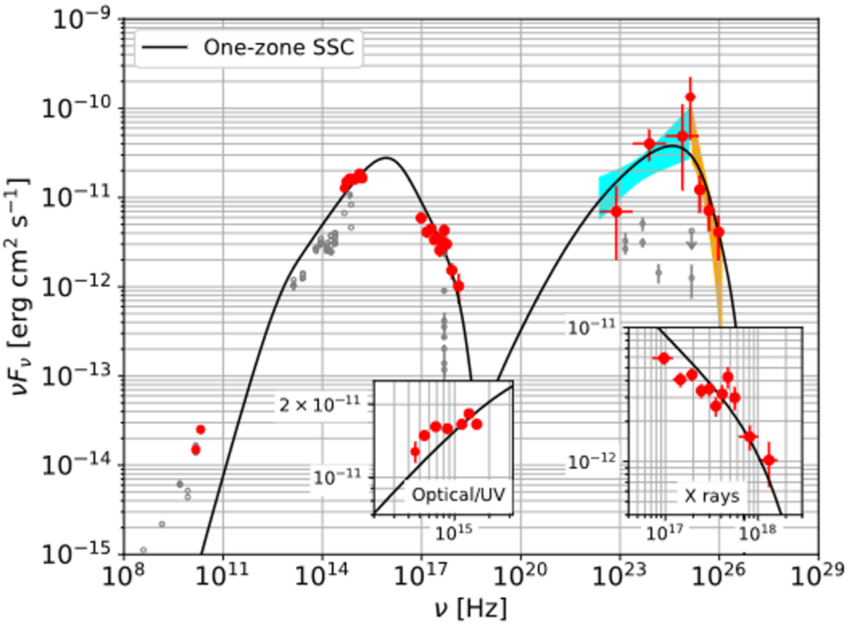

Figure 6.8: One-zone leptonic modeling of the broad-band SED of B2 1811+31 during Period B, corresponding to the 2020 high state in VHE γ-rays (marked by the red points). Archival data are represented by the hollow gray points. The blue and orange shaded areas indicate the 1σ uncertainty bands on the intrinsic spectrum of the source derived from *Fermi*-LAT and MAGIC observations, respectively. The inset panels provide zoom-ins on the optical/UV and X-ray bands.

6.5.4 Two-zone Modeling of the SED

A two-zone SSC model with modifications due to the BL Lac nature of the source was considered [213]. The external photon contribution to the inverse Compton scattering is neglected. The physical scenario involves two regions: a small, energetic 'blob' dominating X-ray and VHE γ-ray emissions, and a larger, less energetic 'core' region, contributing significantly to the optical/UV and HE γ-ray bands. The blob region is closer to the central engine, explaining its higher energy and magnetic field compared to the core. The two regions are assumed to be independent, with synchrotron photons from one region not significantly acting as seed photons for the other [213].

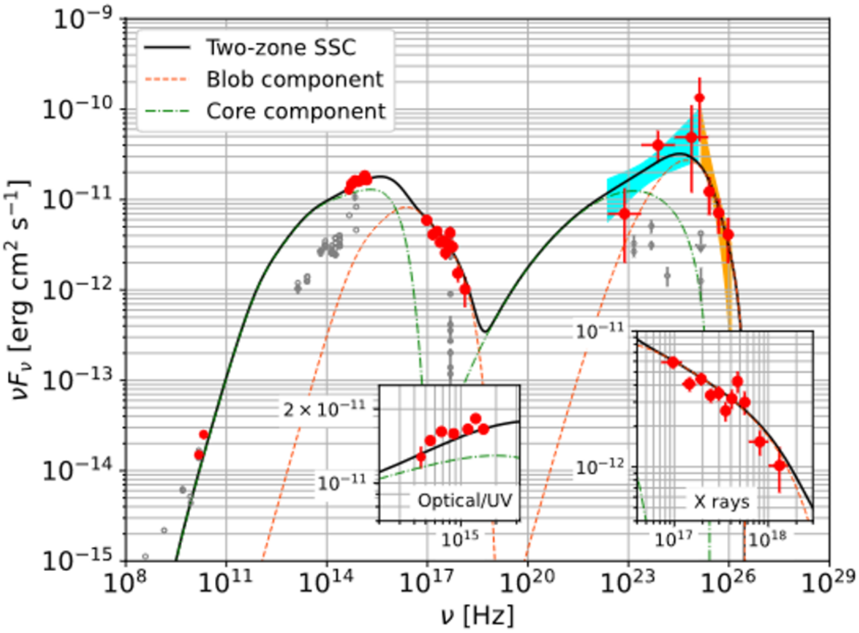

Figure 6.9: Two-zone leptonic modeling of the broad-band SED of B2 1811+31 during Period B, corresponding to the 2020 high state in VHE γ-rays (marked by the red points). Archival data are represented by the hollow gray points. The blue and orange shaded areas indicate the 1σ uncertainty bands on the intrinsic spectrum of the source derived from *Fermi*-LAT and MAGIC observations, respectively. For the two-zone SSC model, the contributions from the core and the blob are shown by the green and orange lines, respectively, while the total spectrum is obtained as the sum of the two components. The inset panels provide zoom-ins on the optical/UV and X-ray bands.

The two-zone model was constructed by following a similar procedure to the one-zone model. Various Doppler factors, δ_D, were tested for both regions, and the parameter space was explored, considering the constraints from the MWL analysis (Section 6.2). The model also incorporated self-consistent particle populations, accounting for escape and radiative cooling via synchrotron and SSC radiation [214, 215]. The final two-zone SSC solution, presented in Figure 6.9, fits the optical-to-X-ray SED better than the single-zone model, without requiring hard spectral breaks in the electron distributions. The EED indices for the core are $p_{1,\text{core}} = 1.8$ and $p_{2,\text{core}} = 2.7$, while for the blob, they are $p_{1,\text{blob}} = 2.0$ and

$p_{2,\mathrm{blob}} = 3.8$. The blob region's Doppler factor is $\delta_D = 10$, and the core region has $\delta_D = 4$. The size of the blob is constrained to $R_{\mathrm{blob}} = 4.1 \times 10^{15}\,\mathrm{cm}$, satisfying causality limits, with the electron energy range extending up to $E_{\max} \approx 150\,\mathrm{GeV}$. The core region successfully accounts for the radio flux, which was underestimated by the single-zone model.

The core region is at energy equipartition, while the blob has a modified equipartition coefficient ($k_{\mathrm{eq}} \approx 18$), in line with previous studies [212]. The time evolution of the EED was analyzed by considering particle acceleration, escape, adiabatic expansion, and radiative cooling [202]. In this context, the cooling timescales for both synchrotron and SSC processes play a crucial role. The synchrotron cooling timescale is given by:

$$t_{\mathrm{synch}}(\gamma) = \gamma \left(\frac{d\gamma}{dt}\right)^{-1}_{\mathrm{synch}} = \frac{3 m_e c}{4 \sigma_T u_B \gamma} \propto \gamma^{-1}\,. \tag{6.11}$$

This equation shows that the synchrotron cooling timescale t_{synch} is inversely proportional to the Lorentz factor γ, where m_e is the electron mass, c is the speed of light, σ_T is the Thomson scattering cross-section, and u_B is the magnetic field energy density.

Furthermore, the photon number density for the synchrotron radiation field in each region can be expressed as:

$$n_{\mathrm{ph}}(\epsilon) = \frac{3}{4}\frac{1}{m_e c^2 \epsilon}\frac{R_b}{c}\sqrt{3} e^3 B h \int_1^{\infty} d\gamma\, n_e(\gamma) R(x)\,. \tag{6.12}$$

This equation calculates the photon number density $n_{\mathrm{ph}}(\epsilon)$, where ϵ is the dimensionless photon energy, R_b is the size of the blob region, B is the magnetic field strength, and $n_e(\gamma)$ is the electron distribution. The factor $R(x)$ accounts for the synchrotron power, averaged over the electron pitch angles. This density is used to compute the inverse Compton scattering timescale.

The cooling timescales were compared to the light-crossing timescale $t_{\mathrm{lc}} = R/c$, as shown in Figure 6.10. For the blob region, the cooling timescales are dominated by synchrotron and SSC processes. The steady-state solution to the EED continuity equation predicts a spectral break $p_2 - p_1 = 1$, and the spectral break in the core region is consistent with cooling timescales scaling as γ^{-1}. The blob region requires a stronger break, suggesting possible deviations from equilibrium or cooling in the Klein-Nishina regime.

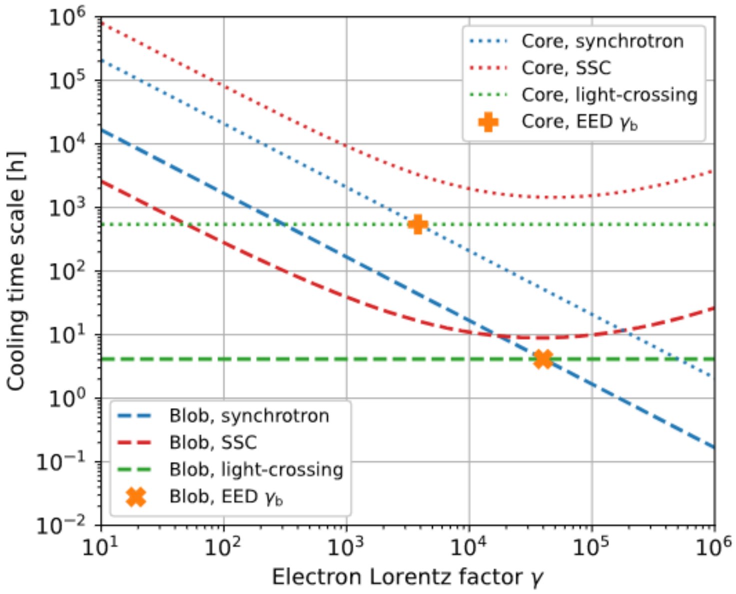

Figure 6.10: Comparison among the cooling timescales for the two-zone model in Figure 6.9, as a function of the electron Lorentz factor γ, is shown. The times are presented in the observer frame, i.e., corrected by the corresponding $(1+z)\delta_D$ with respect to the frames comoving with the two regions. Dashed (dotted) curves refer to the blob (core) region. Blue and red curves represent the synchrotron and SSC cooling timescales, respectively, while the green lines indicate the light-crossing times. The orange markers represent the γ_b values of the electron energy distribution (EED) within the two emission regions (see Table 6.10) [155].

The variability analysis in Section 6.2.2 provides an upper limit on the emission region size, $R_{\text{max}} = (1.8 \pm 0.4) \times 10^{17}\,\text{cm}$, for the core region with $\delta_D = 4$, which matches the core size $R_{\text{core}} = 2.1 \times 10^{17}\,\text{cm}$. The jet luminosity for both regions is computed as $L_e = 2\pi R^2\,\beta\,c\,\Gamma^2\,u_e$ and $L_B = 2\pi R^2\,\beta\,c\,\Gamma^2\,u_B$, where u_e and u_B are the energy densities in electrons and magnetic fields. The luminosities for the blob and core regions are $L_e \approx 1 \times 10^{43}\,\text{erg s}^{-1}$ and $L_B \approx 4 \times 10^{43}\,\text{erg s}^{-1}$.

In the two-zone model, the radio emission is not fully correlated with optical and γ-ray emissions. The core region accounts for up to 50% of the radio flux, but not entirely. Modifications in the core region's electron density and minimum electron energy could improve the fit to the radio data, while maintaining consistency with the SED at higher frequencies.

The solution shown in Figure 6.9 is one possible set of parameters, which satisfactorily reproduces the observed SED and ensures the self-consistency of the proposed physical scenario for the two regions.

Summary and Conclusions

Atmospheric Monitoring with LIDAR

Atmospheric absorption plays a critical role in the detection of high-energy gamma rays by IACTs, as variability caused by aerosols and clouds can affect energy reconstruction and source interpretation.

To support atmospheric monitoring at the MAGIC site, a micro-power elastic LIDAR system with HPD photon detection was developed. It provides afterpulse-free return signals with high charge resolution, allowing precise waveform digitization and effective separation of photo-electron signals from ion feedback. A laser upgrade in 2016 extended the maximum detection range from 22 km to about 31 km under clear conditions.

The system was calibrated over 24 time intervals, achieving a statistical uncertainty of 3% and systematic uncertainty of 2%. Using a dataset of 105 atmospheric profiles (2013–2020), the nocturnal boundary layer was characterized, showing two aerosol substructures and a curved profile influenced by local topography. Seasonal trends were identified, with best transmission in spring and strongest degradation during summer.

A cloud analysis algorithm retrieved cloud-averaged LIDAR ratios of 21±6 sr, consistent with cirrus cloud types C2 and C3. Temperature inversion effects on cloud top heights were also studied. The analysis revealed that during winter and spring, cloud layers tend to be confined below the lowest tropopause, effectively trapped by strong inversion layers. In contrast, summer clouds often extend several kilometers below the tropopause, occasionally reaching altitudes as high as 22 km a.s.l., indicating a seasonal variability in vertical cloud development.

Additionally, calibrated LIDAR data enabled extraction of night-sky background photon rates, revealing contributions from zodiacal light and galactic plane. The analysis also detected residual anthropogenic contributions to the 532 nm light background, especially before local midnight. After midnight, when only low-pressure sodium lamps remained, the residual background increased with zenith angle and correlated with more densely populated areas of the island.

Impact on CTAO Performance

In addition to analysis of LIDAR measurements, a large-scale database of simulated extensive air showers induced by gamma rays, protons, and electrons was generated using the CORSIKA code. The Cherenkov light in the wavelength range from 240 nm to 700 nm was also simulated, followed by telescope response simulations using `sim_telarray` software. These simulations, along with atmospheric transmission models produced with MODTRAN software, were used to assess the performance of the *Cherenkov Telescope Array Observatory* (CTAO) in the presence of clouds. A total of 36 transmission models were generated, differing in optical depth and cloud height.

The presence of clouds significantly degrades the performance of telescopes, primarily due to their optical depth. For clouds at altitudes greater than 11 km, the impact on performance is minimal, as the majority of air showers have a maximum below the cloud base. However, for lower clouds (up to 7 km), the energy threshold increases by up to 60%, and sensitivity is worsened by up to 20% above 1 TeV. The energy resolution at the threshold is degraded by 30% for low clouds and by less than 10% above 1 TeV. At energies above 150 GeV, both subarrays of the CTAO perform similarly. The reconstruction of direction remains manageable even in the presence of low, opaque clouds, with deviations from the shower axis remaining small.

A semi-analytical model of sensitivity degradation, consistent with Monte Carlo simulations, was introduced to summarize the influence of cloud optical depth and altitude on telescope performance. The model provides an accurate approximation for most cloud scenarios, although it fails to account for slight performance gains in cases of very low clouds (3 km a.g.l.).

Multi-Wavelength Study of B2 1811+31

Long-term multi-wavelength (MWL) observations of B2 1811+31 are also discussed as part of this work, with particular attention given to the 2020 gamma-ray flare. During this flare, MAGIC telescopes detected the first-ever very-high-energy (VHE) gamma-ray emission from this source. The MWL campaign covered the period of the flare, coordinated with *Fermi*-LAT observations, and provided a comprehensive view of the source's emission across radio to VHE bands.

The long-term behavior of B2 1811+31 revealed a correlation between optical and gamma-ray emissions, with the radio flux showing a distinct evolution. The source entered a flaring state following an increasing trend in the optical band, which lasted for approximately eight years. After the flare, the optical flux declined, returning to a state similar to that before the rising trend. This long-term rising-peaking-falling pattern was also observed in X-rays and gamma-rays. The X-ray flux exhibited a "harder-when-brighter" trend and varied by more than two orders of magnitude.

A significant shift in the synchrotron peak frequency was noted during the 2020 flare, suggesting that the source transitioned from an intermediate to a high-energy peaked blazar (HBL) state. The fast variability of the HE gamma-ray flux during the flare provided an upper limit on the size of the emission region. The SED was modeled using both one-zone and two-zone SSC scenarios, with the two-zone model offering a better fit, accounting for both optical/UV and X-ray bands without requiring extreme electron distribution parameters. The two-zone model is more consistent with energy equipartition and better describes the radio flux than the one-zone model.

Final Remarks and Outlook

This thesis presented the development, calibration, and application of a custom-designed, eye-safe LIDAR system for atmospheric monitoring at the MAGIC site. The system enabled precise characterization of aerosol and cloud layers, as well as night-sky background conditions, over several years of operation. These results align with previous atmospheric studies and contribute to a deeper understanding of the optical conditions at the ORM.

The findings are directly applicable to future ground-based gamma-ray observatories, particularly the CTAO-North, where atmospheric variability represents a critical factor in performance. Seasonal statistics of aerosol transmission and cloud distributions derived in this work can aid in optimizing observation scheduling and data quality control strategies at CTAO-North site.

Finally, the multi-wavelength study of the blazar B2 1811+31 during its 2020 flare contributed new insights into blazar variability and spectral evolution, revealing a transition to an HBL state and supporting a two-zone SSC emission scenario. This highlights the value of coordinated high-energy and multi-wavelength observations in constraining emission models of active galactic nuclei.

Overall, the work combines atmospheric science, simulation-based performance analysis, and astrophysical interpretation, offering relevant insights and practical tools that may support future research and observational planning in ground-based gamma-ray astronomy.

Contribution of the Doctoral Candidate to Research

Contribution to LIDAR and NSB Research

As part of this doctoral research, I independently investigated how the sensitivity of the MAGIC telescope's camera detectors is influenced by variations in the Night Sky Background (NSB), using data from the MAGIC Collaboration Database and LIDAR-based atmospheric transmission profiles collected between 2013 and 2020. This analysis was fully developed and executed by the doctoral candidate, including the design of the data selection criteria, statistical treatment of the NSB variations, and correlation studies with photoelectron background rates from the HPD detector with GaAsP photocathode.

A key contribution involved quantifying the combined effect of artificial light pollution and atmospheric transmission on the DC levels of the MAGIC cameras, and how this varies with azimuth and seasonal atmospheric conditions at the Roque de los Muchachos Observatory.

I also performed an independent analysis of the long-term LIDAR dataset to study cloud morphology, altitude distribution, and seasonal trends. This part of the work involved using the ROOT framework (based on C++) to create plots of vertical LIDAR return signal profiles, enabling the classification and visualization of cloud layers and the interpretation of their behavior in relation to local atmospheric structure.

These contributions support the broader goals of the MAGIC atmospheric monitoring program and are also relevant for the planning of future observations at the CTAO-North.

I contributed to the paper "Characterizing the aerosol atmosphere above the Observatorio del Roque de los Muchachos by analysing seven years of data taken with a GaAsP HPD-readout, absolutely calibrated elastic LIDAR," which was published in Monthly Notices of the Royal Astronomical Society in September 2022 [99]. My contributions to the paper were in Sections 7, 8, and 9 (Clouds, Analysis of 7 years of LIDAR data, and Night sky brightness, respectively).

Cross-check Analysis of CTAO Simulations

I also performed a cross-check analysis of Monte Carlo simulations for atmospheric conditions at the CTAO-North site (La Palma). These simulations aimed to investigate the impact of aerosol thickness and cloud properties, such as height and thickness, on critical CTAO-North telescope parameters. Specifically, the study focused on the differential sensitivity, energy resolution, and angular resolution of the telescopes. To achieve this, I utilized MAGIC Analysis and Reconstruction Software (MARS), adapted for CTAO, to analyze the simulated data. As anticipated, cloud effects were found to be most pronounced at low energies, particularly near the energy threshold. These findings are essential for enhancing the understanding of CTAO telescopes' performance under cloudy conditions. The results of this analysis were presented at the 37th International Cosmic Ray Conference (ICRC 2021), under the title “Performance of the Cherenkov Telescope Array in the Presence of Clouds” [138].

Furthermore, I contributed to the creation of new `sim_telarray` simulation files for protons, electrons, and gamma rays under specific atmospheric conditions at the CTAO-North site. `sim_telarray` is a software package that simulates the response of IACTs to extensive air showers produced by high-energy particles entering the Earth's atmosphere. These simulations help in understanding how the telescopes detect signals from cosmic particles and how atmospheric effects influence this detection.

The new simulations were designed to improve upon previous versions by increasing the statistical sample size and by including a broader range of atmospheric conditions, such as varying aerosol thickness, cloud height, and cloud thickness. The updated simulations thus provide a more detailed and realistic assessment of the CTAO-North performance under changing atmospheric conditions [138].

For these simulations, the high-performance computing resources of the University of Rijeka's supercomputer, Bura, were employed, enabling efficient processing of the large data volumes required.

Analysis of the VHE Source B2 1811+31

As part of my work within the MAGIC Collaboration, I served as the Flare Advocate during the MAGIC observational period 220 (October 2020). During this period, the collaboration reported the detection of very-high-energy (VHE) gamma-ray emission from the source B2 1811+31 using the MAGIC telescopes. This discovery was published in the Astronomer's Telegram on October 13, 2020 [154], and was presented at the remote MAGIC Collaboration Meeting later that year (November 9, 2020). I conducted a detailed analysis of the source B2 1811+31 detected in the VHE regime by the MAGIC telescopes, in October 2020. This involved producing light curves and spectral energy distributions (SEDs) for the observed sources, which were integrated into a multi-wavelength (MWL) picture of the detected Active Galactic Nuclei (AGN) sources. This analysis contributes to the broader understanding of AGN behavior across the entire electromagnetic spectrum, enabling a more comprehensive interpretation of their properties. I am also the corresponding author of the publication "Very-high-energy gamma-ray detection and long-term multi-wavelength view of the flaring blazar B2 1811+31," which was accepted for publication in Astronomy & Astrophysics in March 2025 and published in May 2025 [155].

Appendix A

Macro for Visualizing Transmission Data in Relation to DCs and Background in LIDAR Measurements

The source code developed during the doctoral research is available on the GitHub repository:

`https://github.com/lpavleti/Macro-for-Visualizing-Transmission`

This macro, written in C++ using the ROOT framework, is designed to analyze and visualize the relationship between atmospheric transmission measurements at different altitudes and detector counts (DCs) or background brightness levels from LIDAR data collected during the doctoral research.

The macro performs the following key tasks:

- Loads data from a ROOT TChain containing combined observational files.
- Creates multiple 2D histograms (`TH2F`) to plot various transmission metrics (e.g., transmission at 3 km, 4.5 km, 6 km, 9 km, and ratios between these) against DCs and brightness.

- Applies physical and data quality cuts, including filtering by zenith distance, angular distance from the telescope field of view, moon zenith distance, and galactic latitude to ensure reliable data selection.

- Fills histograms with filtered data, excluding non-physical or invalid transmission values (e.g., transmission values above 1).

- Generates canvases for graphical output and sets logarithmic scales for better data visualization.

- Implements profiles over histograms to extract median transmission trends.

- Fits linear functions to transmission profiles to quantify relationships.

- Supports azimuthal angle segmentation for more detailed directional analysis.

This tool enables detailed multi-parameter exploration of atmospheric transmission effects on observational data, which is useful for calibrating and understanding LIDAR measurements in the context of high-energy astrophysical observations.

List of Figures

List of Tables

Bibliography

[1] W. L. Kraushaar, G. W. Clark, G. P. Garmire, R. Borken, P. Higbie, V. Leong, and T. Thorsos, “High-energy cosmic gamma-ray observations from the oso-3 satellite,” The Astrophysical Journal, vol. 177, pp. 341–349, 1972.

[2] C. E. Fichtel, R. C. Hartman, D. A. Kniffen, D. J. Thompson, and R. C. Lamb, “The small astronomy satellite 2 (sas-2),” The Astrophysical Journal, vol. 177, pp. 341–349, 1972.

[3] NASA, “Vela 5a/b and 6a/b,” 2023, accessed: June 15, 2025. [Online]. Available: https://imagine.gsfc.nasa.gov/science/toolbox/missions/vela.html

[4] M. Collaboration, “Magic (major atmospheric gamma imaging cherenkov) florian goebel telescopes,” 2023, accessed: June 15, 2025. [Online]. Available: https://www.mpg.de/5571159/the-magic-telescopes

[5] V. A. Acciari, S. Ansoldi, L. A. Antonelli, A. Arbet Engels, K. Asano, D. Baack, and M. Collaboration, “Teraelectronvolt emission from the gamma-ray burst grb 190114c,” Nature, vol. 575, pp. 455–458, 2019, accessed: June 15, 2025. [Online]. Available: https://doi.org/10.1038/s41586-019-1707-3

[6] C. Consortium, “The cherenkov telescope array observatory: Ongoing development of the world’s premier ground-based gamma ray observatory,” 2024, accessed: June 15, 2025. [Online]. Available: https://spie.org/astronomical-telescopes-instrumentation/presentation/

The-Cherenkov-Telescope-Array-Observatory-CTAO--ongoing-development-of/13094-19

[7] E. Commission, "Ctao becomes a european research infrastructure consortium," 2025, accessed: June 15, 2025. [Online]. Available: https://www.eric-forum.eu/2025/01/22/ctao-becomes-a-european-research-infrastructure-consortium/

[8] L. Collaboration, "Observations of the crab nebula and pulsar with the large-sized telescope prototype of the cherenkov telescope array," arXiv, 2023, accessed: June 15, 2025. [Online]. Available: https://arxiv.org/abs/2306.12960

[9] Fermi Gamma-ray Space Telescope Team, "Fermi gamma-ray space telescope mission overview," 2025, accessed: June 15, 2025. [Online]. Available: https://fermi.gsfc.nasa.gov/science/mission/

[10] H.E.S.S. Collaboration, "High energy stereoscopic system (h.e.s.s.) gamma-ray observatory," 2025, accessed: June 15, 2025. [Online]. Available: https://www.mpi-hd.mpg.de/hfm/HESS/

[11] V. Collaboration and A. Team, "Veritas and agile gamma-ray observatories overview," 2025, accessed: June 15, 2025. [Online]. Available: https://veritas.sao.arizona.edu/

[12] D. Dominis Prester, J. Ebr, M. Gaug, A. Hahn, A. Babić, J. Eliášek, P. Janeček, S. Karpov, M. Kolarek, M. Manganaro, and R. Mirzoyan, "Characterisation of the atmosphere in very high energy gamma-astronomy for imaging atmospheric cherenkov telescopes," Universe, vol. 10, no. 9, p. 349, 2024. [Online]. Available: https://www.mdpi.com/2218-1997/10/9/349

[13] M. I. C. Martin, "Understanding blazar emission through multifrequency observations," Ph.D. dissertation, Universidad de La Laguna (Canary Islands, Spain), 2016.

[14] B. W. Carroll and D. A. Ostlie, An introduction to modern astrophysics. Cambridge University Press, 2017.

[15] T. Heckman, “An optical and radio survey of the nuclei of bright galaxies-Activity in normal galactic nuclei,” Astronomy and Astrophysics, vol. 87, no. 1-2, July 1980, p. 152-164. Research supported by the University of Washington., vol. 87, pp. 152–164, 1980.

[16] B. L. Fanaroff and J. M. Riley, “The morphology of extragalactic radio sources of high and low luminosity,” Monthly Notices of the Royal Astronomical Society, vol. 167, no. 1, pp. 31P–36P, 1974.

[17] Caltech Observatory, official webpage: https://cso.caltech.edu/.

[18] Caltech Observatory, official webpage: https://www.astro.caltech.edu/ovroblazars.

[19] C. M. Urry and P. Padovani, “Unified schemes for radio-loud active galactic nuclei,” Publications of the Astronomical Society of the Pacific, vol. 107, no. 715, p. 803–845, 1995.

[20] E. Y. Khachikian and D. W. Weedman, “An atlas of Seyfert galaxies,” Astrophysical Journal, vol. 192, Sept. 15, 1974, pt. 1, p. 581-589., vol. 192, pp. 581–589, 1974.

[21] J. M. Shuder, “Emission-line-continuum correlations in Active Galactic Nuclei,” Astrophysical Journal, Part 1, vol. 244, Feb. 15, 1981, p. 12-18., vol. 244, pp. 12–18, 1981.

[22] R. Antonucci and J. Miller, “Spectropolarimetry and the nature of NGC 1068,” The Astrophysical Journal, vol. 297, pp. 621–632, 1985.

[23] V. Beckmann and C. R. Shrader, Active Galactic Nuclei. Weinheim: Wiley-VCH, 2012.

[24] G. Ghisellini, C. Righi, L. Costamante, and F. Tavecchio, “The Fermi blazar sequence,” Monthly Notices of the Royal Astronomical Society, vol. 469, no. 1, pp. 255–266, 2017.

[25] A. Konigl, “Relativistic jets as X-ray and gamma-ray sources,” *Astrophysical Journal, Part 1, vol. 243, Feb. 1, 1981, p. 700-709.*, vol. 243, pp. 700–709, 1981.

[26] L. Maraschi, G. Ghisellini, and A. Celotti, “A jet model for the gamma-ray emitting blazar 3C 279,” *Astrophysical Journal, Part 2-Letters (ISSN 0004-637X), vol. 397, no. 1, p. L5-L9.*, vol. 397, pp. L5–L9, 1992.

[27] K. Murase, C. D. Dermer, H. Takami, and G. Migliori, “Blazars as ultra-high-energy cosmic-ray sources: implications for TeV gamma-ray observations,” *The Astrophysical Journal*, vol. 749, no. 1, p. 63, 2012.

[28] I. Collaboration, M. Aartsen, M. Ackermann, J. Adams, J. A. Aguilar, M. Ahlers, M. Ahrens, I. Al Samarai, D. Altmann, K. Andeen *et al.*, “Neutrino emission from the direction of the blazar TXS 0506+ 056 prior to the IceCube-170922A alert,” *Science*, vol. 361, no. 6398, pp. 147–151, 2018.

[29] S. Ansoldi, L. A. Antonelli, C. Arcaro, D. Baack, A. Babić, B. Banerjee, P. Bangale, U. B. De Almeida, J. A. Barrio, J. B. González *et al.*, “The blazar TXS 0506+ 056 associated with a high-energy neutrino: insights into extragalactic jets and cosmic-ray acceleration,” *The Astrophysical Journal Letters*, vol. 863, no. 1, p. L10, 2018.

[30] R. Abbasi, M. Ackermann, J. Adams, J. Aguilar, M. Ahlers, M. Ahrens, J. Alameddine, C. Alispach, A. Alves Jr, N. Amin *et al.*, “Improved characterization of the astrophysical muon–neutrino flux with 9.5 years of IceCube data,” *The Astrophysical Journal*, vol. 928, no. 1, p. 50, 2022.

[31] A. A. Abdo, M. Ackermann, M. Ajello, A. Allafort, E. Antolini, W. Atwood, M. Axelsson, L. Baldini, J. Ballet, G. Barbiellini *et al.*, “Fermi large area telescope first source catalog,” *The Astrophysical Journal Supplement Series*, vol. 188, no. 2, p. 405, 2010.

[32] M. L. Ahnen, S. Ansoldi, L. Antonelli, C. Arcaro, D. Baack, A. Babić, B. Banerjee, P. Bangale, U. B. De Almeida, J. Barrio *et al.*, “Multi-wavelength characterization

of the blazar S5 0716+ 714 during an unprecedented outburst phase," Astronomy & astrophysics, vol. 619, p. A45, 2018.

[33] G. a. Fossati, L. Maraschi, A. Celotti, A. Comastri, and G. Ghisellini, "A unifying view of the spectral energy distributions of blazars," Monthly Notices of the Royal Astronomical Society, vol. 299, no. 2, pp. 433–448, 1998.

[34] G. B. Rybicki and A. P. Lightman, Radiative Processes in Astrophysics. Wiley-VCH, 1979.

[35] G. R. Blumenthal and R. J. Gould, "Bremsstrahlung, synchrotron radiation, and compton scattering of high-energy electrons traversing dilute gases," Reviews of Modern Physics, vol. 42, p. 237–270, 1970.

[36] C. D. Dermer and R. Schlickeiser, "Model for the high-energy emission from blazars," The Astrophysical Journal, vol. 416, p. 458, 1993.

[37] K. P. Singh, S. Sahayanathan, and P. Kushwaha, "High-energy emission processes in oj287 during 2009 flare," ResearchGate preprint, 2013, https://www.researchgate.net/publication/254864773.

[38] eoPortal, "H.E.S.S. - High Energy Stereoscopic System," 2025, accessed: May 23, 2025. [Online]. Available: https://www.eoportal.org/other-space-activities/hess

[39] T. C. Weekes, M. F. Cawley, D. Fegan, K. Gibbs, A. Hillas, P. Kowk, R. Lamb, D. Lewis, D. Macomb, N. Porter et al., "Observation of TeV gamma-rays from the Crab nebula using the atmospheric Cherenkov imaging technique," Astrophysical Journal, vol. 342, pp. 379–395, 1989.

[40] M. Punch, C. W. Akerlof, M. F. Cawley, M. Chantell, D. Fegan, S. Fennell, J. Gaidos, J. Hagan, A. Hillas, Y. Jiang et al., "Detection of TeV photons from the active galaxy Markarian 421," Nature, vol. 358, no. 6386, pp. 477–478, 1992.

[41] F. Aharonian, A. Akhperjanian, M. Beilicke, K. Bernlöhr, H.-G. Börst, H. Bojahr, O. Bolz, T. Coarasa, J. Contreras, J. Cortina et al., "Is the giant radio galaxy M 87 a TeV gamma-ray emitter?" Astronomy & Astrophysics, vol. 403, no. 1, pp. L1–L5, 2003.

[42] D. Borla Tridon, F. Goebel, D. Fink et al., "Performance of the camera of the MAGIC ii telescope," arXiv e-prints, vol. arXiv:0906.5448, 2009, preprint, https://arxiv.org/abs/0906.5448, accessed 2025-10-19.

[43] J. R. Primack, A. Dominguez, R. C. Gilmore, and R. S. Somerville, "Extragalactic Background Light and Gamma-Ray Attenuation," in AIP Conference Proceedings, vol. 1381, no. 1. American Institute of Physics, 2011, pp. 72–83.

[44] W. Heitler, The quantum theory of radiation. Courier Corporation, 1984.

[45] P. Madau and E. S. Phinney, "Constraints on the extragalactic background light from gamma-ray observations of high-redshift quasars," The Astrophysical Journal, vol. 456, p. 124, 1996.

[46] S. W. Stahler and F. Palla, The formation of stars. John Wiley & Sons, 2008.

[47] P. J. E. Peebles, Principles of physical cosmology. Princeton university press, 1993, vol. 27.

[48] V. A. Acciari, S. Ansoldi, L. A. Antonelli, A. Arbet Engels, D. Baack, A. Babić, B. Banerjee, U. Barres de Almeida, J. Barrio, J. Becerra González et al., "Measurement of the extragalactic background light using MAGIC and Fermi-LAT gamma-ray observations of blazars up to z= 1," Monthly Notices of the Royal Astronomical Society, vol. 486, no. 3, pp. 4233–4251, 2019.

[49] A. Maeder, "An alternative to the ΛCDM model: The case of scale invariance," The Astrophysical Journal, vol. 834, no. 2, p. 194, 2017.

[50] A. Dominguez, J. R. Primack, D. Rosario, F. Prada, R. Gilmore, S. Faber, D. Koo, R. Somerville, M. Pérez-Torres, P. Pérez-González et al., "Extragalactic background light inferred from AEGIS galaxy-SED-type fractions," Monthly Notices of the Royal Astronomical Society, vol. 410, no. 4, pp. 2556–2578, 2011.

[51] R. C. Gilmore, R. S. Somerville, J. R. Primack, and A. Domínguez, "Semi-analytic modelling of the extragalactic background light and consequences for extragalactic gamma-ray spectra," Monthly Notices of the Royal Astronomical Society, vol. 422, no. 4, pp. 3189–3207, 2012.

[52] A. Franceschini, G. Rodighiero, M. Vaccari, S. Berta, L. Marchetti, G. Mainetti, and . . . , "Galaxy evolution from deep multi-wavelength infrared surveys: a prelude to *herschel*," Astronomy & Astrophysics, vol. 517, p. A74, 2010.

[53] K. Bernlöhr, "CORSIKA and sim_telarray–Simulation of the imaging atmospheric Cherenkov technique," 2001.

[54] NASA, "Van allen radiation belt," https://en.wikipedia.org/wiki/File:Van_Allen_radiation_belt.svg, 2012, accessed: 2025-10-19. Image via Wikimedia Commons. Licensed under CC BY-SA 4.0.

[55] L. G. Jacchia, "Revised static models of the thermosphere and exosphere with empirical temperature profiles," SAO Special Report# 332 (1971), vol. 332, 1971.

[56] C. Chamberlain, "Essentials of Meteorology: an Invitation to the Atmosphere, C. Donald Ahrens: book review," South African Geographical Journal= Suid-Afrikaanse Geografiese Tydskrif, vol. 91, no. 1, p. 56, 2009.

[57] R. J. States and C. S. Gardner, "Thermal structure of the mesopause region (80–105 km) at 40° N latitude. Part I: Seasonal variations," Journal of the Atmospheric Sciences, vol. 57, no. 1, pp. 66–77, 2000.

[58] D. o. P. Plymouth State University and E. Sciences, “Layers of the atmosphere,” https://vortex.plymouth.edu/dept/tutorials/atmosphere/layers.html, n.d., accessed: 2025-10-19.

[59] J. Carrillo, J. Guerra, E. Cuevas, and J. Barrancos, “Characterization of the marine boundary layer and the trade-wind inversion over the sub-tropical North Atlantic,” Boundary-layer meteorology, vol. 158, no. 2, pp. 311–330, 2016.

[60] N. . R. Project, “The ionosphere — the effects of earth’s upper atmosphere on radio signals,” https://radiojove.gsfc.nasa.gov/education/activities/iono.html, n.d., accessed: 2025-09-27.

[61] D. B. Newell, E. Tiesinga et al., “The international system of units (SI),” NIST Special Publication, vol. 330, pp. 1–138, 2019.

[62] H. Horvath, “Gustav Mie and the scattering and absorption of light by particles: Historic developments and basics,” Journal of Quantitative Spectroscopy and Radiative Transfer, vol. 110, no. 11, pp. 787–799, 2009.

[63] D. Hrupec, “Extragalactic Sources of Rapidly Variable High Energy Gamma Radiation,” Ph.D. dissertation, University of Zagreb, Faculty of Science, 2008.

[64] J. D. Jackson, Classical Electrodynamics, 3rd ed. New York: John Wiley & Sons, 1998.

[65] G. Mie, “Beiträge zur optik trüber medien, speziell kolloidaler metallösungen,” Annalen der Physik, vol. 330, p. 377–445, 1908, in German.

[66] M. Gaug, O. Blanch, D. Dorner, M. Doro, L. Font, C. Fruck, M. Garczarczyk, D. Garrido, D. Hrupec, J. Hose, A. López-Oramas, G. Maneva, M. Martinez, R. Mirzoyan, P. Temnikov, and R. Zanin, “Atmospheric Monitoring for the MAGIC Telescopes,” in International Workshop on Atmospheric Monitoring for High-Energy Astroparticle Detectors, Saclay, France, Mar. 2014.

[67] L. Elterman, “Uv, visible, and ir attenuation for altitudes to 50 km,” Air Force Cambridge Research Laboratories, Bedford, Massachusetts, Tech. Rep. AFCRL-68-0153, 1964, environmental Research Papers, No. 285.

[68] A. Ångström, “On the Atmospheric Transmission of Sun Radiation and on Dust in the Air,” Geografiska Annaler, vol. 11, pp. 156–166., 1929.

[69] G. Lombardi, V. Zitelli, and S. Ortolani, “The astroclimatological comparison of the Paranal Observatory and El Roque de Los Muchachos Observatory,” MNRAS, vol. 399, pp. 783–793, Oct. 2009.

[70] A. M. Varela, H. Vázquez Ramió, J. Vernin et al., “European Extremely Large Telescope Site Characterization III: Ground Meteorology,” PASP, vol. 126, no. 938, pp. 412–431, apr 2014.

[71] B. A. Laken, H. Parviainen, A. García-Gil et al., “Thirty Years of Atmospheric Extinction from Telescopes of the North Atlantic Canary Archipelago,” Journal of Climate, vol. 29, no. 1, pp. 227–240, 2016.

[72] S. L. Hidalgo, C. Muñoz-Tuñón, J. A. Castro-Almazán et al., “Canarian Observatories Meteorology; Comparison of OT and ORM using Regional Climate Reanalysis,” PASP, vol. 133, no. 1028, p. 105002, oct 2021.

[73] R. Rajkhowa, “Light pollution and impact of light pollution,” International Journal of Science and Research (IJSR), vol. 3, no. 10, pp. 861–867, 2014.

[74] L. P. Map. [Online]. Available: https://www.lightpollutionmap.info

[75] E. H. Palmén and C. W. Newton, Atmospheric circulation systems: their structure and physical interpretation. Academic press, 1969, vol. 13.

[76] S. Rodrıguez, C. Torres, J.-C. Guerra, and E. Cuevas, “Transport pathways of ozone to marine and free-troposphere sites in Tenerife, Canary Islands,” Atmospheric Environment, vol. 38, no. 28, pp. 4733–4747, 2004.

[77] T. I. Font, "El tiempo atmosférico en las islas Canarias," Servicio Meteorológico Nacional (INM), Serie A, vol. 26, 1956, available at https://repositorio.aemet.es/handle/20.500.11765/9616.

[78] A. H. De Lemps, Le climat des îles Canaries. Société d'édition d'enseignement supérieur, 1969, vol. 54.

[79] C. J. Torres, E. Cuevas, J. C. Guerra, and V. Carreño, "Caracterización de la capa de mezcla marítima y de la atmósfera libre en la región subtropical sobre Canarias," in 3a Asamblea Hispano-Portuguesa de Geodesia y Geofísica, Valencia, Spain, 2002, p. 1. [Online]. Available: https://www.divulgameteo.es/uploads/Caracterizaci%C3%B3n-masas-aire-Canarias.pdf

[80] S. Rodríguez, A. Alastuey, S. Alonso-Pérez, X. Querol, E. Cuevas, J. Abreu-Afonso, M. Viana, N. Pérez, M. Pandolfi, and J. De la Rosa, "Transport of desert dust mixed with North African industrial pollutants in the subtropical Saharan Air Layer," Atmospheric Chemistry and Physics, vol. 11, no. 13, pp. 6663–6685, 2011.

[81] K. Kandler, N. Benker, U. Bundke, E. Cuevas, M. Ebert, P. Knippertz, S. Rodríguez, L. Schütz, and S. Weinbruch, "Chemical composition and complex refractive index of Saharan Mineral Dust at Izaña, Tenerife (Spain) derived by electron microscopy," Atmospheric Environment, vol. 41, no. 37, pp. 8058–8074, 2007.

[82] G. Lombardi, V. Zitelli, S. Ortolani, M. Pedani, and A. Ghedina, "El Roque de Los Muchachos site characteristics. III. Analysis of atmospheric dust and aerosol extinction," A&A, vol. 483, pp. 651–659, May 2008.

[83] S. Rodríguez, Y. González, E. Cuevas, R. Ramos, P. M. Romero, J. Abreu-Afonso, and A. Redondas, "Atmospheric nanoparticle observations in the low free troposphere during upward orographic flows at Izaña Mountain Observatory," Atmospheric Chemistry and Physics, vol. 9, no. 17, pp. 6319–6335, 2009.

[84] J. Delgado, O. García, A. Díaz, J. Díaz, F. Expósito, E. Cuevas, X. Querol, A. Alastuey, and S. Castillo, "Origin and SEM analysis of aerosols in the high mountain of Tenerife (Canary Islands)," Natural Science, vol. 2, pp. 1119–1129, 2010.

[85] G. Lombardi, V. Zitelli, S. Ortolani, A. Ghedina, A. Garcia, E. Molinari, and C. Gatica, "New dust measurements at ORM, and comparison with Paranal Observatory," in Society of Photo-Optical Instrumentation Engineers (SPIE) Conference Series, vol. 7733, Jul. 2010, p. 77334G.

[86] D. Collins, H. Johnsson, J. Seinfeld, R. Flagan, S. Gasso, D. Hegg, P. Russell, B. Schmid, J. Livingston, and E. Ostrom, "In situ aerosol-size distributions and clear-column radiative closure during ACE-2," Tellus Series B, vol. 52, pp. 498–525, 2000.

[87] P. K. Quinn and T. S. Bates, "Regional aerosol properties: Comparisons of boundary layer measurements from ACE 1, ACE 2, Aerosols99, INDOEX, ACE Asia, TARFOX, and NEAQS," J. of Geophys. Res.: Atmospheres, vol. 110, no. D14, pp. 1–24, 2005.

[88] E. Andrews, O. J. A., P. Bonasoni, A. Marinoni, E. Cuevas, S. Rodríguez, J. Y. Sun, D. A. Jaffe, E. V. Fischer, U. Baltensperger, E. Weingartner, M. Collaud Coen, S. Sharma, A. M. Macdonald, W. R. Leaitch, N. H. Lin, P. Laj, T. Arsov, I. Kalapov, A. Jefferson, and P. Sheridan, "Climatology of aerosol radiative properties in the free troposphere," Atmospheric Res., vol. 102, no. 4, pp. 365–393, 2011.

[89] P. Murdin, "Nighttime skies above the Canary Islands," Vistas in Astron., vol. 28, pp. 449–465, 1985.

[90] D. C. B. Whittet, M. F. Bode, and P. Murdin, "The extinction properties of Saharan dust over la palma," Vistas in Astron., vol. 30, pp. 135–144, 1987.

[91] D. J. Stickland, C. Lloyd, C. D. Pike, and E. N. Walker, “The photometric properties of atmospheric dust over the La Palma observatory,” The Observatory, vol. 107, pp. 74–78, Apr. 1987.

[92] C. Muñoz-Tuñón, J. Vernin, and A. M. Varela, “Night-time image quality at Roque de los Muchachos Observatory,” A&AS, vol. 125, no. 1, pp. 183–193, 1997.

[93] A. Jímenez, H. González Jorge, and M. C. Rabello-Soares, “Diurnal atmospheric extinction over Teide Observatory (Tenerife, Canary Islands),” A&AS, vol. 129, pp. 413–423, Apr. 1998.

[94] A. García-Gil, C. Muñoz-Tuñón, and A. M. Varela, “Atmosphere Extinction at the ORM on La Palma: A 20 yr Statistical Database Gathered at the Carlsberg Meridian Telescope,” PASP, vol. 122, pp. 1109–1121, Sep. 2010.

[95] A. M. Varela, C. Bertolin, C. Muñoz-Tuñón, S. Ortolani, and J. J. Fuensalida, “Astronomical site selection: on the use of satellite data for aerosol content monitoring,” MNRAS, vol. 391, pp. 507–520, Dec. 2008.

[96] M. Sicard, M. N. M. Reba, S. Tomás, A. Comerón, O. Batet, C. Muñoz-Porcar, A. Rodríguez, F. Rocadenbosch, C. Muñoz-Tuñón, and J. J. Fuensalida, “Results of site testing using an aerosol, backscatter lidar at the Roque de los Muchachos Observatory,” MNRAS, vol. 405, no. 1, pp. 129–142, 2010.

[97] A. M. Hillas and J. R. Patterson, “Characteristics and brightness of Cerenkov shower images for gamma-ray astronomy near 1 TeV,” J. Phys. G-Nucl. Part. Phys., vol. 16, no. 8, pp. 1271–1281, August 1990.

[98] C. Fruck, M. Gaug, R. Zanin, D. Dorner, D. Garrido, R. Mirzoyan, and L. Font, “A novel LIDAR-based Atmospheric Calibration Method for Improving the Data Analysis of MAGIC,” in Proc. 33^{rd} ICRC, Rio de Janeiro, Brasil, 3 2014, p. 1054, arXiv:1403.3591.

[99] C. Fruck, M. Gaug, A. Hahn, V. Acciari, J. Besenrieder, D. Dominis Prester, D. Dorner, D. Fink, L. Font, S. Mićanović *et al.*, “Characterizing the aerosol atmosphere above the Observatorio del Roque de los Muchachos by analysing seven years of data taken with an GaAsP HPD-readout, absolutely calibrated elastic LIDAR,” *Monthly Notices of the Royal Astronomical Society*, vol. 515, no. 3, pp. 4520–4550, 2022.

[100] L. Font *et al.*, “Monitoring and calibration of the atmosphere in MAGIC,” in *Proceedings of the 33rd ICRC, Rio de Janeiro*, 2013, p. 0090. [Online]. Available: https://galprop.stanford.edu/elibrary/icrc/2013/papers/icrc2013-0090.pdf

[101] C. Fruck and M. Gaug, “Atmospheric monitoring in MAGIC and data corrections,” in *European Physical Journal Web of Conferences*, ser. AtmoHEAD 2014: Atmospheric Monitoring for High Energy AstroParticle Detectors, vol. 89, Mar 2015, p. 02003.

[102] M. Will *et al.*, “Atmospheric Monitoring at the Site of the MAGIC Telescopes,” *EPJ Web of Conferences*, vol. 01002, no. 144, 2017, proc. to the 2016 AtmoHEAD.

[103] V. A. Kovalev and W. E. Eichinger, *Elastic Lidar, Theory, Practice and Analysis Methods*. John Wiley & Sons, New York, 2005.

[104] R. T. H. Collis, “Lidar: A new atmospheric probe,” *Quarterly J. of the R. Meteorological Soc.*, vol. 92, pp. 220–230, Apr. 1966.

[105] F. G. Fernald, B. M. Herman, and J. A. Reagan, “Determination of Aerosol Height Distributions by Lidar.” *J. of Applied Meteorology*, vol. 11, pp. 482–489, Apr. 1972.

[106] C. M. R. Platt, “Remote Sounding of High Clouds: I. Calculation of Visible and Infrared Optical Properties from Lidar and Radiometer Measurements.” *J. of Applied Meteorology*, vol. 18, pp. 1130–1143, Sep. 1979.

[107] F. G. Fernald, “Analysis of atmospheric lidar observations: some comments,” *Applied Opt.*, vol. 23, no. 5, pp. 652–653, Mar 1984.

[108] J. D. Klett, “LIDAR inversion with varialbe backscatter/extinction ratios,” Applied Optics, vol. 24, pp. 1638–1643, 1985.

[109] E. V. Browell, S. Ismail, and S. T. Shipley, “Ultraviolet DIAL measurements of O3 profiles in regions of spatially inhomogeneous aerosols,” Applied Opt., vol. 24, no. 17, pp. 2827–2836, Sep 1985.

[110] J. A. Weinman, “Derivation of atmospheric extinction profiles and wind speed over the ocean from a satellite-borne LIDAR,” Applied Opt., vol. 27, no. 19, pp. 3994–4001, Oct 1988.

[111] V. A. Kovalev, “Lidar measurement of the vertical aerosol extinction profiles with range-dependent backscatter-to-extinction ratios,” Applied Opt., vol. 32, no. 30, pp. 6053–6065, Oct 1993.

[112] V. A. Kovalev and H. Moosmüller, “Distortion of particulate extinction profiles measured with LIDAR in a two-component atmosphere,” Appl. Optics, vol. 33, pp. 6499–6507, Sep. 1994.

[113] V. A. Kovalev, “Sensitivity of the LIDAR solution to errors of the aerosol backscatter-to-extinction ratio: influence of a monotonic change in the aerosol extinction coefficient,” Applied Opt., vol. 34, no. 18, pp. 3457–3462, Jun 1995.

[114] G. J. Kunz, “Transmission as an input boundary value for an analytical solution of a single-scatter lidar equation,” Appl. Opt., vol. 35, no. 18, pp. 3255–3260, Jun 1996.

[115] J. T. McGraw, P. C. Zimmer, M. R. Ackermann, D. C. Hines, A. B. Hull, L. Rossmann, D. C. Zirzow, S. W. Brown, G. T. Fraser, K. R. Lykke, A. W. Smith, C. W. Stubbs, and J. T. Woodward, “Ground-based observatory operations optimized and enhanced by direct atmospheric measurements,” in Modern Technologies in Space- and Ground-based Telescopes and Instrumentation, E. Atad-Ettedgui and D. Lemke, Eds., vol. 7739, International Society for Optics and Photonics. SPIE, Jul. 2010, pp. 847–864.

[116] T. Takamura and Y. Sasano, "Ratio of aerosol backscatter to extinction coefficients as determined from angular scattering measurements for use in atmospheric lidar applications," Optical and Quantum Electronics, vol. 19, pp. 293–302, 1987.

[117] Y. Sasano, E. V. Browell, and S. Ismail, "Error caused by using a constant extinction/backscatter ratio in the lidar solution," Applied Opt., vol. 24, pp. 3929–3932, 1985.

[118] S. A. Young, "Analysis of Lidar Backscatter Profiles in Optically Thin Clouds," Applied Opt., vol. 34, pp. 7091–7031, 1995.

[119] J. D. Klett, "Stable analytical inversion solution for processing LIDAR returns," Applied Opt., vol. 20, pp. 211–220, 1981.

[120] M. L. Ahnen, S. Ansoldi, L. A. Antonelli, C. Arcaro, A. Babić, B. Banerjee, P. Bangale, U. Barres de Almeida, J. A. Barrio, J. Becerra González, W. Bednarek, E. Bernardini, A. Berti, W. Bhattacharyya, B. Biasuzzi, A. Biland, O. Blanch, S. Bonnefoy, G. Bonnoli, R. Carosi, A. Carosi, A. Chatterjee, P. Colin, E. Colombo, J. L. Contreras, J. Cortina, S. Covino, P. Cumani, P. Da Vela, F. Dazzi, A. De Angelis, B. De Lotto, E. de Oña Wilhelmi, F. Di Pierro, M. Doert, A. Domínguez, D. Dominis Prester, D. Dorner, M. Doro, S. Einecke, D. Eisenacher Glawion, D. Elsaesser, M. Engelkemeier, V. Fallah Ramazani, A. Fernández-Barral, D. Fidalgo, M. V. Fonseca, L. Font, C. Fruck, D. Galindo, R. J. García López, M. Garczarczyk, M. Gaug, P. Giammaria, N. Godinović, D. Gora, S. Griffiths, D. Guberman, D. Hadasch, A. Hahn, T. Hassan, M. Hayashida, J. Herrera, J. Hose, D. Hrupec, G. Hughes, K. Ishio, Y. Konno, H. Kubo, J. Kushida, D. Kuveždić, D. Lelas, E. Lindfors, S. Lombardi, F. Longo, M. López, C. Maggio, P. Majumdar, M. Makariev, G. Maneva, M. Manganaro, K. Mannheim, L. Maraschi, M. Mariotti, M. Martínez, D. Mazin, U. Menzel, M. Minev, R. Mirzoyan, A. Moralejo, V. Moreno, E. Moretti, V. Neustroev, A. Niedzwiecki, M. Nievas Rosillo, K. Nilsson, D. Ninci, K. Nishijima, K. Noda, L. Nogués, S. Paiano, J. Palacio, D. Paneque, R. Paoletti,

J. M. Paredes, X. Paredes-Fortuny, G. Pedaletti, M. Peresano, L. Perri, M. Persic, P. G. Prada Moroni, E. Prandini, I. Puljak, J. R. Garcia, I. Reichardt, W. Rhode, M. Ribó, J. Rico, A. Rugliancich, T. Saito, K. Satalecka, S. Schroeder, T. Schweizer, A. Sillanpää, J. Sitarek, I. Šnidarić, D. Sobczynska, A. Stamerra, M. Strzys, T. Surić, L. Takalo, F. Tavecchio, P. Temnikov, T. Terzić, D. Tescaro, M. Teshima, D. F. Torres, N. Torres-Albà, A. Treves, G. Vanzo, M. Vazquez Acosta, I. Vovk, J. E. Ward, M. Will, and D. Zarić, "Performance of the MAGIC telescopes under moonlight," Astroparticle Phys., vol. 94, pp. 29–41, Sep. 2017.

[121] M. Sicard, C. Pérez, F. Rocadenbosch, J. M. Baldasano, and D. García-Vizcaino, "Mixed-Layer Depth Determination in the Barcelona Coastal Area From Regular Lidar Measurements: Methods, Results and Limitations," Boundary-Layer Meteorology, vol. 119, no. 1, pp. 135–157, Apr 2006. [Online]. Available: https://doi.org/10.1007/s10546-005-9005-9

[122] D. A. Erasmus and R. Van Rooyen, "A satellite survey of cloud cover and water vapor in northwest Africa and southern Spain," in Ground-based and Airborne Telescopes, vol. 6267. SPIE, 2006, pp. 566–577.

[123] D. A. Gouveia, B. Barja, H. M. J. Barbosa, P. Seifert, H. Baars, T. Pauliquevis, and P. Artaxo, "Optical and geometrical properties of cirrus clouds in Amazonia derived from 1 year of ground-based lidar measurements," Atmos. Chem. Phys., vol. 17, pp. 3619–3636, 2017.

[124] P. Keckhut, J.-M. Perrin, G. Thuillier, C. Hoareau, J. Porteneuve, and N. Montoux, "Subgrid-scale cirrus observed by LIDAR at mid-latitude: variability effects of the cloud optical depth," J. of Applied Remote Sensing, vol. 7, pp. 1–15, 2013.

[125] M. Reverdy, V. Noel, H. Chepfer, and B. Legras, "On the origin of subvisible cirrus clouds in the tropical upper troposphere," Atmos. Chem. Phys., vol. 12, pp. 12 081–12 101, 2012.

[126] J. J. Rodriguez-Franco and E. Cuevas, “Characteristics of the subtropical tropopause region based on long-term highly-resolved sonde records over Tenerife,” J. Geophys. Res. Atmos., vol. 118, pp. 10 754–10 769, 2013.

[127] A.-C. Levasseur-Regourd and R. Dumont, “Absolute photometry of zodiacal light,” Astronomy and Astrophysics, vol. 84, no. 3, Apr. 1980, p. 277-279., vol. 84, pp. 277–279, 1980.

[128] Leinert, Ch. et al., “The 1997 reference of diffuse night sky brightness,” A&AS, vol. 127, pp. 1–99, 1998.

[129] “BOE-A-1992-8705, Real Decreto 243/1992, de 13 de marzo, por el que se aprueba el Reglamento de la Ley 31/1988, de 31 de octubre, sobre protección de la calidad astronómica de los observatorios del Instituto de Astrofísica de Canarias,” https://www.boe.es/eli/es/rd/1992/03/13/243, last accessed Jan. 6, 2022, 1988.

[130] BOE-A-1992-8705, “Real Decreto 580/2017, de 12 de junio, por el que se modifica el Real Decreto 243/1992, de 13 de marzo, por el que se aprueba el Reglamento de la Ley 31/1988, de 31 de octubre, sobre Protección de la Calidad Astronómica de los Observatorios del Instituto de Astrofísica de Canarias,” https://www.boe.es/boe/dias/2017/07/01/pdfs/BOE-A-2017-7585.pdf, last accessed Jan. 6, 2022, 2017.

[131] Instituto de Astrofísica de Canarias, Oficina Técnica Protección del Cielo (OTPR), https://www.iac.es/en/organizational-unit/sky-protection-office, last accessed Jan 6, 2022, 1988.

[132] Román, M.O., , Wang, Z., Shrestha, R., Yao, T., and Kalb, V., “VIIRS/NPP Lunar BRDF-Adjusted Nighttime Lights Yearly L3 Global 15 arc second Linear Lat Lon Grid, c1,” NASA Level-1 and Atmosphere Archive & Distribution System (LAADS) Distributed Active Archive Center (DAAC), Goddard Space Flight Center, Greenbelt, MD, USA, 2021. [Online]. Available: https://dx.doi.org/10.5067/VIIRS/VNP46A4.001

[133] K. Bernlöhr, "Impact of atmospheric parameters on the atmospheric Cherenkov technique," Astroparticle Physics, vol. 12, no. 4, pp. 255–268, 2000.

[134] P. Munar-Adrover and M. Gaug, "Studying molecular profiles above the Cherenkov Telescope Array sites," in EPJ Web of Conferences, vol. 197. EDP Sciences, 2019, p. 01002.

[135] O. Dubovik, A. Sinyuk, T. Lapyonok, B. N. Holben, M. Mishchenko, P. Yang, T. F. Eck, H. Volten, O. Muñoz, B. Veihelmann, W. J. van der Zande, J.-F. Leon, M. Sorokin, and I. Slutsker, "Application of spheroid models to account for aerosol particle nonsphericity in remote sensing of desert dust," Journal of Geophysical Research: Atmospheres, vol. 111, no. D11, 2006. [Online]. Available: https://agupubs.onlinelibrary.wiley.com/doi/abs/10.1029/2005JD006619

[136] D. Heck, J. Knapp, J. Capdevielle, G. Schatz, T. Thouw et al., "CORSIKA: A Monte Carlo code to simulate extensive air showers," 1998.

[137] S. A. Bass, M. Belkacem, M. Bleicher, M. Brandstetter, L. Bravina, C. Ernst, L. Gerland, M. Hofmann, S. Hofmann, J. Konopka et al., "Microscopic models for ultrarelativistic heavy ion collisions," Progress in Particle and Nuclear Physics, vol. 41, pp. 255–369, 1998.

[138] M. Pecimotika, D. D. Prester, D. Hrupec, S. Mićanović, L. Pavletić, and J. Sitarek, "Performance and systematic uncertainties of cta-north in conditions of reduced atmospheric transmission," Journal of cosmology and astroparticle physics, vol. 2023, no. 06, p. 011, 2023.

[139] Cherenkov Telescope Array Observatory, "Ctao-north – ctao," 2024, accessed: 2025-06-26. [Online]. Available: https://www.ctao.org/emission-to-discovery/array-sites/ctao-north/

[140] APPEC, "Ctao news: New array layouts for the upcoming new legal entity," 2024, accessed: 2025-06-26. [Online]. Available: https://www.appec.org/news/ctao-news-new-array-layouts-for-the-upcoming-new-legal-entity/

[141] R. Zanin et al., "MARS, the MAGIC analysis and reconstruction software," in 33rd International Cosmic Ray Conference, 2013, p. 773.

[142] J. Aleksić et al., "The major upgrade of the MAGIC telescopes, Part II: A performance study using observations of the Crab Nebula," Astropart. Phys., vol. 72, pp. 76–94, 2016.

[143] E. Aliu et al., "Improving the performance of the single-dish Cherenkov telescope MAGIC through the use of signal timing," Astropart. Phys., vol. 30, pp. 293–305, 2009.

[144] A. M. Hillas, "Cerenkov Light Images of EAS Produced by Primary Gamma Rays and by Nuclei," in 19th International Cosmic Ray Conference, vol. 3, 1985, p. 445.

[145] J. Albert et al., "Implementation of the Random Forest Method for the Imaging Atmospheric Cherenkov Telescope MAGIC," Nucl. Instrum. Meth. A, vol. 588, pp. 424–432, 2008.

[146] A. Ivanović and et al., "A novel energy reconstruction method for wide-field-of-view imaging atmospheric cherenkov technique experiments," Experimental Astronomy, vol. 49, pp. 1–19, 2025. [Online]. Available: https://link.springer.com/article/10.1007/s10686-025-10007-x

[147] U. of Rijeka, "Bura Supercomputer," https://cnrm.uniri.hr/bura/, accessed: 2025-03-29.

[148] L. Petrov, "The catalog of positions of optically bright extragalactic radio sources OBRS-1," The Astronomical Journal, vol. 142, no. 4, p. 105, 2011.

[149] S. Abdollahi, F. Acero, L. Baldini, J. Ballet, D. Bastieri, R. Bellazzini, B. Berenji, A. Berretta, E. Bissaldi, R. D. Blandford et al., "Incremental Fermi large area telescope fourth source catalog," The Astrophysical Journal Supplement Series, vol. 260, no. 2, p. 53, 2022.

[150] S. Laurent-Muehleisen, R. Kollgaard, E. Feigelson, W. Brinkmann, and J. Siebert, "The RGB Sample of intermediate BL Lacertae objects," The Astrophysical Journal, vol. 525, no. 1, p. 127, 1999.

[151] V. F. Ramazani, E. Lindfors, and K. Nilsson, "Empirical multi-wavelength prediction method for very high energy gamma-ray emitting BL Lacertae objects," Astronomy & Astrophysics, vol. 608, p. A68, 2017.

[152] P. Giommi, G. Tagliaferri, K. Beuermann, G. Branduardi-Raymont, R. Brissenden, U. Graser, K. Mason, J. Mittaz, P. Murdin, G. Pooley et al., "The EXOSAT high Galactic latitude survey," Astrophysical Journal, Part 1 (ISSN 0004-637X), vol. 378, Sept. 1, 1991, p. 77-92. Research supported by Royal Society and SERC., vol. 378, pp. 77–92, 1991.

[153] M. Ajello, R. Angioni, M. Axelsson, J. Ballet, G. Barbiellini, D. Bastieri, J. B. Gonzalez, R. Bellazzini, E. Bissaldi, E. Bloom et al., "The fourth catalog of active galactic nuclei detected by the Fermi Large Area Telescope," The Astrophysical Journal, vol. 892, no. 2, p. 105, 2020.

[154] O. Blanch, "Detection of very-high-energy gamma-ray emission from B2 1811+ 31 with the MAGIC telescopes," The Astronomer's Telegram, vol. 14090, p. 1, 2020.

[155] K. Abe et al., "Very-high-energy gamma-ray detection and long-term multi-wavelength view of the flaring blazar B2 1811+31," A&A, March 2025.

[156] T. P. Li and Y. Q. Ma, "Analysis methods for results in gamma-ray astronomy." , vol. 272, pp. 317–324, Sep. 1983.

[157] J. Albert, E. Aliu, H. Anderhub, P. Antoranz, A. Armada, C. Baixeras, J. Barrio, H. Bartko, D. Bastieri, J. Becker et al., "Variable very high energy γ-ray emission from Markarian 501," The Astrophysical Journal, vol. 669, no. 2, p. 862, 2007.

[158] W. Atwood, A. A. Abdo, M. Ackermann, W. Althouse, B. Anderson, M. Axelsson, L. Baldini, J. Ballet, D. Band, G. Barbiellini et al., "The large area telescope on the Fermi gamma-ray space telescope mission," The Astrophysical Journal, vol. 697, no. 2, p. 1071, 2009.

[159] W. Atwood, A. Albert, L. Baldini, M. Tinivella, J. Bregeon, M. Pesce-Rollins, C. Sgrò, P. Bruel, E. Charles, A. Drlica-Wagner et al., "Pass 8: toward the full realization of the Fermi-LAT scientific potential," arXiv preprint arXiv:1303.3514, 2013.

[160] P. Bruel, T. Burnett, S. Digel, G. Johannesson, N. Omodei, and M. Wood, "Fermi-LAT improved Pass˜ 8 event selection," arXiv preprint arXiv:1810.11394, 2018.

[161] S. M. D. f. g. Fermi Gamma-ray Space Telescope. [Online]. Available: https://www.lightpollutionmap.info

[162] S. Abdollahi, M. Ajello, L. Baldini, J. Ballet, D. Bastieri, J. B. Gonzalez, R. Bellazzini, A. Berretta, E. Bissaldi, R. Bonino et al., "The fermi-LAT lightcurve repository," The Astrophysical Journal Supplement Series, vol. 265, no. 2, p. 31, 2023.

[163] B. Lott, L. Escande, S. Larsson, and J. Ballet, "An adaptive-binning method for generating constant-uncertainty/constant-significance light curves with Fermi-LAT data," Astronomy & Astrophysics, vol. 544, p. A6, 2012.

[164] N. Gehrels, G. Chincarini, P. Giommi, K. Mason, J. Nousek, A. Wells, N. White, S. Barthelmy, D. N. Burrows, L. R. Cominsky et al., "The Swift gamma-ray burst mission," The Astrophysical Journal, vol. 611, no. 2, p. 1005, 2004.

[165] S. D. Barthelmy, L. M. Barbier, J. R. Cummings, E. E. Fenimore, N. Gehrels, D. Hullinger, H. A. Krimm, C. B. Markwardt, D. M. Palmer, A. Parsons et al., "The

burst alert telescope (BAT) on the SWIFT midex mission," Space Science Reviews, vol. 120, pp. 143–164, 2005.

[166] D. N. Burrows, P. Romano, A. Falcone, S. Kobayashi, B. Zhang, A. Moretti, P. O'brien, M. Goad, S. Campana, K. Page et al., "Bright X-ray flares in gamma-ray burst afterglows," Science, vol. 309, no. 5742, pp. 1833–1835, 2005.

[167] P. W. Roming, T. E. Kennedy, K. O. Mason, J. A. Nousek, L. Ahr, R. E. Bingham, P. S. Broos, M. J. Carter, B. K. Hancock, H. E. Huckle et al., "The Swift ultra-violet/optical telescope," Space Science Reviews, vol. 120, pp. 95–142, 2005.

[168] P. Evans, A. Beardmore, K. Page, J. Osborne, P. O'Brien, R. Willingale, R. Starling, D. N. Burrows, O. Godet, L. Vetere et al., "Methods and results of an automatic analysis of a complete sample of Swift-XRT observations of GRBs," Monthly Notices of the Royal Astronomical Society, vol. 397, no. 3, pp. 1177–1201, 2009.

[169] K. Arnaud, "Astronomical data analysis software and systems V," in ASP Conf., vol. 17, 1996.

[170] R. Willingale, R. Starling, A. P. Beardmore, N. R. Tanvir, and P. T. O'Brien, "Calibration of X-ray absorption in our Galaxy," Monthly Notices of the Royal Astronomical Society, vol. 431, no. 1, pp. 394–404, 2013.

[171] J. Wilms, A. Allen, and R. McCray, "On the absorption of X-rays in the interstellar medium," arXiv preprint astro-ph/0008425, 2000.

[172] W. Cash, "Parameter estimation in astronomy through application of the likelihood ratio," Astrophysical Journal, Part 1, vol. 228, Mar. 15, 1979, p. 939-947., vol. 228, pp. 939–947, 1979.

[173] J. Aleksić, S. Ansoldi, L. A. Antonelli, P. Antoranz, A. Babic, P. Bangale, U. B. De Almeida, J. Barrio, J. B. González, W. Bednarek et al., "Unprecedented study of the broadband emission of Mrk 421 during flaring activity in March 2010," Astronomy & astrophysics, vol. 578, p. A22, 2015.

[174] Z. R. Weaver, K. Williamson, S. Jorstad, A. Marscher, V. Larionov, C. M. Raiteri, M. Villata, J. Acosta-Pulido, R. Bachev, G. Baida et al., “Multiwavelength variability of BL Lacertae measured with high time resolution,” The Astrophysical Journal, vol. 900, no. 2, p. 137, 2020.

[175] T. Poole, A. Breeveld, M. Page, W. Landsman, S. Holland, P. Roming, N. Kuin, P. Brown, C. Gronwall, S. Hunsberger et al., “Photometric calibration of the Swift ultraviolet/optical telescope,” Monthly Notices of the Royal Astronomical Society, vol. 383, no. 2, pp. 627–645, 2008.

[176] A. Breeveld, P. Curran, E. Hoversten, S. Koch, W. Landsman, F. Marshall, M. Page, T. Poole, P. Roming, P. Smith et al., “Further calibration of the Swift ultraviolet/optical telescope,” Monthly Notices of the Royal Astronomical Society, vol. 406, no. 3, pp. 1687–1700, 2010.

[177] E. L. Fitzpatrick, “Correcting for the effects of interstellar extinction,” Publications of the Astronomical Society of the Pacific, vol. 111, no. 755, p. 63, 1999.

[178] E. F. Schlafly and D. P. Finkbeiner, “Measuring reddening with Sloan Digital Sky Survey stellar spectra and recalibrating SFD,” The Astrophysical Journal, vol. 737, no. 2, p. 103, 2011.

[179] E. C. Bellm, S. R. Kulkarni, T. Barlow, U. Feindt, M. J. Graham, A. Goobar, T. Kupfer, C.-C. Ngeow, P. Nugent, E. Ofek et al., “The zwicky transient facility: Surveys and scheduler,” Publications of the Astronomical Society of the Pacific, vol. 131, no. 1000, p. 068003, 2019.

[180] A. V. Filippenko, W. Li, R. Treffers, and M. Modjaz, “The lick observatory supernova search with the Katzman automatic imaging telescope,” in International Astronomical Union Colloquium, vol. 183. Cambridge University Press, 2001, pp. 121–130.

[181] A. Drake, S. Djorgovski, A. Mahabal, J. Prieto, E. Beshore, M. Graham, M. Catalan, S. Larson, E. Christensen, C. Donalek et al., “The Catalina real-time transient survey,” Proceedings of the International Astronomical Union, vol. 7, no. S285, pp. 306–308, 2011.

[182] K. Nilsson, E. Lindfors, L. Takalo, R. Reinthal, A. Berdyugin, A. Sillanpää, S. Ciprini, A. Halkola, P. Heinämäki, T. Hovatta et al., “Long-term optical monitoring of TeV emitting blazars-I. Data analysis,” Astronomy & Astrophysics, vol. 620, p. A185, 2018.

[183] P. M. Kouch, I. Liodakis, R. Middei, D. E. Kim, F. Tavecchio, A. P. Marscher, H. L. Marshall, S. R. Ehlert, L. Di Gesu, S. G. Jorstad et al., “IXPE observation of PKS 2155-304 reveals the most highly polarized blazar,” arXiv preprint arXiv:2406.01693, 2024.

[184] K. Nilsson, T. Pursimo, J. Heidt, L. Takalo, A. Sillanpää, and W. Brinkmann, “R-band imaging of the host galaxies of RGB BL Lacertae objects,” Astronomy & Astrophysics, vol. 400, no. 1, pp. 95–118, 2003.

[185] J. L. Richards, W. Max-Moerbeck, V. Pavlidou, O. G. King, T. J. Pearson, A. C. Readhead, R. Reeves, M. C. Shepherd, M. A. Stevenson, L. C. Weintraub et al., “Blazars in the FERMI Era: The OVRO 40 m telescope monitoring program,” The Astrophysical Journal Supplement Series, vol. 194, no. 2, p. 29, 2011.

[186] F. Eppel, M. Kadler, J. Heßdörfer, P. Benke, L. Debbrecht, J. Eich, A. Gokus, S. Hämmerich, D. Kirchner, G. Paraschos et al., “TELAMON: Effelsberg monitoring of AGN jets with very-high-energy astroparticle emission-I. Program description and sample characterization,” Astronomy & Astrophysics, vol. 684, p. A11, 2024.

[187] S. Abe, J. Abhir, V. Acciari, A. Aguasca-Cabot, I. Agudo, T. Aniello, S. Ansoldi, L. Antonelli, A. A. Engels, C. Arcaro et al., “Insights into the broadband emis-

sion of the TeV blazar Mrk 501 during the first X-ray polarization measurements," Astronomy & Astrophysics, vol. 685, p. A117, 2024.

[188] L. Foschini, G. Bonnoli, G. Ghisellini, G. Tagliaferri, F. Tavecchio, and A. Stamerra, "Fermi/LAT detection of extraordinary variability in the gamma-ray emission of the blazar PKS 1510-089," Astronomy & Astrophysics, vol. 555, p. A138, 2013.

[189] M. collaboration, V. Acciari, S. Ansoldi, L. Antonelli, A. Arbet Engels, M. Artero, K. Asano, D. Baack, A. Babić, A. Baquero et al., "First detection of VHE gamma-ray emission from TXS 1515–273, study of its X-ray variability and spectral energy distribution," Monthly Notices of the Royal Astronomical Society, vol. 507, no. 1, pp. 1528–1545, 2021.

[190] S. Abe, J. Abhir, V. Acciari, I. Agudo, T. Aniello, S. Ansoldi, L. Antonelli, A. A. Engels, C. Arcaro, M. Artero et al., "First characterization of the emission behavior of Mrk421 from radio to VHE gamma rays with simultaneous X-ray polarization measurements," arXiv preprint arXiv:2312.10732, 2023.

[191] E. Pian, E. Palazzi, L. Chiappetti, L. Maraschi, F. Tavecchio, G. Ghisellini, G. Tagliaferri, G. Fossati, A. Treves, C. M. Urry et al., "Bepposax observations of the BL Lac object Mkn 501 in an intermediate state," arXiv preprint astro-ph/9810398, 1998.

[192] M. Böttcher, "The synchrotron peak shift during high-energy flares of blazars," The Astrophysical Journal, vol. 515, no. 1, p. L21, 1999.

[193] E. L. Wright, P. R. Eisenhardt, A. K. Mainzer, M. E. Ressler, R. M. Cutri, T. Jarrett, J. D. Kirkpatrick, D. Padgett, R. S. McMillan, M. Skrutskie et al., "The Wide-field Infrared Survey Explorer (WISE): mission description and initial on-orbit performance," The Astronomical Journal, vol. 140, no. 6, p. 1868, 2010.

[194] N. Sahakyan and P. Giommi, "A 13-yr-long broad-band view of BL Lac," Monthly Notices of the Royal Astronomical Society, vol. 513, no. 3, pp. 4645–4656, 2022.

[195] E. Dwek and F. Krennrich, “The extragalactic background light and the gamma-ray opacity of the universe,” Astroparticle Physics, vol. 43, pp. 112–133, 2013.

[196] E. Prandini, G. Bonnoli, L. Maraschi, M. Mariotti, and F. Tavecchio, “TeV blazars and their distance,” arXiv preprint arXiv:1101.5005, 2011.

[197] A. R. Whitney, I. I. Shapiro, A. E. Rogers, D. S. Robertson, C. A. Knight, T. A. Clark, R. M. Goldstein, G. E. Marandino, and N. R. Vandenberg, “Quasars revisited: rapid time variations observed via very-long-baseline interferometry,” Science, vol. 173, no. 3993, pp. 225–230, 1971.

[198] M. Cohen, W. Cannon, G. Purcell, D. Shaffer, J. Broderick, K. Kellermann, and D. Jauncey, “The small-scale structure of radio galaxies and quasi-stellar sources at 3.8 centimeters,” Astrophysical Journal, vol. 170, p. 207, vol. 170, p. 207, 1971.

[199] J. Biretta, W. Sparks, and F. Macchetto, “Hubble Space Telescope observations of superluminal motion in the M87 jet,” The Astrophysical Journal, vol. 520, no. 2, p. 621, 1999.

[200] B. Snios, P. E. Nulsen, R. P. Kraft, C. Cheung, E. T. Meyer, W. R. Forman, C. Jones, and S. S. Murray, “Detection of Superluminal Motion in the X-ray Jet of M87,” The Astrophysical Journal, vol. 879, no. 1, p. 8, 2019.

[201] D. Giannios and H. C. Spruit, “The role of kink instability in Poynting-flux dominated jets,” Astronomy & Astrophysics, vol. 450, no. 3, pp. 887–898, 2006.

[202] N. S. Kardashev, “Nonstationarity of spectra of young sources of nonthermal radio emission,” Soviet Astronomy, Vol. 6, p. 317, vol. 6, p. 317, 1962.

[203] M. Böttcher, A. Reimer, K. Sweeney, and A. Prakash, “Leptonic and hadronic modeling of Fermi-detected blazars,” The Astrophysical Journal, vol. 768, no. 1, p. 54, 2013.

[204] A. Zech, M. Cerruti, and D. Mazin, “Expected signatures from hadronic emission processes in the TeV spectra of BL Lacertae objects,” Astronomy & Astrophysics, vol. 602, p. A25, 2017.

[205] M. Cerruti, W. Benbow, X. Chen, J. P. Dumm, L. Fortson, and K. Shahinyan, “Luminous and high-frequency peaked blazars: the origin of the γ-ray emission from PKS 1424+ 240,” Astronomy & Astrophysics, vol. 606, p. A68, 2017.

[206] A. Aab, P. Abreu, M. Aglietta, J. M. Albury, I. Allekotte, A. Almela, J. Alvarez-Muñiz, R. A. Batista, G. A. Anastasi, L. Anchordoqui et al., “A Search for Ultra-high-energy Neutrinos from TXS 0506+ 056 Using the Pierre Auger Observatory,” The Astrophysical Journal, vol. 902, no. 2, p. 105, 2020.

[207] R. Abbasi, M. Ackermann, J. Adams, J. Aguilar, M. Ahlers, M. Ahrens, C. Alispach, A. Alves, N. Amin, R. An et al., “Search for Multi-flare Neutrino Emissions in 10 yr of IceCube Data from a Catalog of Sources,” The Astrophysical Journal Letters, vol. 920, no. 2, p. L45, 2021.

[208] R. Abbasi, M. Ackermann, J. Adams, S. Agarwalla, J. Aguilar, M. Ahlers, J. Alameddine, N. Amin, K. Andeen, G. Anton et al., “IceCat-1: The IceCube Event Catalog of Alert Tracks,” The Astrophysical Journal Supplement Series, vol. 269, no. 1, p. 25, 2023.

[209] C. Nigro, J. Sitarek, P. Gliwny, D. Sanchez, A. Tramacere, and M. Craig, “agnpy: An open-source python package modelling the radiative processes of jetted active galactic nuclei,” Astronomy & Astrophysics, vol. 660, p. A18, 2022.

[210] T. Hovatta, E. Valtaoja, M. Tornikoski, and A. Lähteenmäki, “Doppler factors, Lorentz factors and viewing angles for quasars, BL Lacertae objects and radio galaxies,” Astronomy & Astrophysics, vol. 494, no. 2, pp. 527–537, 2009.

[211] F. Tavecchio and G. Ghisellini, “On the magnetization of BL Lac jets,” Monthly Notices of the Royal Astronomical Society, vol. 456, no. 3, pp. 2374–2382, 2016.

[212] V. A. Acciari, S. Ansoldi, L. A. Antonelli, A. A. Engels, D. Baack, A. Babić, B. Banerjee, U. B. De Almeida, J. A. Barrio, J. B. González et al., "Broadband characterisation of the very intense TeV flares of the blazar 1ES 1959+ 650 in 2016," Astronomy & astrophysics, vol. 638, p. A14, 2020.

[213] F. Tavecchio, J. Becerra-Gonzalez, G. Ghisellini, A. Stamerra, G. Bonnoli, L. Foschini, and L. Maraschi, "On the origin of the γ-ray emission from the flaring blazar PKS 1222+ 216," Astronomy & Astrophysics, vol. 534, p. A86, 2011.

[214] S. Inoue and F. Takahara, "Electron acceleration and gamma-ray emission from blazars," Astrophysical Journal v. 463, p. 555, vol. 463, p. 555, 1996.

[215] M. Cerruti, "Leptonic and hadronic radiative processes in supermassive-black-hole jets," Galaxies, vol. 8, no. 4, p. 72, 2020.